UNIVERSIDAD POLITÉCNICA DE MADRID
ESCUELA TÉCNICA SUPERIOR DE INGENIEROS AERONÁUTICOS

THE DYNAMICS OF THE OUTER REGION OF WALL-BOUNDED TURBULENCE

LA DINÁMICA DE LA ZONA EXTERIOR EN LA TURBULENCIA DE PARED

Tesis Doctoral

Por
Oscar Flores
Ingeniero Aeronáutico

Madrid, Diciembre 2007

DEPARTAMENTO DE MOTOPROPULSIÓN Y TERMOFLUIDODINÁMICA
ESCUELA TÉCNICA SUPERIOR DE INGENIEROS AERONÁUTICOS

THE DYNAMICS OF THE OUTER REGION OF WALL-BOUNDED TURBULENCE

LA DINÁMICA DE LA ZONA EXTERIOR EN LA TURBULENCIA DE PARED

Autor
Oscar Flores
Ingeniero Aeronáutico

Director de Tesis
Javier Jiménez
Doctor Ingeniero Aeronáutico

Madrid, Diciembre 2007

Contents

Contents i

Acknowledgements iii

Nomenclature v

Abstract xi

Resumen xiii

1. Introduction **1**
1.1. Historical remarks 1
1.2. Wall-bounded turbulence 4
1.2.1. Turbulent flows over rough walls 10
1.3. Techniques employed in the study of wall-turbulence 13
1.4. Aims 16
1.5. Contents 17

2. DNS of turbulent channel with wall disturbances [1] **19**
2.1. Introduction 19
2.2. Numerical Experiments 21
2.3. One-point statistics 22
2.4. Box-filtered flow fields 29
2.5. Spectral analysis 32
2.5.1. Global modes 33
2.6. Conclusions 40

3. Vorticity organization in the outer layer of turbulent channels with disturbed walls [2] **43**
3.1. Introduction 43
3.2. Cluster identification methodology 45

[1] Part of the contents of this chapter have been published in the Journal of Fluid Mechanics, volume 566, pages 357-376, with Javier Jiménez as coauthor.

[2] Part of the contents of this chapter have been published in the Journal of Fluid Mechanics, volume 591, pages 145-154, with Javier Jiménez and Juan C. del Álamo as coauthors.

3.3. The geometry and distribution of the detached clusters 47
3.4. The geometry and distribution of the attached clusters 49
3.5. The average velocity field conditioned to the tall attached clusters . . 54
3.6. Conclusions 58

4. Linear analysis of self-similar structures in the turbulent logarithmic region 61
4.1. Introduction 61
4.2. The linearized equations for elongated turbulent structures 63
4.2.1. Self-similar form of the linearized N-S equations 65
4.3. Numerical solution 66
4.4. Results from the linear model 68
4.4.1. Energy growth and lifetimes 68
4.4.2. Self-similarity 71
4.4.3. Velocity structure 73
4.4.4. Linear model over rough walls 78
4.5. Origin of the bursts 79
4.6. Conclusions 85

5. Conclusions and future work 87

References 93

Acknowledgements

I am indebted to many people who have been fundamental in the development of this thesis. First to my advisor, Javier Jiménez, who introduced me to the world of scientific research and to the subject of wall-bounded turbulence. He has provided the indispensable support and guidance for the completion of the present thesis, apart from teaching me many lessons that I am sure I will not forget. I am also grateful to Rafael Gómez-Blanco, Vassilis Theofilis and Francisco Higuera, for their constant interest in my work throughout this PhD. I also appreciate the help received from the people working in the School of Aeronautics, particularly Jóse Sánchez and Fernando Fernández. And finally, I would also like to thank Prof. Robert Moser for his interest in my thesis, and for giving me the opportunity to work with him one summer in the Mechanical Engineering Department in the University of Texas at Austin.

I will always remember with a smile all the friends that I have made during these five years; Dani, Guillem, Gwenael, Jorge, Juanc, Leo, Mark, Miguel, Marcos, Mario, Samuel, Sergio, Yhosi and many others. They have shared many joys and jokes with me during this time. Amongst them, I am particularly grateful to Mark and Juanc, who, apart from sharing joys and jokes, have also shared worries and concerns, and have participated in many fruitful discussions on our research. It has been a pleasure to work with them.

I am also grateful to my family: my parents and my brother, who have done far more for me than I can express in words. Explaining my research to them and at the same time observing in their faces the mixture of pride and puzzlement has been a great pleasure. Patricia also deserves my deepest gratitude, for being on my side throughout this PhD. Not only she has contributed to the revision of this thesis, but more important, she has given my her support, love and friendship.

The research presented in this thesis has been carried out at the Department of Propulsion and Fluid Mechanics (*Departamento de Motopopulsión y Termofluidodinámica*) of the School of Aeronautics (*Escuela Técnica Superior de Ingenieros Aeronáuticos*), which is part of the Polytechnic University of Madrid (*Universidad Politécnica de Madrid*). The calculations for the numerical experiments of this thesis have been performed in several machines, including our clusters in the department, the super-computer *Mare Nostrum* at the BSC (Barcelona), the clusters in CIEMAT

(Madrid) and in CEPBA (UPC, Barcelona). I must acknowledge the computational time they all donated. Most of the storage and post-processing of the database has been done in the servers of the department. The data of the largest simulation are mirrored in the servers of the Port d'Informació Científica (PIC, Barcelona), who graciously donated around 0.4TB of disk space.

The necessary financial support has been provided by the Spanish CICYT (*Comisión Interministerial de Ciencia y Tecnología*) under grants DPI2003-03434 and TRA2006-08226, and by the Spanish Ministry of Education (*Ministerio de Educación y Ciencia*), through a four-year FPI scholarship. This financial support has allowed for a short summer visit to the Center for Turbulence Research in Standford, directed by Prof. Parviz Moin.

Nomenclature

$(\cdot)'$ Root mean square, or quadratic average, of $(\cdot)$.

$(\cdot)^*$ Complex conjugate of $(\cdot)$.

$(\cdot)^+$ Variable in wall units, normalized using u_τ and ν.

$\overline{(\cdot)}$ Ensemble average in the homogeneous directions.

$\widehat{\varphi}$ Coefficients of the Fourier expansion of φ.

$\mathbf{r} = (r_x, r_y, r_z)$ Coordinate system centered at the cluster and scaled with its wall-normal size.

$\mathbf{x_c} = (x_c, y_c, z_c)$ Center of the Cartesian box that circumscribes the cluster.

$\mathbf{x_u} = (x_u, y_u, z_u)$ Centroid of the streamwise kinetic energy distribution in the linear model.

$\mathbf{x_v} = (x_v, y_v, z_v)$ Centroid of the wall-normal kinetic energy distribution in the linear model.

$\langle \mathbf{u} \rangle = (\langle u \rangle , \langle v \rangle , \langle w \rangle)$ Average velocity fluctuations conditioned to attached clusters.

$\langle \mathbf{u} \rangle_L = (\langle u \rangle_L, \langle v \rangle_L, \langle w \rangle_L)$ Time averaged velocity fluctuations field for the linear model.

A Intercept constant in the log law over smooth walls.

B Intercept constant in the log law for rough-walled flows when the wall distance is normalized with the roughness length scale.

C Intercept constant in the log law for rough-walled flows when the wall distance is in wall units.

C_{rs} Correlation coefficient between the Fourier velocity components $\hat{r}$ and $\hat{s}$.

D Discriminant of the velocity gradient tensor.

E_u One dimensional energy spectrum.

F_c Ratio of Reynolds stress averaged in the region occupied by attached clusters to total Reynolds stress.

F_e Ratio of Reynolds stress averaged in the region free of attached clusters to total Reynolds stress.

F_{uv} Structure function, or ratio between the tangential Reynolds stresses and the product of the root mean square of the velocities.

H_{uu} Correlation height of the streamwise velocity.

K_x Streamwise wavenumber of the velocity disturbances at the wall.

K_z Spanwise wavenumber of the velocity disturbances at the wall.

L Distance to the entrance of the pipe.

L_ϵ Integral length scale.

L_x Streamwise periodicity of the computational domain.

L_y Size of the numerical domain in the wall-normal direction.

L_z Spanwise periodicity of the computational domain.

N_C Total number of extracted clusters.

N_x Number of points used in the streamwise direction for the numerical solution of the linear model.

N_y Number of points used in the wall-normal direction for the numerical solution of the linear model.

N_z Number of points used in the spanwise direction for the numerical solution of the linear model.

N_{att} Total number of attached clusters.

P_0 Mean value of the pressure.

Q Second invariant of the velocity gradient tensor.

Q_u Instantaneous streamwise energy in the linear model.

Q_v Instantaneous wall-normal energy in the linear model.

Q_0 Initial energy in the linear model.

Q_{vw} Instantaneous cross-flow energy in the linear model.

R Pipe radius.

Re Reynolds number.

Re_λ Microscale Reynolds number.

Re_τ Friction Reynolds number, also known as Kármán number.

S^k Set of characteristic lengthscales that characterize a rough surface.

T_l Integral time of the wall-normal energy in the linear model.

T_v Integral time of the wall-normal velocity in turbulent channels.

$T_{\max}$ Time to maximum growth.

U Mean velocity in the streamwise direction.

U_b Bulk velocity.

U_c Mean streamwise velocity at the centerline.

U_e Characteristic mean velocity difference experienced by an eddy.

U_w Mean streamwise velocity fluctuations inside low-velocity cones.

V_r Relative volume occupied by vortex clusters.

V_w Mean wall-normal velocity fluctuations inside low-velocity cones.

W Mean velocity in the spanwise direction.

α Threshold of the clusters identification criterion.

α_c Percolation threshold of the clusters identification criterion.

β Fraction of the Reynolds stresses included in ν_T.

χ Self-similar variable for the streamwise coordinate.

Δc Difference between the phase velocity and the mean velocity profile.

ΔU Roughness function.

Δx Streamwise resolution of the mesh after dealiasing.

δx Streamwise separation.

Δy_c Wall-normal resolution of the mesh at the center of the channel.

Δy_w Wall-normal resolution of the mesh at the wall.

Δz Spanwise resolution of the mesh after dealiasing.

δz Spanwise separation.

δ Boundary layer thickness.

Δ_x Streamwise length of the Cartesian box that circumscribes the cluster.

Δ_y Wall-normal length of the Cartesian box that circumscribes the cluster.

δ_y Wall-normal shift or error-in-origin over a rough wall.

Δ_z Spanwise length of the Cartesian box that circumscribes the cluster.

ℓ Characteristic size of a turbulent eddy.

η Self-similar variable for the wall-normal coordinate.

η_k Kolmogorov length scale.

Λ_x Streamwise wavelength of the velocity disturbances at the wall.

Λ_z Spanwise wavelength of the velocity disturbances at the wall.

κ Kármán constant.

λ_x Streamwise wavelength.

λ_z Spanwise wavelength.

ν Kinematic viscosity.

ν_T Turbulent eddy viscosity.

ν_W Extra additive constant that introduces the effect of wall roughness in ν_T.

ω_x Streamwise vorticity.

ω_y Spanwise vorticity.

ω_z Wall-normal vorticity.

Φ Wall-normal turbulent energy flux.

ϕ_{rr} Premultiplied spectral energy density of the velocity component r.

Π Turbulent energy production.

ψ Transverse stream function, $v = \psi_z$ and $w = -\psi_y$.

ρ Density.

ρ_{rs} Correlation coefficient between the velocity components r and s.

τ	Normalized time, using the initial size of the burst and the friction velocity.
τ_w	Shear stress at the wall.
$\tilde{\omega}_x$	Streamwise vorticity in self-similar form.
ε	Turbulent energy dissipation.
ζ	Self-similar variable for the spanwise coordinate.
c	Phase velocity.
e_u	Wall-normal distribution of streamwise velocity energy.
e_{vw}	Wall-normal distribution of cross-flow velocity energy.
h	Channel half-height.
h_R	Height of the roughness sublayer.
k	Height of the roughness elements.
k_1	Wavenumber in the direction of the velocity.
k_x	Wavenumber in the streamwise direction.
k_z	Wavenumber in the spanwise direction.
l_x	Characteristic dimension of an eddy in the streamwise direction.
l_y	Characteristic dimension of an eddy in the wall-normal direction.
l_z	Characteristic dimension of an eddy in the spanwise direction.
n_a	Density of attached clusters per unit wall-parallel area.
n_d	Density of detached clusters per unit wall-parallel area.
p_c	Characteristic rapid pressure fluctuations of an eddy.
p_V	Probability density function of the minimum and maximum heights of a cluster.
p_Δ	Joint probability density function of the logarithm of the sizes of the clusters.
q	Energy in the streamwise velocity at wavelengths $6h < \lambda_x < 24h$ and $\lambda_z > h$.
t_ℓ	Characteristic turnover time of a turbulent eddy.
t_ν	Viscous time scale.
t_c	Characteristic time of an eddy.

$\tilde{u}$	Streamwise velocity in self-similar form.
u	Streamwise velocity fluctuation.
${u'_F}^2$	Streamwise kinetic energy contained in the Fourier modes associated to the wall disturbances.
u_ℓ	Characteristic velocity of a turbulent eddy.
u_τ	Friction velocity.
u_B	Average velocity fluctuations around the wall velocity disturbances.
u_k	Kolmogorov velocity scale.
v	Wall-normal velocity fluctuation.
v_c	Characteristic wall-normal velocity of an eddy.
w	Spanwise velocity fluctuation.
w_c	Characteristic spanwise velocity of an eddy.
x	Streamwise coordinate.
$\tilde{y}$	Wall-normal coordinate adjusted with δ_y.
y	Wall-normal coordinate.
y_0	Wall-distance of the center of the initial burst for the linear model.
$y_{\max}$	Maximum wall-distance of a cluster.
$y_{\min}$	Minimum wall-distance of a cluster.
z	Spanwise coordinate.

Abstract

The objective of this thesis is the analysis of the dynamics of the outer region of wall-bounded flows, focusing on the interaction between the inner- and outer-layers. The primary tool used in the present study is a set of Direct Numerical Simulations (DNS) of turbulent channels with friction Reynolds number $Re_\tau \approx 630$. In those simulations, the standard non-slip and impermeability boundary conditions are substituted by prescribed velocity disturbances that destroy the near-wall energy cycle characteristic smooth-walled flows. In this sense, the present DNSes can be understood as a simulation of a turbulent flow consisting on a core region without a near-wall region. The profiles of the mean velocity and of the velocity fluctuation intensity show similar effects as those reported on rough-walled flows, and our wall-forcing corresponds to equivalent sand roughness in the fully rough regime.

The changes on the flow structure imposed by the wall forcing are essentially limited to the roughness sublayer; a layer near the wall whose height is proportional to a length scale defined in terms of the additional Reynolds stresses. The spectral distribution of energy in this layer is dominated by the wavenumber of the velocity disturbances and by its harmonics. Outside of it, only the largest scales of the flow are modified by the wall forcing. They are the global modes identified in previous works, corresponding to structures highly correlated from the wall to the center of the channel. Our results indicate that their intensity does not scale with the friction velocity, nor with the centerline velocity. However, a velocity scale proporional to $u_\tau \log(Re_\tau)$ is able to collapse of the velocity fluctuations of several wall-bounded turbulent flows over a wide range of Reynolds numbers and surface roughness.

Similar conclusions are drawn from the analysis of the coherent structures of vorticity that populate the logarithmic and outer regions of the wall-disturbed cases. The attached clusters have the same properties over smooth and rough walls, and in both cases they make important contributions to the Reynolds stress in the logarithmic and outer regions. In average, the attached clusters are statistically associated with wall-normal velocity bursts and cone-shaped streaks of low-momentum fluid. Our results indicate that the global modes are connected to the part of these streaks that have sizes comparable to the flow thickness. They are very coherent motions, where the wall-normal and streamwise velocity components are tightly coupled.

The final part of this thesis puts together all those observations into a linear

model that explains the generation of the cone-shaped low-speed streaks of the logarithmic region by bursts of wall-normal velocity. The results of the linear simulations show that localized bursts generate elongated upstream u-streaks that agree well with the velocity fields conditioned to attached clusters, but where the downstream wakes observed in real turbulent flows are absent. The absence of the downstream part of the low-momentum cones suggests that the cones are the cause, rather than the effect, of the bursts. It is hypothesized that the burst are generated by some instability of the local velocity profile, in analogy with the near-wall cycle. However, while the near-wall cycle is autonomous, the effect of the outer region has to be included in the model in order to generate strong enough streaks. This suggests that the causality assumed in most models of wall-bounded turbulence could be reversed, and that the outer region may be critical for the dynamics of the logarithmic layer.

Resumen

El objetivo de esta tesis es el análisis de las interacciones entre la zona de la pared y la zona exterior en flujos turbulentos. Se trata de un problema con gran interés tecnológico, puesto que estas interacciones son importantes para la predicción y el control de la separación en perfiles aerodinámicos en aeronaves y turborreactores, la pérdida de presión en sistemas de tuberías, la dispersión de contaminantes en la atmósfera o el efecto de la topografía en la capa límite atmosférica. La turbulencia también es un problema muy interesante desde un punto de vista puramente matemático, pues ofrece uno de los paradigmas de sistema dinámico no lineal intrínsecamente disipativo: incluso cuando la viscosidad tiende a cero, la disipación tiende a una constante.

La investigación de la turbulencia de pared ha realizado importantes avances durante las últimas décadas, y se puede afirmar sin duda alguna que nuestro conocimiento de la estructura y dinámica de la zona cercana a la pared es bastante completo. Sin embargo, existe una cierta controversia acerca del papel que juega esta zona en la dinámica del resto del flujo. Para analizar esta cuestión, en esta tesis se han desarrollado una serie de Simulaciones Numéricas Directas (DNS) de canales turbulentos con perturbaciones de velocidad en las paredes. Estas perturbaciones cambian por completo la estructura de la turbulencia en la zona cercana a la pared, permitiendo evaluar su influencia en la zona exterior del flujo.

En esta tesis consideraremos siempre flujos homogéneos en las direcciones paralelas a las paredes, x y z, con un gradiente de presión medio actuando en la dirección longitudinal x. La velocidad media en esa dirección es U, mientras que las componentes de las fluctuaciones de velocidad en x y z son u y w. La dirección perpendicular a la pared es y, con origen en una de las paredes, y su correspondiente componente de la velocidad es v. Las velocidades medias en las direcciones y y z son cero. Las componentes de la vorticidad son ω_x, ω_y y ω_z. La velocidad de fricción es u_τ, definida a partir de la cortadura en la pared. Las variables adimensionalizadas con la velocidad de fricción y la viscosidad ν están en unidades de pared, y se indican con un superíndice $^+$.

La teoría clásica

La teoría clásica para la turbulencia de pared puede encontrarse en distintas monografías, como por ejemplo Tennekes & Lumley (1972), Townsend (1976) o Schlichting (1979). Esta teoría se desarrolla a partir de los trabajos de Prandtl (1904, 1914), en los que se demuestra que la viscosidad siempre es importante en una capa delgada cercana a la pared. De esta forma, la presencia de paredes sólidas en el flujo impone dos escalas de longitud. En primer lugar tenemos la escala de longitud de la zona exterior, que para el caso de canales turbulentos es la semi-altura del canal, h (para otras geometrías canónicas esta longitud es R o δ, como se observa en la figura 1.1). En segundo lugar, la escala de longitud relevante cerca de la pared es la escala de longitud viscosa, ν/u_τ, donde u_τ es la velocidad de fricción. La energía se introduce en el flujo a través del gradiente de presión medio, que actúa sobre escalas del orden h, mientras que la disipación turbulenta tiene lugar en escalas del orden de ν/u_τ. De esta forma, estas dos escalas de longitud actúan como las escalas integrales y disipativas de la *cascada de energía* de la teoría de Kolmogorov (1941), aunque en este caso la presencia de la pared las segrega en el espacio.

El análisis dimensional de la ecuación de cantidad de movimiento para la velocidad media muestra que los flujos turbulentos de pared puede separarse en distintas zonas. En primer lugar tenemos una zona de la pared o región interior, donde la velocidad media sólo depende de la velocidad de fricción u_τ y de la escala de longitud ν/u_τ. Esta ley, que aparece en la ecuación (1.11), recibe el nombre de *ley de la pared*.

Como ya hemos mencionado, en este momento disponemos de una descripción bastante completa de la estructura y la dinámica de la turbulencia en la zona cercana a la pared, $y^+ \lesssim 100$. Las estructuras de velocidad características de esta zona del flujo son estrías o bandas de $u > 0$ y $u < 0$, alargadas en la dirección x y con anchuras típicas del orden de $z^+ \approx 100$ (Kim *et al.*, 1971). Asociados a estas estrías aparecen varios torbellinos orientados en la dirección del flujo (Robinson, 1991*b*; Jiménez & Moin, 1991). Las estrías y los torbellinos se relacionan en un *ciclo autónomo de energía*, que no necesita ser asistido por la zona exterior del flujo (Jiménez & Pinelli, 1999). Los torbellinos generan las estrías al interaccionar con el perfil de velocidad medio (Blackwelder & Eckelmann, 1979), alejando de la pared fluido con baja cantidad de movimiento y acercando a la pared fluido con velocidad alta. El ciclo se cierra con una inestabilidad varicosa de las estrías, que genera nuevos torbellinos que son orientados en la dirección x por el gradiente de velocidad medio (Schoppa & Hussain, 2002; Kawahara *et al.*, 2003).

Por otro lado tenemos la zona exterior, donde el análisis dimensional indica que la diferencia entre la velocidad media y la velocidad máxima sólo depende de la velocidad de fricción u_τ y del espesor del flujo h. Esta ley, que aparece en la ecuación (1.13), recibe el nombre de *ley de defecto de velocidad* (von Kármán, 1930). Entre la zona exterior y la zona cercana a la pared aparece la zona de intermedia o de solape. En ella son válidas tanto la ley de la pared como la ley de defecto de velocidad, lo que implica que la velocidad media en esta zona varía como el logaritmo de la

distancia a la pared (von Kármán, 1930; Millikan, 1939). Esta ley aparece expresada en (1.15), y es la causa de que la zona de solape también reciba el nombre de *zona logarítmica*.

En principio, la pared segrega las estructuras turbulentas del flujo: las estructuras pequeñas pueden residir cerca de la pared, mientras que las estructuras grandes son forzadas a residir en la zona exterior. La zona de la pared también es la zona más activa del flujo, generando más del 35% de la energía turbulenta del flujo en un volumen que corresponde al 17% del total. Esto es debido a que tanto el gradiente de velocidad como los esfuerzos de Reynolds son mayores en la zona de la pared que en el resto del flujo. Parte de esta energía turbulenta se disipa localmente, pero el resto es transportado a la zona exterior por un flujo de energía constante a través de la zona logarítmica. Esta cascada de energía adicional recibe en nombre de *cascada de energía inversa*, y aparece superpuesta a la cascada de Kolmogorov local.

Mientras que disponemos de una descripción bastante completa de la cinemática y la dinámica de la zona de la pared, nuestro conocimiento de las zonas exterior y de solape es casi exclusivamente cinemático. Sabemos que en la zona de solape se generan estructuras de velocidad longitudinal muy alargadas, cuya densidad espectral de energía varía como el inverso del número de onda (Perry *et al.*, 1986). La zona exterior también está poblada por estructuras de velocidad longitudinal muy alargadas (Townsend, 1958; Grant, 1958; Kovasznay *et al.*, 1970; Perry & Abell, 1975; Brown & Thomas, 1977; Perry *et al.*, 1986; Kim & Adrian, 1999). Estas estructuras reciben el nombre de *modos globales*, ya que muestran correlaciones muy elevadas desde la zona exterior hasta la pared (Bullock *et al.*, 1978; del Álamo & Jiménez, 2003). La densidad espectral de energía de la componente longitudinal del flujo también esta bastante bien caracterizada (del Álamo *et al.*, 2004). En la zona logarítmica la energía se concentra en longitudes de onda a lo largo de la linea $\lambda_x y \sim \lambda_z^2$, que se satura en $\lambda_z \sim h$ para dar lugar a los modos globales. Sin embargo, pese a disponer de una descripción cinemática aproximada de las zonas logarítmica y exterior, aún no se ha descrito un modelo dinámico satisfactorio.

Es importante tener en cuenta que la teoría clásica para la turbulencia de pared predice que las estructuras de las zonas logarítmica y exterior son independientes de la naturaleza de la pared, en particular de su rugosidad. Perry & Abell (1977) fueron los primeros en publicar estos argumentos bajo el nombre de *hipótesis de Townsend*, puesto que es una extensión del concepto de similitud de pared de Townsend. De acuerdo con estos autores, la rugosidad solamente afecta a una capa delgada, la subcapa rugosa. Por encima de ella, los movimientos a números de Reynolds altos son independientes de la rugosidad de la pared y de la viscosidad, excepto por el papel que juegan en determinar la velocidad en la parte superior de la zona de pared. Esto implica que, aparte del efecto de la rugosidad en el perfil medio, no deberían de observarse otras diferencias entre flujos sobre paredes lisas o rugosas.

De esta forma, los argumentos dimensionales que proporcionan el perfil de velocidad medio sobre paredes lisas cambian poco cuando se aplican a paredes rugosas. El análisis de la subcapa rugosa indica que la velocidad media tiene que depender

de la velocidad de fricción, de la escala viscosa y de una serie de parámetros que caractericen completamente la rugosidad, como se muestra en la ecuación (1.17). Los argumentos que proporcionan la ley de defecto de velocidad en la zona exterior también son aplicables a paredes rugosas, siempre que la longitud característica de la rugosidad k sea mucho menor que el espesor del flujo, $k/h \ll 1$. La ley logarítmica se obtienen de forma análoga al caso de paredes liso, excepto por el hecho de que la constante A en (1.15) pasa a depender de los parámetros que definen la rugosidad, como puede comprobarse en la ecuación (1.18). De esta forma, el efecto de la rugosidad en el perfil medio es un defecto constante de velocidad en las zonas logarítmica y exterior, ΔU, que depende de los parámetros que definen la rugosidad.

En los flujos turbulentos sobre paredes rugosas se identifican normalmente tres regímenes, en función de la dependencia de ΔU con el número de Reynolds de la rugosidad, $k^+ = ku_\tau/\nu$. Cuando la longitud característica de la rugosidad k es inferior a la escala de longitud viscosa ($k^+ \lesssim 5$) tenemos que $\Delta U \approx 0$. En este caso, el efecto de la rugosidad es despreciable y se dice que el flujo es hidráulicamente liso. Cuando el número de Reynolds de la rugosidad k^+ es muy grande estamos ante rugosidad completamente desarrollada. Este régimen se caracteriza porque el coeficiente de fricción se hace independiente del número de Reynolds y $\Delta U^+ \propto \log(k^+)$. Para valores intermedios de k^+ estamos en el régimen transicional. Los valores que delimitan estos tres regímenes dependen de la forma y densidad de los elementos rugosos, aunque para rugosidad *de arena* (obtenida pegando granos de arena de un tamaño uniforme a una superficie lisa, como en Nikuradse, 1932)) los límites comúnmente aceptados son $k_s^+ = 5$ y $k_s^+ = 70$.

Canales turbulentos con perturbaciones de velocidad en las paredes.

La teoría clásica de la turbulencia de pared, en concreto la hipótesis de Townsend, ha sido cuestionada durante las ultimas décadas. Krogstad *et al.* (1992) midieron en capas limites turbulentas sobre una pared en la que se habían pegado una serie de barras transversalmente al flujo. Sus mediciones muestran que en la zona exterior, las fluctuaciones de v son más intensas sobre paredes rugosas que sobre paredes lisas. Esto sugiere que la rugosidad es capaz de modificar las estructuras turbulentas que contribuyen a los esfuerzos de Reynolds en la zona exterior. En un artículo posterior, Krogstad & Antonia (1994) relacionaron estos cambios con un acortamiento de la función de correlación de la componente longitudinal de la velocidad. Finalmente, en Krogstad & Antonia (1999) se obtuvieron resultados similares para una rugosidad distinta. Además, mostraron que los esfuerzos de Reynolds asociados a eventos con $u > 0$ y $v < 0$ era mayores sobre paredes rugosas que sobre paredes lisas, produciendo diferencias en la distribución espectral de energía de v y de uv.

Otros estudios en canales turbulentos, como Djenidi *et al.* (1994) o Poggi *et al.* (2003) también muestran resultados consistentes con Krogstad *et al.* (1992) y en contra de la hipótesis de semejanza de Townsend. Finalmente, simulaciones numéricas

en canales turbulentos con elementos rugosos grandes ($k/h \approx 0.1 - 0.2$) en una sola pared (Bhaganagar & Kim, 2003; Leonardi *et al.*, 2003; Orlandi *et al.*, 2003) también muestran cambios en la estructura de la turbulencia en la zona exterior. Sin embargo, en en estas simulaciones no está claro si las diferencias en la zona exterior se deben la asimetría del canal o al efecto directo de la rugosidad en el flujo (Hanjalić & Launder, 1972).

También podemos encontrar en la literatura distintos trabajos que muestran resultados consistentes con la hipótesis de Townsend, tanto en canales como en capas límites. Los artículos de Keirsbulck *et al.* (2002), Flack *et al.* (2005), Bakken *et al.* (2005) o Ashafarian *et al.* (2004) son algunos ejemplos. En los artículos de Raupach *et al.* (1991) y Jiménez (2004) pueden encontrarse más referencias.

Dentro de esta controversia acerca de la hipótesis de Townsend, en esta tesis se han realizado una serie de simulaciones numéricas directas (DNS) de canales turbulentos con números de Reynolds del orden de $Re_\tau = u_\tau h/\nu \sim 600$. En estas simulaciones, las condiciones de contorno habituales para paredes lisas (impermeabilidad y no deslizamiento) han sido sustituidas por una serie fluctuaciones de velocidad fijas, asociadas a un número de onda dado, con el objetivo de perturbar la dinámica de la zona cercana a la pared. Después de una serie de simulaciones preliminares con el objetivo de seleccionar el forzado más adecuado, en esta tesis se presentan resultados correspondientes a tres forzados distintos. Los dos primeros son forzados donde $u = -v \neq 0$ en la pared, mientras que se mantiene $w = 0$. El tercer forzado se aplica a las tres componentes de la velocidad, manteniendo $u = -v$ y desfasando media longitud de onda el forzado en w. De esta forma, estos tres forzados proporcionan esfuerzos tangenciales de Reynolds negativos en la dirección del flujo, mientras que los esfuerzos tangenciales transversales son cero en media.

Los principales parámetros de estas simulaciones están recogidos en la tabla 2.1. Se han realizado cuatro simulaciones con perturbaciones en las paredes. Las tres primeras, correspondientes a los tres forzados descritos en el párrafo anterior, tienen unos periodos en las direcciones x y z (o dominio computacional, $L_x \times L_z = 4\pi h \times 2\pi h$) insuficientes para capturar las estructuras mas largas de la zona exterior, los modos globales. Por este motivo, se ha realizado una simulación en un dominio computacional mayor para el forzado intermedio ($L_x \times L_z = 8\pi h \times 4\pi h$). La tabla 2.1 también incluye los parámetros del caso de referencia con paredes lisas, un DNS de un canal turbulento con $Re_\tau = 550$ realizado por del Álamo *et al.* (2004) en un dominio computacional grande.

Cuando comparamos los perfiles de velocidad de los casos con paredes perturbadas con el caso de referencia (ver figura 2.1) observamos que su comportamiento es cualitativamente similar al observado en flujos sobre paredes rugosas. Aparece un defecto de velocidad constante ΔU en las zonas de solape y exterior, mientras que el perfil de velocidades de los distintos casos colapsa en una sola línea cuando lo expresamos en forma de defecto, $U^+ - U_c^+$ (U_c es la velocidad en el centro del canal). Por lo tanto, se han caracterizado los DNS de canales turbulentos con paredes perturbadas como flujos sobre paredes rugosas. Se ha definido una rugosidad

equivalente de arena k_s, y se ha modificado la coordenada normal a la pared con un desplazamiento en el origen δ_y. Este tipo de ajustes son habituales en flujos sobre paredes rugosas, donde la definición de un origen de coordenadas para y en la superficie rugosa no es inmediata (ver Thom, 1971; Jackson, 1981).

En la tabla 2.1 aparecen resumidos los valores de los parámetros que caracterizan a los casos con perturbaciones en la pared como flujos sobre paredes rugosas. Podemos comprobar que dos de los forzados proporcionan valores de k_s^+ que corresponden al régimen de rugosidad completamente desarrollada, mientras que el forzado restante corresponde al régimen transicional.

El análisis de los perfiles de fluctuaciones turbulentas de u y ω_x (figuras 2.2*a* y *b*) muestra que, debido al efecto directo de las perturbaciones en las paredes, el ciclo autónomo de energía característico de la zona de la pared no está presente en los casos con rugosidad completamente desarrollada. En estos casos, las estrías de la zona de la pared se acortan, y los torbellinos asociados a estas estrías pierden intensidad. El cociente entre la producción de energía turbulenta y la disipación también muestra la desaparición de la actividad del ciclo de la pared (figura 2.2*c*), y de hecho el flujo de energía en la zona cercana a la pared también se ve reducido por el efecto de las perturbaciones en la pared (figura 2.2*d*). Sin embargo, pese a los importantes cambios que las perturbaciones provocan en la zona cercana a la pared, las fluctuaciones turbulentas en la zona exterior son iguales en los casos lisos y rugosos (figura 2.3).

Las velocidades de advección de la componente de la vorticidad en la dirección normal a la pared, ω_y, tampoco se ven afectadas por la rugosidad en la zona exterior del flujo (figura 2.4), aparte del defecto de velocidad constante impuesto por la rugosidad en la velocidad media del flujo. En el límite de estructuras muy alargadas, esta componente de la vorticidad se corresponde aproximadamente con la velocidad longitudinal. Por este motivo, la velocidad de advección de ω_y puede interpretarse como un indicador de primer orden de la dinámica de las estructuras de velocidad muy alargadas de las zonas logarítmica y exterior.

Se ha prestado especial interés al análisis del flujo alrededor de las zonas de succión y soplado impuestas por el forzado en las paredes. Los campos instantáneos de velocidad muestran zonas localizadas donde la velocidad longitudinal total es negativa y el flujo está separado. Para poder analizar cuantitativamente esta parte del flujo se han calculado los campos de velocidad media alrededor de la unidad mínima del forzado, $\mathbf{u}_B(x, y, z)$. Estos campos son periódicos en x y z, con longitudes de onda máximas iguales a la longitud de onda del forzado, y solo contienen una zona de succión y una de soplado. El análisis de estos campos medios nos han permitido observar que las perturbaciones introducidas en la pared decaen exponencialmente con la distancia normalizada con la longitud de onda del forzado (ver ecuación 2.5 y figura 2.6*a*). El análisis de los espectros de energía filtrados a los números de onda del forzado y sus armónicos muestra que las fluctuaciones asociadas al forzado dominan al resto de fluctuaciones turbulentas en la subcapa rugosa. El espesor de esta subcapa escala con una distancia definida a partir de la distribución de esfuerzos

de Reynolds $\overline{(u_B v_B)}$ (ver ecuación 2.6 y figura 2.6b).

A continuación, la recuperación de las fluctuaciones de velocidad fuera de la subcapa rugosa es analizada en detalle, utilizando la densidad espectral de energía ϕ_{uu} y los coeficientes de correlación ρ_{uu} y ρ_{vv}. La comparación entre los espectros de los casos lisos y rugosos (figura 2.7) muestra que una vez nos encontramos fuera de la subcapa rugosa, las diferencias entre las distintas simulaciones son mínimas. Las mismas conclusiones se pueden sacar de las correlaciones de u y de v, que se muestran en la figura 2.8. En esta última figura se puede observar que para separaciones largas ($\delta x > 10y_0$) las funciones de correlación del caso liso y rugoso difieren. De hecho, el espectro de u que aparece en la figura 2.7(a) muestra diferencias similares para longitudes de onda en el rango $\lambda_x > 6h$ y $\lambda_z > h$.

El análisis de ρ_{uu} muestra que estas longitudes de onda corresponden a los modos globales, previamente identificados sobre paredes lisas por Bullock *et al.* (1978) y del Álamo & Jiménez (2003). La altura de correlación, definida como la integral doble del coeficiente de correlación desde la pared al centro del canal (ver ecuación 2.9), indica una correlación muy alta entre la pared y el centro del canal. La intensidad de estos modos en unidades de pared es menor en los casos rugosos que en el liso, debido al efecto del forzado en el perfil de velocidad medio. Es importante tener en cuenta que la rugosidad sólo afecta a la intensidad de estos modos, mientras que su forma permanece igual (ver figura 2.10).

Del Álamo *et al.* (2004) propusieron que la intensidad de estos modos escalaba con la velocidad en el centro del canal. De esta forma, las fluctuaciones de u a una altura y/h dada crecían linealmente con U_c^2. La figura 2.11 muestra los datos de las simulaciones con perturbaciones de velocidad en las paredes, así como datos de una selección de canales y tubos turbulentos a distintos números de Reynolds y rugosidades. Podemos observar como la escala de velocidad U_c^2 no colapsa los datos sobre paredes rugosas. Sin embargo, la escala de velocidad $u_\tau \log Re_\tau$ parece ser capaz de unificar los resultados de paredes lisas y régimen transicionalmente rugoso en una única curva. Es sorprendente que, al menos para Re_τ moderados, las fluctuaciones de u de los casos con rugosidad completamente desarrollada también parecen mostrar una dependencia lineal con $u_\tau \log Re_\tau$. En principio, podría argumentarse que los datos de Bakken *et al.* (2005) muestran una saturación para $(u'^2)^+ \approx 3$. Sin embargo, se necesitan datos con números de Reynolds más altos en el régimen de rugosidad completamente desarrollada para poder sacar conclusiones firmes.

La organización de los racimos de torbellinos en la zona exterior de canales con perturbaciones en las paredes

Después de analizar la estructura de la velocidad en los canales turbulentos con perturbaciones en la pared, hemos volcado nuestra atención en el efecto que las perturbaciones tienen en los torbellinos de la zona exterior. El interés de estas estructuras está motivado porque, según una serie de modelos teóricos (Perry & Chong, 1982; Perry *et al.*, 1986; Townsend, 1976), las interacciones entre las zonas de la

pared y exterior están dominadas por torbellinos que comunican ambas zonas. Estos torbellinos suelen tener forma de Λ o de herradura, y están inclinados en la dirección del flujo. Aunque inicialmente estas teorías estaban desarrolladas para estructuras de velocidad promediadas, la identificación en flujos turbulentos con números de Reynolds bajos de torbellinos con forma de Λ o de herradura (Robinson, 1991*b*; Blackburn *et al.*, 1996; Chong *et al.*, 1998; Adrian *et al.*, 2000; Ganapathisubramani *et al.*, 2003) favoreció el renacimiento de estas teorías, pero aplicadas a estructuras instantáneas del flujo.

Especialmente relevante es el artículo de Adrian *et al.* (2000), en el que se presenta un modelo para la turbulencia de pared basado en paquetes de torbellinos de herradura que crecen desde la zona de la pared. Los torbellinos que forman cada paquete trabajan cooperativamente para generar las rampas de baja velocidad observadas por Meinhart & Adrian (1995). Estos paquetes se regeneran por un mecanismo no-lineal (Zhou *et al.*, 1999), y crecen de forma auto-semejante en un proceso complejo que incluye la auto-inducción de los propios torbellinos de herradura y las uniones entre torbellinos vecinos (Tomkins & Adrian, 2003).

Este modelo es distinto del propuesto por del Álamo *et al.* (2006), en el que los torbellinos aparecen en estructuras (*racimos*, según la notación de estos autores) mucho mas complejas que las propuestas por Adrian *et al.* (2000). En un trabajo anterior, Tanahashi *et al.* (2004) ya habían observado racimos de torbellinos similares a los observados por del Álamo *et al.* (2006). El campo de velocidad medio condicionado a estos objetos muestra una estela de baja velocidad con forma de cono, que se extiende aguas abajo. En la posición del racimo de torbellinos aparece un torbellino con forma de Λ con una eyección entre sus patas. La propuesta de del Álamo *et al.* (2006) es que los racimos son marcadores de erupciones de fluido desde las capas inferiores del flujo, y son estas erupciones las que forman las estelas de baja velocidad. Según sus estimaciones, los tiempos de vida asociados a esas erupciones son cortos, por lo que resulta complicado que sean originadas cerca de la pared.

Es importante tener en cuenta que el modelo propuesto por Adrian *et al.* (2000) es difícil de reconciliar con la teoría clásica, y en concreto con la hipótesis de Townsend. Puesto que los torbellinos de herradura se generan en la pared, debería ser posible cambiar la estructura de la turbulencia en la zona exterior modificando las propiedades de los torbellinos cuando se generan. Los canales con perturbaciones en las paredes desarrollados en esta tesis son candidatos excepcionales para analizar estas cuestiones, debido a los profundos cambios que el forzado impone en la zona cercana a la pared.

En esta tesis, hemos aplicado los criterios de identificación de torbellinos desarrollados por del Álamo *et al.* (2006) a nuestra base de datos de canales con perturbaciones en las paredes. Puesto que la presencia del forzado cambia las propiedades de conectividad de los torbellinos en la subcapa rugosa, y puesto que nuestro interés se centra en las erupciones de velocidad que marcan estos torbellinos, el método desarrollado por del Álamo *et al.* (2006) ha sido modificado para analizar sólo la

zona del flujo por encima de 50 unidades de pared.

Los racimos extraídos de los canales con perturbaciones en las paredes se separan de forma natural en dos familias (ver figura 3.1*b*), igual que sobre paredes lisas. Por una lado, la función de de densidad de probabilidad de las distancias máximas y mínimas de los puntos que forman cada racimo $p_V(y_{\min}, y_{\max})$, muestra una familia de racimos que están ligados a las paredes, con puntos por debajo de $y^+ = 50$. El resto de p_V aparece distribuido en una franja con $y_{\max} - y_{\min}$ uniforme, correspondiente a racimos desligados, que no llegan hasta las paredes.

Los racimos desligados son estructuras disipativas, tanto sobre paredes lisas como sobre las paredes con perturbaciones. Su tamaño es proporcional a la escala de Kolmogorov, y sus tamaños coinciden razonablemente bien con la densidad espectral de enstrofía (ver figura 3.3). Su forma y densidad recuerda a la de los *gusanos* de la turbulencia isótropa, identificados por Jiménez & Wray (1998), y no depende de los detalles de la pared.

La familia de racimos ligados es en principio más interesante. Puesto que se trata de estructuras que llegan a la pared, se podría esperar que la modificación de la condición de contorno pudiera cambiar su dinámica. Sin embargo, los resultados que se presentan en las figuras 3.4, 3.5, 3.6 y 3.7 muestran que este no es el caso. Independientemente de los detalles de la pared, los racimos de torbellinos ligados suficientemente grandes exhiben una distribución de tamaños auto-semejante, con longitudes y anchuras proporcionales a sus alturas (ver ecuación 3.2 y figura 3.4). Igual que en el caso de pared lisa, se trata de estructuras con esfuerzos de Reynolds más intensos que la media (ver figura 3.5). La densidad de racimos ligados tampoco varían con el forzado en la pared, como indica la figura 3.6, y el efecto del umbral de detección α es igual en los casos lisos y rugosos.

El único efecto de la pared en estos objetos parece estar en su forma, que es ligeramente menos alargada en la dirección longitudinal en las cercanías de la pared, como se observa en la figura 3.7(a). Sin embargo, estas diferencias no están asociadas al efecto directo de las perturbaciones sobre los racimos, sino al cambio en el gradiente de velocidad medio en la subcapa rugosa.

El hecho de que las propiedades de los racimos ligados sean independientes de los detalles de la pared, sugiere que estos objetos se crean con tamaños similares a los observados, o que se *olvidan* rápidamente de sus orígenes. En principio, estas dos explicaciones no son necesariamente excluyentes. Mientras que los tiempos de vida de los racimos ligados presentados en del Álamo *et al.* (2006) respaldan la primera explicación, los resultados del modelo lineal que se describe en el último capítulo de esta tesis sugieren que, en media, la evolución de las eyecciones asociadas a los racimos ligados se hace auto-semejante en tiempos muy cortos.

Los campos de velocidad condicionados a racimos ligados sí muestran diferencias significativas, aunque la estructura del campo fluido medio que rodea a los racimos es similar: una estela de baja velocidad que se extiende fundamentalmente aguas abajo del racimo, abriéndose con forma de cono, y flanqueada por dos zonas de alta velocidad (ver figura 3.8). Sin embargo, la parte de la estela de baja velocidad que

se extiende aguas arriba del racimo es más corta en los casos con perturbaciones que en el caso de paredes lisas (ver figuras 3.8 y 3.9). De nuevo, este acortamiento de la estructura de velocidad en la subcapa rugosa no se debe al efecto directo de las perturbaciones, sino a la modificación del gradiente de velocidad.

El otro efecto interesante es la menor intensidad de las estelas para el caso rugoso en la zona lejos aguas abajo del racimo, medida como la velocidad media en el interior de la estela (ver figura 3.11). Debido al bajo número de Reynolds de las simulaciones presentadas en esta tesis, las estelas alcanzan alturas comparables a la altura del canal relativamente cerca del racimo. Esta zona *saturada* de la estela se corresponde con los modos globales mencionados anteriormente. Ya hemos visto que su intensidad es ligeramente menor en los casos con rugosidad que en los casos con paredes lisas. Los campos de velocidad condicionados a racimos muestran que las componentes de velocidad longitudinal y normal a la pared están muy correladas, confirmando la relación entre los modos globales y la parte de las estelas de baja velocidad con anchuras del orden del espesor del flujo.

Modelo lineal para la zona logarítmica

En el último capítulo de esta tesis intentamos sintetizar las conclusiones obtenidas en los capítulos anteriores en un modelo sencillo que explique la dinámica de las estructuras de la zona logarítmica. Nuestro parecer es que los modelos existentes hasta el momento están incompletos, ya que, como hemos visto en el capítulo anterior, no son capaces de explicar todas las observaciones.

En primer lugar, tenemos el modelo de paquetes de torbellinos de herradura propuesto por Adrian *et al.* (2000). El inconveniente principal de este modelo es la propagación y crecimiento auto-semejante de los paquetes en el seno de un flujo turbulento. Las evidencias de un proceso de regeneración de los paquetes fueron obtenidas por Zhou *et al.* (1999) en un flujo laminar con viscosidad molecular, y es discutible que ese proceso puede extrapolarse a un flujo turbulento real. Además, incluso en ese entorno tan favorable, los paquetes de torbellinos de herradura no se propagan demasiado en la dirección normal a la pared. Finalmente, aunque no menos importante, no es sencillo imaginar un torbellino con forma de herradura, con un diámetro proporcional a la escala de Kolmogorov, extendiéndose a lo largo de toda la zona logarítmica de un flujo turbulento con un número de Reynolds alto sin perder su coherencia espacial durante tiempos largos.

En segundo lugar, tenemos el modelo de racimos, erupciones y rampas propuesto por del Álamo *et al.* (2006). Este modelo se basa en estructuras que son intrínsecamente turbulentas, y que sólo se parecen a un torbellino de herradura cuando se realiza algún tipo de promedio. Además, el elemento dinámicamente relevante en este modelo no es el racimo de torbellinos, sino la erupción que está marcando. Sin embargo, en este modelo no esta claro como se produce la alineación de los racimos/erupciones para formar las estelas de baja velocidad, ni si las estelas son la causa o el efecto de las erupciones.

Es importante tener en cuenta que ambos modelos son equivalentes desde el punto de vista cinemático, y que las diferencias entre ellos se reducen fundamentalmente a cuestiones dinámicas: ¿Vienen estas estructuras de la pared? ¿Qué coherencia temporal tienen? ¿Quién origina a quien?

Para aclarar estas cuestiones, planteamos un problema sencillo: la generación de estelas de baja velocidad a partir de una versión idealizada de una erupción, utilizando las ecuaciones de Navier-Stokes linealizadas. El uso de las ecuaciones linealizadas se justifica con el análisis de los órdenes de magnitud de los términos de la ecuación de cantidad de movimiento. El tiempo asociado a la cortadura media es mucho más corto que el tiempo de giro de las estructuras ligadas a la pared de la zona logarítmica, por lo que su dinámica es esencialmente lineal. Además, el hecho de que se trate de estructuras alargadas, con longitudes características en la dirección del flujo mayores que en las direcciones transversales, permite una serie de simplificaciones adicionales (ver ecuaciones 4.3–4.5). Finalmente, el efecto de las interacciones no lineales de la estructura consigo misma y con la turbulencia del ambiente se introduce en el modelo como una viscosidad turbulenta, que básicamente limita el crecimiento máximo de la estructura. Es importante tener en cuenta que la introducción de la viscosidad turbulenta en las ecuaciones implica que, en vez de modelar la evolución de una estructura instantánea del flujo, el problema que nos planteamos es la dinámica de una estructura media.

Cuando consideramos las ecuaciones linealizadas en una zona logarítmica ideal con viscosidad turbulenta, la ausencia de una escala de longitud fija nos permite expresar la ecuación de cantidad de movimiento y de la continuidad en forma auto-semejante (ver ecuaciones 4.6–4.8). La solución crece linealmente con el tiempo en el plano transversal a la dirección media del flujo, debido al efecto de la viscosidad turbulenta lineal. En la dirección del flujo, la solución se estira bajo el efecto del gradiente de velocidad medio, que varía como el inverso de la distancia a la pared.

Estos comportamientos cualitativos también se observan en las soluciones numéricas del modelo lineal. En ellas se resuelven las ecuaciones linealizadas (4.3)-(4.5) en la zona de la pared de un flujo turbulento con un número de Reynolds virtualmente infinito ($Re_\tau = 10^9$). El dominio computacional empleado es periódico en la dirección transversal al flujo, y está truncado en la dirección normal a una altura suficientemente grande como para no influir en las estructuras que se desarrollan en el flujo. Como condición inicial empleamos una versión idealizada de las estructuras de velocidad condicionadas a racimos ligados que presentamos en el capítulo 3: un par de torbellinos longitudinales, ligados a la pared, generando una zona de v positiva 3 veces más larga que alta y 1.5 veces más ancha que alta. De esta forma, la condición inicial sólo depende de un parámetro, la distancia a la pared del centro de ese par de torbellinos, y_0. Simulaciones preliminares mostraron que la forma particular de la condición inicial no era determinante en la estructura de la solución, que tendía a una evolución auto-semejante tras en un tiempo del orden del tiempo de giro característico de la condición inicial.

Hemos considerado distintos tamaños de la erupción inicial en las simulaciones

lineales, con y_0^+ igual a 25, 50, 100, 200 y 400. En todos estos casos, la evolución del sistema es cualitativamente similar. En el instante inicial toda la energía está en las componentes de velocidad v y w. Sin embargo, la energía en estas componentes decae en más de un orden de magnitud durante el primer giro de la erupción. Mientras la viscosidad turbulenta disipa la erupción, levanta flujo lento de la zona de la pared, generando una estructura de baja velocidad longitudinal. La energía de esta estructura de u crece hasta alcanzar un máximo, para después decaer a un ritmo ligeramente inferior al de v y w: cuando la energía en v y w se ha reducido por un factor de 10^2, la componente de velocidad u aún contienen entre un 10 y un 30% de la energía inicial (ver figura 4.1).

Las energías máximas obtenidas en el proceso dependen del porcentaje (β) de los esfuerzos de Reynolds que se modelan con la viscosidad turbulenta. En la figura 4.1(b) podemos comprobar que pasar de $\beta = 1.0$ (turbulento) a $\beta = 0.0$ (laminar) implica un aumento en la amplificación de energía en más de un orden de magnitud para todos los valores de y_0 contemplados en este estudio. Además, mientras que $\beta > 0$, las erupciones más pequeñas tienen amplificaciones mayores. Cuando $\beta = 0$, la amplificación es directamente proporcional al tamaño de la erupción. Este cambio de comportamiento está relacionado con el hecho de que los tiempos que necesita la viscosidad molecular para disipar la erupción son aproximadamente un orden de magnitud mayores que los que necesita la viscosidad turbulenta (ver figura 4.2a). Además, la aparición de una escala de longitud asociada a la viscosidad en el caso $\beta = 0$ rompe la auto-semejanza de las ecuaciones, produciendo un cambio bastante brusco en la dependencia con y_0 de los tiempos asociados a amplificación máxima cuando pasamos de $\beta > 0$ a $\beta = 0$. Cuando comparamos los tiempos integrales asociados a las soluciones del modelo lineal para distintos β con los tiempos integrales asociados a las estructuras de v de flujos turbulentos reales comprobamos que el comportamiento del modelo lineal es correcto (ver figura 4.2b) cuando $\beta = 0.6$.

Los resultados del modelo lineal arrojan serias dudas sobre la aplicación de resultados obtenidos en flujos laminares a flujos turbulentos. En concreto, los tiempos de vida para $\beta = 0$ son mucho más largos y escalan de forma distinta que los tiempos para $\beta > 0$. Por ejemplo, las simulaciones lineales de Suponitsky *et al.* (2005) indican crecimientos máximos en tiempos del orden de $2.5y_0/u_\tau$, frente a $t \lesssim y_0/u_\tau$ en nuestras simulaciones. En Zhou & Adrian (1995) se indica que torbellinos de herradura con $y_0^+ \sim 50$ se disipan en $t^+ \sim 500$, lo que corresponde a $t \sim 10y_0/u_\tau$. Finalmente, en Zhou *et al.* (1999), se indica que el tiempo en el que se genera el torbellino de herradura secundario es $t \sim 2y_0/u_\tau$, mientras que nuestros resultados indican que ese torbellino ya habría perdido del orden del 70% de su energía si $\beta = 0.3$ (90% si $\beta = 0.6$), posiblemente impidiendo el proceso de regeneración.

La figura 4.3 muestra que la evolución del sistema se vuelve auto-semejante rápidamente si la erupción inicial es suficientemente grande como para *vivir* en la zona logarítmica. También podemos observar que en ese proceso de crecimiento autosemejante, el centro de la estructura se desplaza en la dirección normal a la pared con una velocidad del orden de u_τ. Sin embargo, debido al corto tiempo de

vida de las erupciones, estas apenas consiguen doblar su tamaño inicial antes de ser disipadas por la turbulencia del entorno.

Las estructuras de u generadas en el modelo lineal son consistentes con las estelas observadas *aguas arriba* de los racimos ligados en flujos turbulentos. Sin embargo, la estela que se observa *aguas abajo* en flujos turbulentos reales no está presente en el modelo lineal. Esté es posiblemente el resultado más interesante del modelo lineal, puesto que implica que la erupción sólo es causa de la estela aguas arriba, y sugiriere que la estela aguas abajo es la causa de la erupción.

Todos estos resultados también se obtienen cuando resolvemos las ecuaciones lineales para el perfil de velocidad obtenido un los DNS con perturbaciones en las paredes. Cuando la erupción inicial es suficientemente grande, los resultados para pared rugosa tienden a los obtenidos para paredes lisas (figura 4.7), y los campos de velocidad asociados a racimos turbulentos en el caso rugoso concuerdan con los obtenidos del modelo lineal (ver figura 4.8).

Finalmente, también hemos analizado el efecto que la erupción media tiene en el perfil de velocidad local, para evaluar el origen de las erupciones. Los resultados mostrados en las figuras 4.9 y 4.10 sugieren que para deformar de forma apreciable en perfil de velocidad media necesitamos la contribución de la zona exterior. La disminución de la viscosidad turbulenta en esta zona permite el desarrollo de estructuras de u mas intensas, que podrían ser el origen de las erupciones de la zona logarítmica.

Conclusiones y trabajo futuro

En esta tesis se ha estudiado la naturaleza de las interacciones entre la zona de la pared y la zona exterior, y su papel en la dinámica de la turbulencia de pared. Para abordar este estudio se ha desarrollado una base de datos de simulaciones numéricas directas de canales turbulentos con números de Reynolds moderados, $Re_\tau \approx 600$. Las condiciones de contorno en las paredes de estas simulaciones han sido sustituidas por una distribución periódica de velocidades caracterizada por un único armónico. El efecto de estas perturbaciones es interrumpir el ciclo de energía característico de los flujos turbulentos sobre paredes lisas, cambiando completamente la naturaleza de la zona de la pared en estas simulaciones. Esto las convierte en una valiosa herramienta para analizar el efecto de la pared en la zona exterior.

El análisis de estas simulaciones indica que la hipótesis de Townsend es esencialmente válida. En la subcapa rugosa, el flujo está dominado por el forzado de la pared y sus armónicos. Sin embargo, por encima de esta subcapa rugosa la estructura de la turbulencia es independiente de la naturaleza de la pared. Hay que tener una cierta precaución al extender esta afirmación a las estructuras más largas del flujo. Nuestras simulaciones muestran que los modos globales identificados sobre paredes lisas, que están correlados desde la zona exterior hasta la zona de la pared, también están presentes en flujos sobre paredes rugosas. Su forma no se ve afectada por los detalles de la pared, aunque su intensidad sí se ve afectada por los cambios que la rugosidad impone en el perfil de velocidad medio. Utilizando

datos experimentales de flujos turbulentos en canales y tubos, con paredes lisas y rugosas, hemos comprobado que la escala de velocidad para esos modos es aproximadamente $u_\tau \log Re_\tau$. Esta escala de velocidad funciona para los casos en régimen hidráulicamente liso y transicionalmente rugoso. Sorprendentemente, los casos rugosos completamente desarrollados también parecen seguir ese escalado, aunque se necesitan datos a números de Reynolds mayores para determinar si, tal y como predice la teoría clásica, su intensidad deja de depender del número de Reynolds.

Las estructuras coherentes de vorticidad de la zona exterior tampoco se ven modificadas por el forzado en las paredes. Tanto los racimos de torbellinos ligados a la pared como los desligados tienen las mismas propiedades estadísticas en los casos lisos y rugosos. En particular, los racimos ligados son marcadores de erupciones de velocidad normal a la pared, que tienen un papel importante en la dinámica de las zonas de solape y exterior. Los campos de velocidad asociados a estas erupciones son estelas de baja velocidad con forma cónica, que dan lugar a los modos globales cuando su altura es comparable al espesor del flujo. Tampoco la rugosidad es capaz de modificar estas estelas, salvo por el acortamiento de la parte de esta estela que se desarrolla aguas arriba del racimo, en la zona cercana a la pared.

El modelo lineal presentado en el último capítulo de esta tesis permite explicar este fenómeno. De acuerdo con el análisis de los ordenes de magnitud de los términos de las ecuaciones de Navier-Stokes, el tiempo de giro de las erupciones marcadas por los racimos ligados es mucho mayor que el tiempo de deformación asociado al gradiente de velocidad media, por lo que el proceso de generación de las zonas de baja velocidad observadas en flujos turbulentos sobre paredes lisas y rugosas es esencialmente lineal. Las simulaciones lineales muestran que las erupciones son capaces de generar estelas de baja velocidad aguas arriba, y la forma y tamaño de estas estelas corresponde con las observadas aguas arriba de los racimos de torbellinos ligados, en paredes lisas y rugosas.

Sin embargo, el modelo lineal no explica como se generan las estelas aguas abajo de los racimos. De hecho, las observaciones sugieren que las erupciones son el efecto, más que la causa, de la estela aguas abajo. Además, cuando en el modelo lineal se introduce el efecto de la zona exterior, las estructuras resultantes son notablemente más energéticas. Esto es debido a la disminución de la viscosidad turbulenta en la zona exterior, lo que permite un tiempo de vida mayor para las erupciones de la zona exterior y las correspondientes rampas. Aunque deberá ser comprobado en investigaciones posteriores, lo que sugieren los resultados presentados en esta tesis es que la relación de causalidad normalmente asociada a los flujos de pared puede ser errónea. En vez de tener una zona logarítmica gobernada por las estructuras que vienen de la pared o por un ciclo autónomo, nuestra propuesta es que la zona logarítmica es relativamente pasiva, subordinada a las estructuras de la zona exterior.

Como trabajo futuro se propone el estudio de la cascada de energía en la zona logarítmica, y el análisis de la estabilidad de estructuras de velocidad instantáneas características de la zona logarítmica. Desde un punto de vista más aplicado, una posibilidad que merece ser estudiada es la aplicación de las condiciones de contorno

desarrolladas en esta tesis para emular el efecto de rugosidad real en geometrías complejas.

Chapter 1

Introduction

The problem studied in this thesis pertains to the subject of turbulence in incompressible fluids. The simplest explanation of the term *turbulence* is usually given in oppossition to *laminar*. It is commonly observed in daily situations that slow flows are well organized (laminar flow). However, when the velocity (or the length scale) increases, the flow becomes disorganized and chaotic, and the velocity and the pressure fluctuate rapidly both in time and space. In the latter case, the flow has become turbulent.

Turbulent flows are very common both in industry and in nature. For instance, they are of critical importance in processes such as the mixing of oxygen and fuel in modern combustion engines, the pressure drag in pipeline systems, the dispersion of contaminants in the atmospheric boundary layers or the formation of clouds. In addition to its practical importance, turbulence is considered as one of the modern paradigms of complexity, since it is a multiscale and dissipative problem with nonlinear interactions. The research in turbulence has made important advances during the past century, but there are still some open questions related to the underlying physical mechanisms.

The present thesis is concerned with incompressible turbulent flows in the presence of solid walls, namely wall-bounded turbulence. The phenomenology found in turbulent flows is much broader than that, including homogeneous turbulence, turbulent convection of heat and particles or the problem of shock-waves/turbulence interaction. A general approach to the problem of turbulence can be found in several monographs, like Tennekes & Lumley (1972), Hinze (1975), Townsend (1976), Frisch (1995), Lesieur (1997) and Jiménez (2000).

1.1. Historical remarks

The notion of turbulence is very old. In fact, the term *turbolenza* was a Latin word used to describe crowds. Gonzalo de Berceo used it in the XIII century to describe the weather, and later in the XVI century, Leonardo da Vinci used it to describe the disordered motion of water. However, the scientific study of turbulence began 300 years later, with the pioneering work of Hägen (1854) and Darcy (1857).

They independently analyzed the pressure drop in pipes and found that it had a quadratic component independent of the viscosity. They associated that extra component to the disordered motion of the fluid. Their results showed one of the most important properties of turbulence; even in the limit of negligible viscosity the dissipation remains constant, implying that the velocity gradient tends to infinity and the flow apparently becomes singular. In other words, turbulence is a dissipative system, and precisely this property distinguishes turbulence from other non-linear systems.

After the experiments by Hägen and Darcy, Boussinesq (1877) published a paper distinguishing between two different regimes, *smooth* and *tumultuous*. He also introduced some important features of the turbulent regime, like its enhanced dissipation and the need for a statistical description of the velocity. Later, Reynolds (1883) clarified the transition between the two regimes. He introduced dye in a water pipe and observed how the flow became disordered. He characterized the transition with the non-dimensional number that now bears his name, the Reynolds number $Re = U_b L/\nu$, where U_b is the bulk velocity, L is the distance to the entrance of the pipe and ν is the kinematic viscosity. In a later paper (Reynolds, 1894), he decomposed for the first time the flow in its mean and fluctuating part, introducing the "Reynolds stress" and the "closure problem". The simplest models for solving that problem were based on the analogy with the kinetic theory of gases, leading to the *mixing length* models (Taylor, 1921; Prandtl, 1925; von Kármán, 1930).

Roughly at the same time, Richardson (1920) proposed a multiscale description of turbulence. He postulated that the energy introduced in the turbulent flow generates large scale structures or eddies. These eddies break into smaller eddies due to some kind of instability. The process is repeated several times until the eddies are small enough for the viscosity to dissipate them. Richardson's ideas were further developed by Kolmogorov twenty years later into what is known nowadays as the *energy cascade*, which is probably the most important landmark in turbuelence research. Before that, some other important advances were made. In 1935, Taylor introduced the concept of isotropic turbulence, a turbulent flow where all flow statistical variables are independent of translation, rotation and reflexion of the axes of reference. Its importance resides in that it is the simplest form of turbulence that can be considered relevant for more realistic turbulent flows. Later, von Kármán & Howarth (1938) derived the equation that describes the transfer of energy between different wavelengths, the Kármán-Howarth's equation. This equation was used to derive the Kolmogorov's theory described in the next section.

The Kolmogorov's theory

The Kolmogorov's theory of the *energy cascade* emerges from the ideas postulated by Richardson (1920). We will focus here on the energy distribution predicted by that theory, which has been one of its most successful predictions.

Consider an isotropic and homogeneous turbulent flow, in which the energy is injected in large scale eddies. The hypothesis of the energy cascade is that each of

these eddies, with a characteristic length ℓ and a characteristic velocity u_ℓ, breaks into smaller eddies (say, of size $\ell/2$) in times of the order of their turnover time, $t_\ell = \ell/u_\ell$. The process is repeated until the Reynolds number of the eddy is small enough for the viscosity to become important and dissipate energy. The energy per unit mass transferred in the process is $u_\ell^2/t_\ell = u_\ell^3/\ell$, and if we assume that the cascade is in equilibrium, the energy transfer rate at any scale must be equal to the total dissipation ε. Under these conditions, we can estimate the characteristic velocity of a size-ℓ eddy,

$$\varepsilon = \frac{u_\ell^3}{\ell} \rightarrow u_\ell \sim (\varepsilon\ell)^{1/3}. \tag{1.1}$$

The cascade process is forced at the large scales by an energy input mechanism, which is usually characterized by the integral length scale of the velocity fluctuations, L_ϵ, defined as the integral of the velocity correlation coefficient (Batchelor, 1953, page 47). We can also define a characteristic velocity for the large scales u_L, substituting the integral length scale in (1.1),

$$\varepsilon = \frac{u_L^3}{L_\varepsilon} \rightarrow u_L = (\varepsilon L_\epsilon)^{1/3} \tag{1.2}$$

At smaller scales, the cascade process takes place without energy dissipation as far as the turnover time of the eddy t_ℓ is shorter than the time that viscosity needs to damp it, $t_\nu = \ell^2/\nu$. The Kolmogorov scale η_k is defined as the length scale for which $t_\ell = t_\nu$, resulting in

$$\frac{\eta_k}{u_k} = \frac{\eta_k^2}{\nu} \rightarrow \eta_k = \left(\frac{\nu^3}{\varepsilon}\right)^{1/4}. \tag{1.3}$$

At this scale, the break up of the eddy takes place with energy dissipation, and because of this the range of scales $\ell \sim O(\eta_k)$ is called the *dissipative range*. The range of scales where the eddies break up inviscidly ($L_\epsilon \gg \ell \gg \eta_k$) is called the *inertial range*.

The concept of energy cascade allowed Kolmogorov to obtain the scaling of spectra of the velocity fluctuations in the inertial range, $E_u(k_1) \sim \varepsilon^{2/3} k_1^{-5/3}$, where $k_1 = 1/\ell$ is the wavenumber in the direction of the velocity component u. This expression was a well known empirical law observed in turbulent flows, that remained unexplained until the work of Kolmogorov. Later, Onsager (1945) used the concept of energy cascade to show why the dissipation of turbulent flows does not tend to zero when $\nu \rightarrow 0$, solving the paradox raised by Hägen and Darcy. The idea is that according to (1.1), the velocity gradient is $u_\ell/\ell \sim (\varepsilon/\ell^2)^{1/3}$, increasing as we move to smaller scales in the inertial range. However, at the Kolmogorov scale where dissipation takes place, the velocity gradient is $u_k/\eta_k = (\varepsilon/\nu)^{1/2}$, and the volume integral of the turbulent energy dissipation

$$\frac{1}{Vol} \int_{Vol} \nu(\nabla \mathbf{u})^2 d\mathbf{x} \sim \nu \left(\frac{u_k}{\eta_k}\right)^2 = \varepsilon, \tag{1.4}$$

becomes independent of the viscosity ν, consistently with the experiments of Hägen and Darcy.

One of the most interesting aspects of the Kolmogorov's energy cascade is that, if it exists, it should be universal, common to all turbulent flows. The energy input mechanisms in real flows differ and so do the large scale structures that appear in the flow. However, as the energy is transfered towards smaller eddies, their characteristic time scales decrease. The small scales of the inertial range are too small and to fast to see the spatial and temporal variability of the large (non-universal) scales, and their evolution is controlled by the local value of the energy dissipation. These scales could be universal, since they are always in local equilibrium with the larger ones, as assumed in (1.1). The universality of the Kolmogorov's cascade is behind one the most usual techniques to simulate turbulent flows, namely Large Eddy Simulation (LES), which will be described in §1.3.

Finally, it is important to bear in mind that the Kolmogorov's energy cascade is not a deductive theory, since it is based on a set of hypothesis. A rigorous theory leading from the Navier-Stokes equations to the energy cascade process described above is yet to be developed. In fact, Batchelor & Townsend (1949) showed that some of the hypothesis used by Kolmogorov were not exact. In particular, the arguments of the energy cascade assume that probability functions of the velocity are independent of the scale. The experimental measurements of spatial velocity correlations by Batchelor & Townsend showed that the probability of extreme events was higher as the distance was decreased. This phenomenon receives the name of *intermittency*, and it was included in the modified cascade theory presented by Kolmogorov (1962) and Oboukhov (1962). An important fraction of the research in turbulence in the past century has been devoted to the analysis and description of this phenomenon (for an account of the different approaches check Frisch, 1995).

1.2. Wall-bounded turbulence

In most practical applications, turbulent flows are bounded by solid walls, making the study of wall-bounded turbulence of great importance. Because of that, wall-bounded turbulence has been investigated since the 1900's. However, some important aspects of it are not yet fully understood.

Wall-bounded turbulence is more complicated than free turbulence since the presence of walls imposes constraints that are absent in the latter. The most obvious ones are the non-slip and impermeability boundary conditions for the velocity, which introduce inhomogeneity in the flow. In order to avoid the extra complexity introduced by the geometry of the walls, the present thesis only considers the canonical wall-bounded flows (channels, pipes and boundary layers), which are sketched in figure 1.1. The flow is driven by a pressure gradient in the streamwise direction x, resulting in a mean velocity U which in principle depends only on the wall-normal coordinate y. Note that in the case of boundary layers, U also depends on x. The spanwise coordinate is z, which for pipe-flows is the arc length $z = r\theta$. The velocity

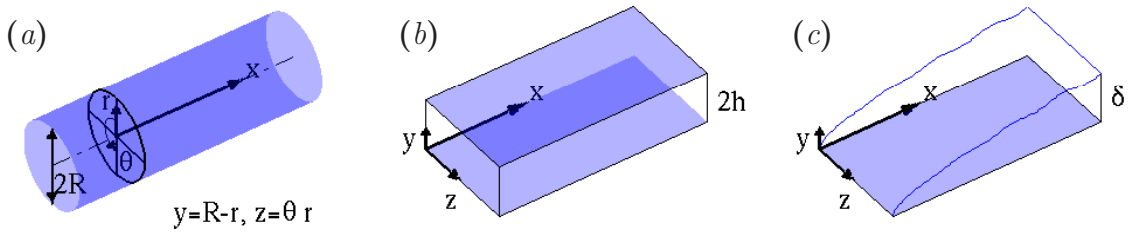

Figure 1.1: Sketch of the geometry of the canonical wall-bounded flows. (a) Pipe. (b) Channel. (c) Boundary layer.

fluctuation with respect to the mean flow is $\mathbf{u} = (u, v, w)$. The flow thickness is defined by the pipe radius R, the channel half height h or the boundary layer thickness δ. They are the characteristic length scales of the outer region of these flows, and they will be considered roughly equivalent. The spanwise direction is homogeneous in the three canonical flows, while the streamwise direction is homogeneous only in pipes and channels.

The classical theory for wall-bounded turbulent flows can be found in many text books, like Tennekes & Lumley (1972), Townsend (1976) or Schlichting (1979). It derives from the work of Prandtl, who extended his boundary layer theory (Prandtl, 1904) to turbulent flows over smooth walls. He showed that even for high Reynolds numbers, the viscosity is always important in a thin layer near the wall, and therefore turbulent flows over smooth walls never become *fully turbulent*. Furthermore, this viscous layer imposes two different length scales in the flow: the viscous length scale in the *inner region* , and the flow thickness h in the rest of the flow, the so-called *outer region*. These two length scales are analogous to the integral and dissipative scales of Kolmogorov's theory, but here the energy cascade is not only separated in scales, but also in space.

Consider the flow in a smooth-walled channel. The analysis of the boundary layer or the pipe cases is similar. The momentum equation for the mean velocity reads

$$\partial_y \overline{uv} = -\rho^{-1}\partial_x P + \nu \partial_{yy} U, \tag{1.5}$$

$$\partial_y \overline{v^2} = -\rho^{-1}\partial_y P, \tag{1.6}$$

$$0 = -\rho^{-1}\partial_z P, \tag{1.7}$$

where $\overline{(\cdot)}$ denotes ensemble averaging over the homogeneous directions.

We can integrate (1.6) and (1.7) to obtain

$$\rho^{-1}P + \overline{v^2} = \rho^{-1}P_0(x). \tag{1.8}$$

We will assume that $P_0(x)$ is linear, so that the mean pressure gradient $\partial_x P$ driving the flow in (1.5) is constant.

Substituting the mean pressure gradient in (1.5), we can integrate the total shear in the flow,

$$-\overline{uv} + \nu \partial_y U = y\rho^{-1}\partial_x P_0 + \tau_w. \tag{1.9}$$

taking into account that the viscous friction at the wall, τ_w, has to balance the mean pressure gradient. Then, since the flow is statistically symmetric with respect to the center of the channel, (1.9) at $y = h$ gives $\rho^{-1}\partial_x P_0 = -\tau_w/h$, and the total shear stress can be expressed as

$$-\overline{uv} + \nu \partial_y U = \tau_w(1 - y/h). \tag{1.10}$$

When the friction Reynolds number $Re_\tau = \tau_w^{1/2} h/\nu$ is large, the viscous shear stress $\nu\partial_y U$ is negligible in most of the flow, and the friction velocity $u_\tau = \tau_w^{1/2}$ is the velocity scale of the Reynolds stress.

Normalizing (1.10) with the friction velocity u_τ and the viscous length scale ν/u_τ, we obtain that when $Re_\tau \gg 1$, the only suitable form of the mean velocity profile in the inner region of a smooth-walled flow is

$$U^+ = f(y^+). \tag{1.11}$$

The + superscript indicates variables normalized in wall-units, using the reference velocity u_τ and the reference length ν/u_τ. Equation (1.11) is usually called the *law of the wall* (Prandtl, 1925), and was supported by early measurements by Nikuradse (1932). Later on, Reichardt (1951) extended the measurements to points very close to the wall, and found that for $y^+ \lesssim 5$ the tangential Reynolds stress was zero and the mean velocity profile was linear,

$$U^+ = y^+. \tag{1.12}$$

Figure 1.2(a) shows in blue the mean velocity profiles obtained in different turbulent channels, both numerical and experimental. We can observe that the data support both (1.11) and (1.12). It is customary to refer to the region below $y^+ \lesssim 5$ as the *viscous sublayer*, while the region between $10 \leq y^+ \leq 100$ is usually called the *buffer* or the *near-wall* region.

In the outer region the viscous shear stresses are negligible and the dimensional analysis shows that the mean velocity has the form

$$U^+ - U^+_{\max} = F\left(\frac{y}{h}\right). \tag{1.13}$$

Note that, since a constant translation velocity does not affect the dynamics of the motion, the maximum velocity of the flow $U_{\max}$ appears in (1.13). This equation was obtained by von Kármán (1930), who applied his similarity hypothesis and the mixing length concept of Taylor and Prandtl to the Reynolds averaged equations in

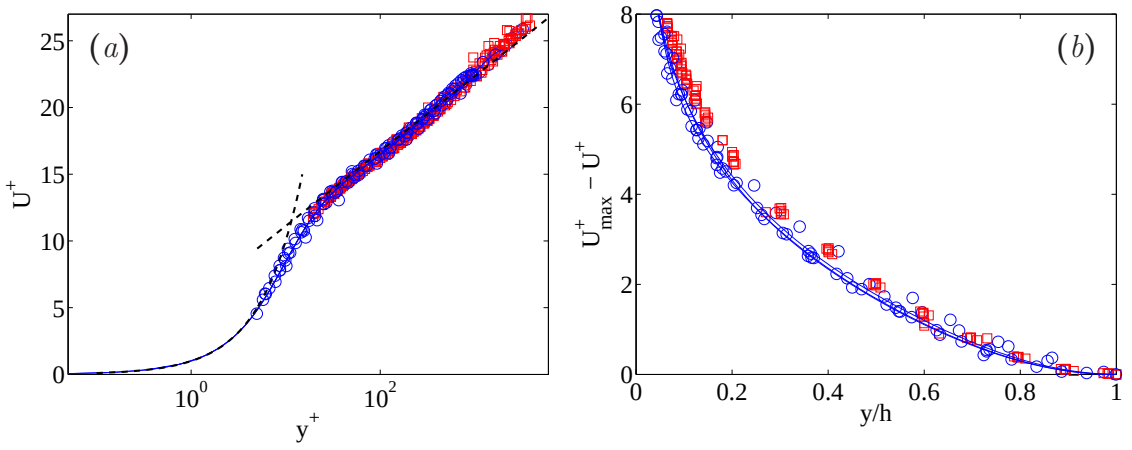

Figure 1.2: Mean velocity profiles of numerical and experimental wall bounded flows, with $Re_\tau = 500 - 5000$. (a) Inner scaling, using ν/u_τ and u_τ. (b) Outer scaling, using h and u_τ. Blue symbols correspond to experimental channel flows, from Bakken *et al.* (2005), Niederschulte *et al.* (1990) and Wei & Willmarth (1989). Blue lines correspond to numerical channel flows, from del Álamo *et al.* (2004) and Hoyas & Jiménez (2006). Red symbols correspond to experimental pipe flows, from Perry *et al.* (1986) and Perry & Abell (1977). The black, dashed lines in (a) correspond to (1.12) and (1.15).

a rectangular channel. Neglecting the effect of molecular viscosity, he computed a mean velocity profile that was only dependent on the maximum velocity, the wall distance, the channel half-height and the friction velocity. This result is known as the *velocity defect law*. Figure 1.2(b) shows the goodness of this law. Note that, since $F(y/h)$ in (1.13) depends on the geometry of the flow, the data from pipes and channels collapse into two different curves in 1.2(b).

Equation (1.13) is valid in the outer region, where $y/h \sim O(1)$. In the near-wall region, where y/h is very small, the molecular viscosity becomes important and the expression above has to be replaced with the law of the wall (1.11). In the overlap region where $y^+ \to \infty$ and $y/h \to 0$, both (1.11) and (1.13) are valid. Since these two expressions do not have any common independent variables, the matching in the overlap region is only possible if

$$\frac{y}{u_\tau}\partial_y U = y^+\frac{df}{dy^+} = \frac{y}{h}\frac{dF}{dy/h} = \kappa^{-1}, \tag{1.14}$$

which can be integrated to

$$U^+ = \frac{1}{\kappa}\log(y^+) + A. \tag{1.15}$$

Because the mean velocity profile varies as the logarithm of the wall distance, the overlap region is also called the *logarithmic region*. The characteristic length scale of the flow is the wall distance y, since h is too large ($y \ll h$) and ν/u_τ is too

small ($y^+ \gg 1$). The constant κ in (1.15) is known as the von Kármán's constant, since Theodore von Kármán was one of the first to obtain (1.15) using similarity arguments (von Kármán, 1930). In principle, κ should be universal, although the reported values for it vary from 0.35 to 0.42. The classical value of the intercept constant is $A \approx 5$, although again its value is slightly different in channels, boundary layers and pipes. The good agreement of numerical and experimental data with (1.15) can be observed in figure 1.2(a).

The process described here to obtain (1.15) is called *asymptotic matching*, and was first described by Millikan (1939). Townsend (1976) gave a different argument to derive the logarithmic velocity law, based on the concept of *equilibrium layer* (Townsend, 1961). He considered a region of the flow close to the wall, with a small thickness when compared to h, so that the variation of the Reynolds stress was small compared with the shear at the wall and the transport of energy by the mean flow was negligible. In that case, he showed that the turbulent energy production and dissipation are in approximate balance, leading to a logarithmic mean velocity profile. Another interesting observation was that the characteristic length scale increased linearly across the region of constant Reynolds stress. That was interpreted by Townsend as an indication of that the energy containing eddies of the flow in that region were *attached* to the wall, with heights and widths proportional to the distances of their centers to the wall, in agreement with the model proposed by Theodorsen (1952).

It is important to keep in mind that the logarithmic velocity law of the classical theory is a first order approximation to the mean velocity profile in the logarithmic region. Indeed, the use of u_τ as a velocity scale for the outer region may not be justified, especially in the case of boundary layers, where the shear stresses tend to zero in the outer limit. Indeed, the literature about wall-bounded turbulence offers some alternatives. For instance, Oberlack (1997) proposed a scaling for the logarithmic region which was equivalent to use no scale for the velocity, leading to an exponential law for the mean velocity. Also, George & Castillo (1997) proposed $U_{\max}$ as a velocity scale, which leads to power laws.

Flow structure and dynamics over smooth walls

As described in the previous paragraphs, we can distinguish three regions in the turbulent flow over a solid wall: the buffer region, the outer region, and the logarithmic region between them. The presence of the wall segregates the flow structures through them, so that smaller eddies reside closer to the wall than larger eddies. The analogy with the Kolmogorov's energy cascade suggests that the outer region corresponds to the integral scales, the buffer region corresponds to the dissipative range, and the logarithmic region corresponds to the inertial range. However, this analogy is not complete. The buffer region is the most active part of the flow, generating more than 35% of the total turbulent energy of the channel when it only represents 17% of the total volume. Note that both the Reynolds stresses and the mean velocity gradient are larger in the buffer region than in the outer region. Part

of the energy generated in the buffer region is dissipated locally, but the rest is exported to the outer region by a constant energy flux through the logarithmic region. This additional energy cascade is known as the *inverse energy cascade*, and appears superimposed to the local Kolmogorov's energy cascade in wall-bounded turbulent flows.

The dynamics of the buffer region below $y^+ \approx 100$ became largely understood in the last decade. The local Reynolds numbers in the buffer region are relatively low, and even if the flow is not laminar, it is at least smooth. This region is dominated by the well-documented near-wall streaks (Kim *et al.*, 1971) and quasi-streamwise vortices (Robinson, 1991*b*; Jiménez & Moin, 1991). The former ones are long, sinuous strips of alternating low and high momentum fluid. Their average spanwise separation is $z^+ \approx 100$, and their length is $x^+ \approx O(10^3)$. The quasi-streamwise vortices are staggered between the high and low velocity streaks, with a longitudinal spacing about $x^+ \approx 400$. Both, streaks and vortices, interact with the mean shear through a non-linear cycle that does not need the assistance of the outer region (Jiménez & Pinelli, 1999). In that cycle, the vortices generate the streaks by stirring the mean velocity profile (Blackwelder & Eckelmann, 1979), while an instability of the streaks generate new vortices (Schoppa & Hussain, 2002; Kawahara *et al.*, 2003). Recently Jiménez *et al.* (2005) have connected that cycle to nonlinear three-dimensional solutions of the Navier-Stokes equations in incompressible Couette (Nagata, 1990; Waleffe, 2003) and Poiselle flows (Toh & Itano, 2001; Waleffe, 2001), as well as with the autonomous channel simulations of Jiménez & Pinelli (1999) and Jiménez & Simens (2001).

The logarithmic and outer regions are less understood than the buffer region. Townsend (1976) argued that the equilibrium layer concept (Townsend, 1961) implies that the aspects of the turbulent motion related with the turbulent energy production and dissipation only depend on the velocity scale u_τ and the length scale y. This statement does not apply to the *inactive motions* (Bradshaw, 1967; Townsend, 1976), that do not contribute to the Reynolds stresses. Another important observation is that the flow structures of the logarithmic and outer regions are constrained by the wall in the y direction, but not in the wall-parallel directions, resulting in the development of elongated structures. These structures do not participate in the isotropic, local Kolmogorov's energy cascade, but they carry an appreciable fraction of the Reynolds stresses, and participate in the inverse energy cascade mentioned above.

It is possible to estimate the one-dimensional energy spectra of the streamwise velocity fluctuations due to large structures in the logarithmic region. According to the wall similarity concept, the one-dimensional energy spectrum can only depend on u_τ^2, the wavenumber k_x, and the wall-normal distance y, which is the characteristic length scale of the logarithmic region. However, since we are considering elongated structures, we have that $k_x y \gg 1$, and the only dimensionally-correct expression for the one-dimensional energy spectra is

$$E_{uu}(k_x) \sim u_\tau^2 k_x^{-1}, \tag{1.16}$$

which was carefully documented by Perry *et al.* (1986).

The outer region may also be described using wall similarity arguments, although the effect of the flow geometry should be taken into account. Therefore, in principle all flow statistics in the outer region should depend on u_τ and h. However, it is known that the flow structures of the outer region are quite large, with streamwise lengths several times longer than the flow thickness (Townsend, 1958; Grant, 1958; Kovasznay *et al.*, 1970; Perry & Abell, 1975; Brown & Thomas, 1977; Perry *et al.*, 1986; Kim & Adrian, 1999). Bullock *et al.* (1978) found that these velocity structures are highly correlated across the whole flow thickness, from the outer region to the wall, and termed them *global modes*. Because of that, it is possible that the velocity scale for those large scale motions is different from the friction velocity. Several propositions have been made in the same direction, such as the *mixed scaling* proposed by de Graaff & Eaton (2000), or the scaling for the global modes with $U_{\max}$, as proposed by del Álamo *et al.* (2004).

1.2.1. Turbulent flows over rough walls

Using the logarithmic velocity profile derived from equation (1.15), Prandtl (1935) obtained his universal drag coefficient law for smooth pipes. This law is supported by several experiments, as shown in Schlichting (1979). However, it fails to reproduce the behavior of the experiments of Hägen (1854) and Darcy (1857), where the wall friction becomes independent of the Reynolds number. The answer to this disagreement is that the pipes used by Hägen and Darcy were somewhat rough, so that the drag forces over the roughness elements overcome the viscous friction as the Reynolds number increased. This behavior only shows up in *fully turbulent* flows, and wall-bounded turbulence over smooth walls is never fully turbulent: there is always a thin layer near the wall were the local Reynolds number is $y^+ = yu_\tau/\nu \approx O(1)$, and the flow is essentially laminar. This difference between smooth- and rough-walled flows is intrinsically interesting and justifies the study of rough walls beyond their practical applications.

The classical theory for turbulent flows over rough walls is based on the wall similarity concept of Townsend, that was extended by (Perry & Abell, 1977) to conform what they called the *Townsend's hypothesis*. It states that the roughness elements only affect a thin layer above them, the *roughness sublayer*. Above it, the turbulent motions at sufficiently high Reynolds number are independent of the wall roughness and of viscosity, except for the role of the roughness sublayer in setting the mean velocity at its upper limit (Perry & Abell, 1977; Raupach *et al.*, 1991). This implies that, apart from the effect of the roughness on the mean velocity, no other differences between smooth- and rough-walled flows should be encountered in the overlap and outer regions.

The effect of the wall roughness on the mean velocity profile is well described in classical text books, like Townsend (1976) or Schlichting (1979). Indeed, the arguments presented in the previous pages for smooth-walled turbulent flows change slightly in the case of flows over rough walls. In the region close to the roughness

elements, the characteristic length scales of the flow are the viscous length scale ν/u_τ, the height of the roughness elements k, and all the additional length scales S^k needed to completely characterize the roughness. Typically, S^k includes the lateral aspect ratios of the roughness elements, and some measure of the density of the roughness elements. The rough-walled version of the law of the wall (1.11) is therefore

$$U^+ = f(y^+, k^+; S^k). \tag{1.17}$$

The arguments leading to the velocity defect law (1.13) are also valid in rough-walled flows, provided that the characteristic size of the roughness elements is small compared with the flow thickness, $k/h \ll 1$. In that case, the arguments leading to the logarithmic law also apply, but the intercept constant changes to include the influence of k^+ and S^k,

$$U^+ = \frac{1}{\kappa}\log(y^+) + C(k^+; S^k). \tag{1.18}$$

It is customary to express $C(k^+; S^k)$ emphasizing the departure of U^+ from the smooth-walled value, using the *roughness function* ΔU,

$$U^+ = \frac{1}{\kappa}\log(y^+) + A - \Delta U^+(k^+; S^k), \tag{1.19}$$

where A is the same intercept constant as used for smooth walls in (1.15). In the limit $k^+ \to 0$, $\Delta U = 0$ and $C = A$.

It is also possible to use k instead of ν/u_τ as characteristic length scale, resulting in

$$U^+ = \frac{1}{\kappa}\log\left(\frac{y}{k}\right) + B(k^+; S^k), \tag{1.20}$$

where B is a function of the roughness. When the *roughness Reynolds number* k^+ is sufficiently high, the influence of the viscous length scale can be neglected in (1.17) and (1.20), and the value of B becomes independent of k^+. Under those conditions, the flow is termed *fully rough*.

The first direct proof of this behavior was reported by Nikuradse (1933), who measured the mean velocity profiles in pipe flows over several sand roughnesses at different Reynolds numbers. He prepared his rough surfaces by gluing carefully filtered sand, so that each of the rough surfaces used by Nikuradse could be characterized by a single length scale k_s, corresponding to the size of the grains. He found that the measured mean velocity profiles could be expressed as

$$U^+ = \frac{1}{\kappa}\log\left(\frac{y}{k_s}\right) + 8.5. \tag{1.21}$$

This equation has been used as a definition of the *equivalent sand roughness* k_s, defined for a given roughness as the height of the sand roughness that gives the same B as the given roughness (Schlichting, 1979). In terms of the equivalent sand roughness, a flow can be considered fully rough for $k_s^+ \gtrsim 80$.

Note that (1.19), (1.20) and (1.21) are equivalent expressions, where the effect of the roughness is measured by a different parameter. They can be related to obtain

$$\Delta U^+(k^+;S^k) = A - B(k^+;S^k) - \frac{1}{\kappa}\log(k^+) = A - 8.5 + \frac{1}{\kappa}\log(k_s^+). \qquad (1.22)$$

For the fully rough regime, B is constant, and therefore we have that $\Delta U^+ \propto \log(k^+)$. Equation (1.22) shows that k_s is only a convenient way of characterizing the drag increment due to the roughness, and may not have any special significance in the dynamics of the flow.

Finally, it is interesting to note that for the usual values of A, $k_s^+ \lesssim 4$ leads to negative values of ΔU^+, indicating that moderately rough surfaces may be able to reduce drag (Tani, 1988; Sirovich & Karlsson, 1997; Bechert *et al.*, 2000). However, in most of the cases, this limit only indicates the *hydraulically smooth regime*, in which the effect of the roughness is negligible and the surface can be considered smooth.

Finally, in the same way as the mean velocity profile in the logarithmic and outer regions of turbulent flows over rough and smooth walls are essentially the same, the classical theory predicts that the kinematics and dynamics of these regions should be very similar. Earlier spectral measurements by Perry & Abell (1977) supported these ideas, as well as the measurements performed later by Perry *et al.* (1986), Ligrani & Moffat (1986) and Perry *et al.* (1987).

k-type and d-type roughness

It is important to clarify that the behavior described above corresponds to the k-type roughness, according to the nomenclature of Perry *et al.* (1969). These authors found that when the roughness consists on narrow spanwise cavities, the roughness function ΔU no longer depends on the characteristic size of the roughness k, but on the thickness of the flow h. This type of roughness, which they termed d-type roughness, never reaches the fully rough regime described before. One of the most appealing characteristics of the d-type roughness is that it should generate a flow with a single length scale valid everywhere, and therefore it should be essentially a pure core flow without logarithmic or buffer regions.

However, the existence of this kind of roughness is subject to some uncertainties, and indeed Jiménez (2004) points out that the evidences for d-type behavior are not conclusive. First, in the experiments of Perry *et al.* (1969), the roughness elements were quite large, with a height to boundary layer thickness ratio $k/h \sim 10-20$. Also, the physical mechanism by which the flow thickness becomes the only length scale is not clear. It has been argued that the flow in the groves is isolated from the rest of the flow, with strong spanwise vortices anchored in the groves. Those vortices break when an intense event coming from the outer region reaches the wall, resulting in intense bursts. Note that while this mechanism explains why the roughness elements length scale does not enter in the roughness function, it does not explain why the flow thickness does.

1.3. Techniques employed in the study of wall-turbulence

Due to the complexity of the mathematical analysis of the Navier-Stokes equations, the advances in the understanding of the turbulent motion strongly rely on empirical data. Nowadays, two different sources of empirical data are used; experiments and numerical simulations. In both cases, the analysis of the data requires the use of statistical tools, and most of the classical text books on turbulence have a chapter devoted to them, as in Batchelor (1953), Tennekes & Lumley (1972), Townsend (1976) or Frisch (1995). Common statistical tools used in the study of turbulence include probability density functions, correlation functions and power density spectra. More specific tools are also found in the literature, like the proper orthogonal decomposition or POD (Bakewell & Lumley, 1967), the quadrant analysis (Wallace *et al.*, 1972; Willmarth & Lu, 1972) or the linear stochastic estimation or LSE (Adrian & Moin, 1988).

Experimental techniques broadly used nowadays include hot wire anemometry, Laser Doppler Anemometry (LDA) and Particle Image Velocimetry (PIV). While the first two only provide the velocity components at a single point, modern implementations of PIV are able to measure three velocity components on a plane or even the three velocity components in a certain volume. The most important advantage of the experiments is their ability to reach higher Reynolds numbers, which also turns out to be their biggest handicap: as the Reynolds number grows, the Kolmogorov scale becomes smaller, and designing experiments able to capture all the scales of the flow is not a trivial task. Experimental techniques will not be used in the present thesis, but comparison with experiments will be presented when possible.

Numerical simulations are also a valuable tool in the analysis of turbulence. They not only provide a complete access to the fluid variables and their derivatives in the whole computational domain, but they also allow the simulation of non-physical configurations: we can filter regions of the flow, damp a certain range of scales, eliminate terms in the Navier-Stokes equations or modify the boundary conditions. These non-physical simulations can be used to investigate the dynamics of a certain region of the flow (Jiménez & Moin, 1991; Jiménez & Pinelli, 1999), test causality relationship between flow structures (Jiménez *et al.*, 2004) or simplify the simulation of complex geometries, such as porous walls Jiménez *et al.* (2001*b*) or riblets Jiménez (1994).

A brief survey presenting the most common approaches to the numerical simulation of turbulent flows follows.

Direct Numerical Simulation

There are in principle three different approaches to the problem of the numerical integration of the Navier-Stokes equations, depending on the level of detail of the

results. The most expensive option (in terms of computational cost) is to integrate directly the full Navier-Stokes equations, resolving all the scales from the integral scale to the dissipative range. This approach is known as Direct Numerical Simulation (DNS). A recent review of the role of DNS as a research tool can be found in Moin & Mahesh (1998), which also include some interesting examples of what they term *novel* DNSes (configurations of turbulent flows that can not be studied with experiments), synergies between experiments and simulations and a review of the contribution of DNS to the understanding of the structure of the turbulent boundary layer.

The spatial resolution (Δ_x) of a DNS is of the order of the Kolmogorov scale,

$$\frac{\Delta_x}{L_\epsilon} \sim \frac{\eta_k}{L_\epsilon} = \left(\frac{u_L L_\epsilon}{\nu}\right)^{-3/4} = Re_L^{-3/4}. \tag{1.23}$$

For historical reasons, (1.23) is usually expressed in terms of the *microscale* Reynolds number, which is defined as

$$Re_\lambda = (15 Re_L)^{1/2}, \tag{1.24}$$

so that $\Delta_x/L_\epsilon \sim Re_\lambda^{-3/2}$. Typical values of the microscale Reynolds number vary from 10 to 10^3. At $Re_\lambda \approx 30$ we can begin to speak about turbulence, and fully turbulent flows require $Re_\lambda \gtrsim 100$. The wake of a walking person has $Re_\lambda \approx 500$, typical industrial flows are in the range $Re_\lambda \approx 100 - 1000$, and the turbulence in the boundary layer of a commercial airplane has $Re_\lambda \approx 300$. Finally, the highest Reynolds numbers measured in the atmosphere are around $Re_\lambda \sim 10^4$.

We can see from these figures how expensive DNSes are. The number of grid points required to resolve a cube of size $O(L_\epsilon^3)$ increases as $Re_\lambda^{9/2}$. Taking into account that the total time needed to have enough statistics is of the order of a few turnover times of the larger structures, $O(L_\epsilon/u_L)$, and that the time step of the simulation is of the order of Δ_x/u_L, we have that the number of time steps is proportional to $Re_\lambda^{3/2}$. Overall, the number of operations required by a DNS is proportional to Re_λ^3, resulting in $O(10^{12})$ operations even for the moderate Reynolds number of $Re_\lambda \approx 100$.

The first DNSes of wall-bounded turbulence were performed in the 1980's by Kim *et al.* (1987) and Spalart (1988). Those simulations had $O(10^6)$ points and low Reynolds numbers. The increase in the computational power of modern supercomputers have made possible DNSes with $O(10^{10})$ points and Reynolds numbers comparable to experiments, like the recent simulations by Kaneda & Ishihara (2006) and Hoyas & Jiménez (2006).

Reynolds Averaged Navier-Stokes equations.

The most convenient option in terms of computational cost is to solve the Reynolds Averaged Navier-Stokes equations (Reynolds, 1894), also known as RANS equations. However, the Reynolds stresses in those equations are unknown and some model is needed to *close* the problem. It is possible to write evolution equations for

these terms, but the new equations then include triple products, which again need to be modeled. The simplest models are based on the concept of *eddy viscosity* (Boussinesq, 1877), which evolved into the *mixing length* concept developed in 1920's by Taylor, Prandtl and von Kármán. More elaborated models are also available, like the popular $k - \varepsilon$ model.

The resolution requirements for RANS computations are minimal, since the grid only needs to be adjusted to the geometry of the flow. Also, since the fluctuating velocity components are included in the model, in most of the cases solving the RANS equations consists only on computing a steady solution.

RANS methods are seldom used in research applications because they require a previous knowledge about the flow in order to adjust the parameters of the model. However, they are a valuable tool in industrial applications, where the critical issue is to obtain a good approximation to the mean flow in times of the order of minutes.

More details about RANS models can be found in several books, like Launder & Spalding (1992), Wilcox (1993) or Pope (2000).

Large Eddy Simulation

Between DNS and RANS we find Large Eddy Simulations (LES), where the dissipative range of scales is modeled making use of the universality of the smallest, isotropic scales (Kolmogorov, 1941).

The formal derivation LES models is based on the application of a smoothing kernel to the Navier-Stokes equations. The shear stresses are then expressed as the sum of two components, the shear stresses of the filtered velocities and the *subgrid* shear stresses, which have to be modeled. One of the most extended models is the Smagorinski model (1963). It is essentially an extension of the eddy viscosity idea of RANS: the subgrid shear stresses are assumed to be proportional and parallel to the filtered rate-of-strain tensor. Recent surveys about LES, filters and models can be found in Sagaut (2005).

The computational cost of an LES is independent of the Reynolds number, since the smallest scale that has to be resolved is a fraction of the integral scale. This is true for flows without walls, or when the flow is separated. In those cases the performance of LES is quite good.

However, wall-bounded turbulence is less suited to LES than free turbulence. The presence of walls increases the anisotropy, worsening the ability of the models to represent the dynamics of the small scales. Also, in the near-wall region the energy containing scales and the dissipative scales coincide, irrespectively of the Reynolds number of the flow. In this situation, the performance of LES decreases, and the use of special wall models is required. Another option is to cluster grid points in the vicinity of the wall to resolve the wall-normal direction as in DNS. The disadvantage is that the cost of the simulation increases as $Re_\lambda^{3/2}$ instead of being independent of the Reynolds number.

1.4. Aims

As described in §1.2, the classical theory for the structure of turbulence in the logarithmic and outer regions is based on the hypothesis that far enough from the wall, the turbulent motion at sufficiently high Reynolds number is independent of the roughness and of the viscosity, except for their effect in setting the velocity scale u_τ, the additive constant in (1.15) and the boundary layer thickness. This implies that, apart from the effect of the wall-roughness on the mean velocity, no other differences between smooth- and rough-walled flows should be observed. These ideas were supported by early experiments by Perry & Abell (1977) and by Ligrani & Moffat (1986).

However, this theory has been challenged during the last decade, and is still a subject of discussion (see the review by Jiménez, 2004). Krogstad *et al.* (1992) and Krogstad & Antonia (1994, 1999) found important departures from the smooth-wall behavior in the outer region of a boundary layer for two different rough walls. Similar results were published by Leonardi *et al.* (2003), Bhaganagar & Kim (2003) and Orlandi *et al.* (2003) in non-symmetric channels with roughness elements only in one wall.

Another challenge to the classical theory comes from conceptual and predictive models based on coherent structures (see the review by Robinson, 1991*a*). Theoretical models based on Townsend's (1976) attached-eddy concept incorporate inner-outer interactions by considering hierarchies of vortex loops that are seeded in the near-wall region and grow by sequences of mergers, as proposed by Head & Bandyopadhyay (1981) and Perry & Chong (1982). These ideas have been broadly supported by subsequent laboratory experiments and low-Reynolds-number numerical simulations (Robinson, 1991*b*; Blackburn *et al.*, 1996; Chong *et al.*, 1998; Adrian *et al.*, 2000; Christensen & Adrian, 2001; Ganapathisubramani *et al.*, 2003; Tomkins & Adrian, 2003; Tanahashi *et al.*, 2004). These theoretical models imply that it should be possible to modify the structure of the whole outer region by changing the characteristics of the hairpins near the wall.

The present thesis aims to shed some light on these issues. DNSes of a turbulent channel flow with a moderate Reynolds number are performed, where the standard non-slip and impermeability boundary conditions are replaced by prescribed velocity disturbances, that mimic the effect of wall-roughness. The results from these simulations will contribute to the understanding of the role of the inner region in the dynamics of the outer region by clarifying the nature of the inner-outer interactions in turbulent channels.

Another objective that is attempted in the present thesis is the development a simple model capable of explaining these interactions. Very recent results (del Álamo *et al.*, 2006; del Álamo & Jiménez, 2006) suggest that at least in a statistical sense the dynamics of the logarithmic layer are linear, a possibility that is explored in detail in the last chapter.

1.5. Contents

The present thesis is structured in three chapters. The first chapter is devoted to the description and characterization of the three DNS of turbulent channels with wall-boundary disturbances that have been developed and run during the first two years of the PhD. This chapter also contains a discussion of the results, a comparison with DNS data of a turbulent channel with smooth walls at a comparable Reynolds number and with experiments on rough-walled pipes and channels. The contents of this chapter have been published in the *Journal of Fluid Mechanics*, under the title "Effect of wall-boundary disturbances on turbulent channel flows", volume 566, pages 357-376, with J. Jiménez as coauthor.

In the second chapter, the coherent structures over the disturbed walls are compared with those found over smooth walls, using the techniques developed by del Álamo *et al.* (2006). Part of the contents of this chapter have been published in the *Journal of Fluid Mechanics*, under the title "Vorticity organization in the outer layer of turbulent channels with disturbed walls", volume 591, pages 145-154, with J. Jiménez and J. C. del Álamo as coauthors.

Finally, the third chapter proposes a description of the dynamics of the logarithmic and outer layers in terms of a linear model, based on the results presented in the previous chapters and on the numerical solution of the linearized Navier-Stokes equations with a turbulent eddy viscosity.

Chapter 2

DNS of turbulent channel with wall disturbances [1]

2.1. Introduction

As has been described in the introduction, the classical theory for wall-bounded turbulent flows can be condensed into the Townsend's hypothesis. It essentially states that the flow in the logarithmic and outer regions does not depend on the wall details, except for the role of the wall in setting the mean velocity at the beginning of the logarithmic region. Turbulent flows over rough-walls are exceptionally well-suited to analyze this statement, since the roughness elements drastically modify the near-wall region. Therefore, any effect of the wall on the outer region should be clearly observable in a rough-walled flow.

As reported in §1.2, early measurements in rough-walled boundary layers and pipe flows gave support to the Townsend's hypothesis (Perry & Abell, 1977; Perry *et al.*, 1986; Ligrani & Moffat, 1986; Perry *et al.*, 1987). However, as pointed out in the recent review by Jiménez (2004), this theory has been challenged during the past decades. The most important challenge comes from the experiments of Krogstad *et al.* (1992) in a boundary layer over a mesh-screen wall. The comparison with the results obtained in a smooth-walled boundary layer reveals that the wall-normal velocity fluctuations are enhanced across the whole thickness of the flow in the rough case, indicating that the active scales are modified everywhere. In a later paper, Krogstad & Antonia (1994) report that these modifications are associated to changes in the streamwise correlation length of all the velocity components, around twice shorter for the structures over rough walls than for those over smooth walls.

Krogstad & Antonia (1999) extend the results obtained with the mesh-screen, comparing the smooth-walled case with a boundary layer over a wall roughened with circular rods. This new rough surface also produces modifications in the velocity fluctuations in the outer region, which are accompanied by differences in the Q2 and Q4 quadrant contributions to the Reynolds stresses, with increased sweep events in

[1] Part of the contents of this chapter have been published in the Journal of Fluid Mechanics, volume 566, pages 357-376, with Javier Jiménez as coauthor.

the rough-walled cases. The comparison of the spectra from the rough-walled cases with the smooth-walled ones shows differences for the v-spectrum and for the uv-cospectrum, while the u-spectrum compares well.

Similar results are published by Djenidi *et al.* (1994) over a d-type roughness in a boundary layer. They conclude that the effects of the surface condition are not confined to the inner region of the flow. The experiments of Poggi *et al.* (2003) in turbulent channels indicate that the roughness decreases the levels of anisotropy and intermittency in the inner region. They suggest that the changes in the inner region modify the flow in such a way that the effects of the roughness should also be present in the core region. Simulations in non-symmetric channels, with roughness elements only in one wall, also show important departures from the smooth wall behavior that extends up to the center of the channel (Bhaganagar & Kim, 2003; Leonardi *et al.*, 2003; Orlandi *et al.*, 2003), although it is unclear whether this is caused by the roughness or by the asymmetry of the mean profile.

On the other hand, other experiments over rough-walled boundary layers show excellent agreement with smooth-walled data in the outer region. Keirsbulck *et al.* (2002) show velocity fluctuations profiles collapsing with smooth-walled data in the outer region, although the wall-normal velocity is affected by the roughness up to 40% of the boundary layer thickness. The turbulent production and dissipation profiles are quite similar all across the layer, while the wall-normal energy flux is very different between the rough and the smooth cases. Flack *et al.* (2005) report Reynolds stresses, quadrant analysis and velocity triple products collapsing with the smooth-walled data within the experimental uncertainty, for rough-walled flows with $\delta \gg k_s$.

A recent study in turbulent channels by Bakken *et al.* (2005), using their own experimental data and the DNS results of Ashafarian *et al.* (2004), supports the idea that the wall-roughness modifies the velocity fluctuations profiles only within the roughness sublayer, although some uncertainty exists about further effects within the outer region. The authors speculate that turbulent channels over rough walls satisfy the similarity hypothesis of Townsend but that the same may not be true for boundary layers.

The numerical experiments presented in this chapter aim to clarify how the outer turbulent flow is modified by the near-wall region. To that end, we present a set of DNSes of turbulent channels, in which the impermeability and non-slip boundary conditions are substituted by prescribed velocity perturbations. These simulations can be understood from two different points of view. First, the perturbations at the wall drastically alter the near-wall region (see §2.3), precluding the development of the near-wall energy cycle characteristic of smooth walls. Since this is expected to happen in rough-walled turbulent flows, the present DNSes can be understood as turbulent channels with artificial roughness. On the other hand, we have already mentioned in §1.3 that the simulation of turbulence offers the possibility of studying non-physical flow configurations. In particular, the above mentioned near-wall cycle was described by Jiménez & Pinelli (1999) using an autonomous channel in which the

outer region was removed by an explicit filtering. From this second perspective, the present DNSes can be understood as a study of a core region without the structures of the smooth wall, complementary to the autonomous channel.

The present chapter is organized as follows. The numerical setup and the boundary conditions are presented in §2.2. The effect of this artificial roughness on the rest of the flow is discussed in §2.3 using one-point statistics. The flow around the disturbances is characterized in §2.4, and the spectral analysis of the outer flow is conducted in §2.5, emphasizing the effect of the wall disturbances on the largest scales of the outer region. Conclusions are offered in §2.6.

2.2. Numerical Experiments

The present direct numerical simulation integrates the Navier Stokes equations in the form of two evolution equations for the wall-normal vorticity ω_y and for the Laplacian of the wall-normal velocity $\nabla^2 v$. The time integration is performed using a third-order Runge-Kutta with implicit viscous terms, as in Kim *et al.* (1987). The spatial discretization is pseudo spectral, with dealiased Fourier expansions for the streamwise (x) and spanwise (z) directions, and a compact finite differences scheme in the wall-normal direction (y). The periodicities of the computational box in the wall-parallel directions are L_x and L_z, while h is the half height of the channel. The mean velocities in the streamwise and spanwise directions are U and W, while the corresponding velocity fluctuations are u and w. The mean value of the wall-normal velocity is zero.

The numerical scheme for the first derivative in the y-direction is 4th-order spectral-like compact finite differences scheme (Lele, 1992), based on a five-point stencil on a uniform mesh, which is analytically mapped to the actual stretched mesh of the simulation. The coefficients of the scheme are computed using two consistency conditions, and two extra conditions provided by the minimization of the L_2 norm of the difference between the eigenvalues $i\alpha$ and $i\tilde{\alpha}$ of the exact and discretized derivatives, in the range $0 < \alpha\Delta x < \pi$. The resulting scheme has quite good resolution properties; the standard five-point 8th-order compact finite differences scheme resolves up to 61% of the numerical wavenumbers with less than 1% of error, while the modified scheme resolves up to 74% with the same accuracy.

For the two points closest to the wall we use compact finite differences schemes with three-point stencils. A 3rd-order scheme with a non-centered stencil is used in the point at the wall, and the next one uses a standard 4th-order centered scheme. It was found that improving the order of the scheme at the wall above the order of the scheme at the center of the channel led to numerical instabilities, in agreement with the results of Kwok *et al.* (2001). These authors also show that boundary schemes one order lower than the interior scheme are adequate to ensure global convergence consistent with the order of the interior scheme.

For reasons of numerical efficiency, the scheme for the second derivative, required to solve the Helmholtz equation for the viscous terms, is directly computed in the

stretched mesh, and only the consistency conditions are used to compute the coefficients of the scheme. As for the first derivative, a five-point stencil is used, with non-centered stencils at the walls. The resulting scheme has 6th-order accuracy.

The non-slip and impermeability boundary conditions for the velocity at the walls are replaced by prescribed zero-mean-value perturbation velocities. These velocities are characterized by the amplitudes and by the streamwise and spanwise wavelengths (Λ_x and Λ_z) of the single Fourier mode being forced. When only the wall-normal velocity component is disturbed, a fairly small effect on the flow is achieved. The roughness function corresponding to a wall-normal velocity disturbance of $v_w'^+ = \overline{(v_w^2)}^+ = 0.72$ is $\Delta U^+ = 4.6$, where the prime denotes the root mean square, the subindex w denotes variables evaluated at the wall, $y = 0$, and the overline denotes averaging in time and in the wall-parallel directions. When the streamwise and the wall-normal velocities are forced coherently so that the Reynolds stresses component $\overline{(uv)}_w \neq 0$, a much stronger effect on the flow is obtained. For instance, $u_w'^+ = -v_w'^+ = 0.83$ leads to $\Delta U^+ = 8.7$. Hence, three distinct forcings have been used, all having $\overline{(uv)}_w \neq 0$ and $\overline{(uw)}_w = \overline{(vw)}_w = 0$. The first two have $u'_w \neq 0$, $v'_w \neq 0$, $w'_w = 0$ and will generally be represented in the figures with open symbols. The third forcing has $u'_w = v'_w = w'_w \neq 0$, and will be represented with solid symbols. In this case, w_w is shifted in x by $\Lambda_x/2$ with respect to u_w and v_w, so that $\overline{(uw)}_w = \overline{(vw)}_w = 0$. As a consequence, the imposed velocity disturbances are non-symmetric and the flow just upstream of $v_w > 0$ goes left, while the flow downstream goes right.

These boundary conditions are quite different from those proposed by Orlandi *et al.* (2003), where an instantaneous velocity plane extracted from a full DNS simulation was used as boundary condition at one wall of the perturbed DNS. The advantages of the present approach are essentially a more complete control of the boundary condition and an easier parameterization of the artificial roughness. Both walls are forced in our case to obtain a symmetric configuration with a well-defined center, where the turbulent structures can be compared to those extracted from smooth-walled channels.

2.3. One-point statistics

The parameters of our numerical experiments are presented in table 2.1. Two different box sizes are used, upper case letters denote big boxes, $L_x \times L_z = 8\pi h \times 4\pi h$, and lower case letters denote smaller ones, $L_x \times L_z = 4\pi h \times 2\pi h$. The cheaper small-box cases are performed to investigate the effects that different intensities and wavelengths of the forcing impose on the $O(y)$ active scales of the outer flow. It is shown by del Álamo *et al.* (2004) that DNSes with these box lengths are able to accurately represent most of the active scales of the turbulence, but do not contain the very large scales of the flow. Therefore, a large-box simulation **R2** is used to study the effects of the mid-intensity forcing on these scales. The results from these four wall-disturbed simulations are compared to a DNS of a smooth-walled turbulent channel in a large box performed by del Álamo & Jiménez (2003), which

	Re_τ	L_x/h	Δx^+	Δy_c^+	Δy_w^+	$u_w'^+$	$v_w'^+$	$(\omega_x')_w^+$	Λ_x^+	ΔU^+	δ_y^+	k_s^+	k^+	h/k	Λ_x/k
r1	556	4π	10.2	7.0	0.8	0.94	1.13	1.19	71	7.1	-2.6	67	6.9	81	10.3
r2	631	4π	11.6	8.0	0.9	0.83	0.83	1.12	220	8.7	-11.2	128	15.5	41	14.2
r3	674	4π	12.4	8.6	1.0	0.67	0.67	1.03	529	9.6	-20.7	207	24.4	28	21.7
R2	632	8π	11.6	8.0	0.9	0.83	0.83	1.12	221	8.7	-11.7	129	15.5	41	14.2
S0	547	8π	13.4	6.7	$\ll 1$	0	0	0.26							

Table 2.1: Numerical simulation parameters. $Re_\tau = u_\tau h/\nu$ is the friction Reynolds number. L_x and $L_z = L_x/2$ are the streamwise and spanwise lengths of the computational box. The mesh resolution after dealiasing is Δx, $\Delta z = \Delta x/2$. The wall-normal mesh resolution is Δy_c at the center of the channel and Δy_w at the wall. u_w' and v_w' are the wall forcing intensities, $(\omega_x)_w'$ is the streamwise vorticity intensity at the wall, Λ_x and $\Lambda_z = \Lambda_x/2$ are the streamwise and spanwise wavelengths of the forcing. ΔU and δ_y are the roughness function and the wall-normal shift, obtained from a logarithmic law adjustment. k_s is the equivalent sand roughness and k is a characteristic length of the forcing, defined in §2.4.

is also included in table 2.1 as case **S0**. This numerical experiment has a friction Reynolds number similar to that of the forced cases.

The definition of the origin of the wall-normal coordinate in rough-walled flows requires some care, due to the nature of the rough wall. Several methods have been proposed. Thom (1971) and Jackson (1981) show that a reasonable choice is the mean momentum absorption plane, obtained as the centroid of the drag profile on the roughness. Other methods are based in the adjustment of the mean velocity profile to a logarithmic law (see the review by Raupach *et al.*, 1991).

In the present simulations the method proposed by Thom (1971) and Jackson (1981) to estimate the position of the wall is not applicable, and both the wall-normal shift δ_y^+ and the roughness function ΔU^+ are obtained by a least square fit of the mean velocity profile to the logarithmic law (1.19) in the region between $y^+ = 50$ and $y = 0.2h$. The exact value of the Kármán constant used for the fitting produces variations in ΔU^+, which are of about 15% when κ is varied in the range $0.38 - 0.42$. The position of the wall also varies with κ, but in all cases $\delta_y^+ \approx O(10)$. The values presented in table 2.1 are obtained for $\kappa = 0.41$ and $A = 5.2$. The equivalent sand roughness k_s^+ of the disturbed cases corresponds to the fully rough regime, except for **r1** which may be classified as transitional. All the computed δ_y^+ are small compared with k_s^+ and with Re_τ. A new wall-normal coordinate

$$\tilde{y} = y + \delta_y\,(1 - y/h) \tag{2.1}$$

is defined to expand the numerical wall-normal coordinate y from the interval $[0, 2h]$ to $[\delta_y, 2h - \delta_y]$. It is interesting to note that δ_y is negative for all cases, which means that the effective wall ($\tilde{y} = 0$) is above the plane at which the disturbances are introduced ($y = 0$). In the smooth case **S0** we have $\tilde{y} = y$.

The mean streamwise velocity profiles are presented in figure 2.1(a) expressed in

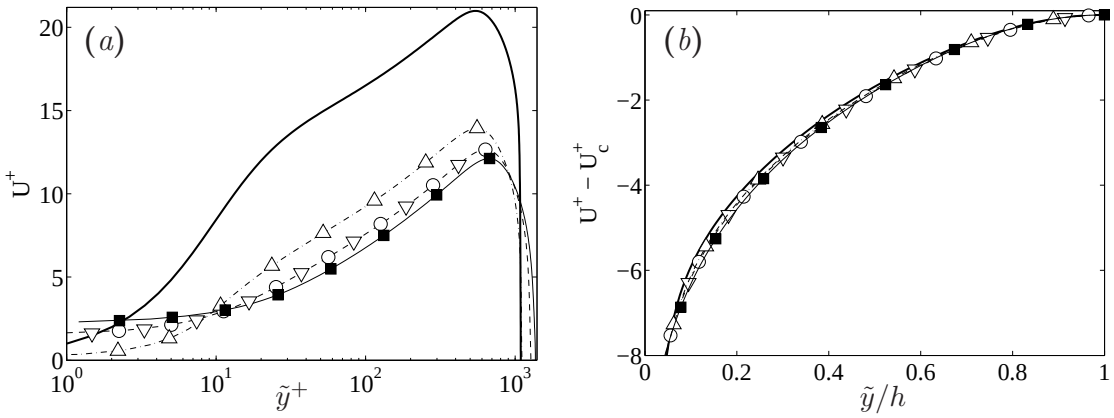

Figure 2.1: (a) Mean streamwise velocity. (b) Streamwise velocity defect law, $U_c = U(y = h)$. ——, **S0**; △, **r1**; ▽, **r2**; ○, **R2**; ■, **r3**.

wall units, and in velocity defect form in figure 2.1(b). Both figures are consistent with previous results obtained over rough walls in experiments (Bakken *et al.*, 2005; Poggi *et al.*, 2003) and in numerical simulations (Ashafarian *et al.*, 2004; Leonardi *et al.*, 2003; Orlandi *et al.*, 2003). Only small deviations from the smooth-walled velocity defect law are observed in figure 2.1(b). Similar differences were observed by del Álamo *et al.* (2004) when comparing smooth channels with different box sizes. They suggested that their discrepancies could be related to contributions from large scales to the mean flow, an argument that may also be valid for the present results.

Although not obvious from the figure, $\partial U/\partial y$ at the wall in case **r1** is roughly zero, which indicates that the mean flow above the disturbances is separated, with $\partial U^+/\partial y^+|_w = -0.07$ and $\min(U^+) = -0.01$. This is due to the high value of v_w employed in this case. Similar locally separated flows are found by Jiménez *et al.* (2001b) in porous channels when the porosity coefficient exceeded a certain threshold.

For the case **r3** a secondary flow (not shown) is observed in the spanwise direction, with $W(y) < 0.1U(y)$ everywhere, a maximum value of $|W^+| = 0.3$ at $y^+ = 40$, and zero mass flux when integrated across the full height of the channel.

The u' profile in the wall region is presented in figure 2.2(a). The intensity of the near-wall peak decreases as the roughness function increases, and the same is true for the off-wall peak of the streamwise vorticity intensity ω_x' in figure 2.2(b). In both cases, the attenuation of the peak is due to the shortening of the spectra, which will be discussed in §2.5. The maximum value of $\omega_x'^+$ is always at $y = 0$. In the smooth case this is due to the interaction of the wall with the transverse velocities created by the quasi-streamwise vortices (Kim *et al.*, 1987). In the disturbed cases, that component is probably also present, but a much larger contribution comes from the forcing itself (compare the values of $\omega_x'|_w$ given in table 2.1). The off-wall peaks of u' and ω_x' are indicators for the near-wall streaks and for the quasi-streamwise

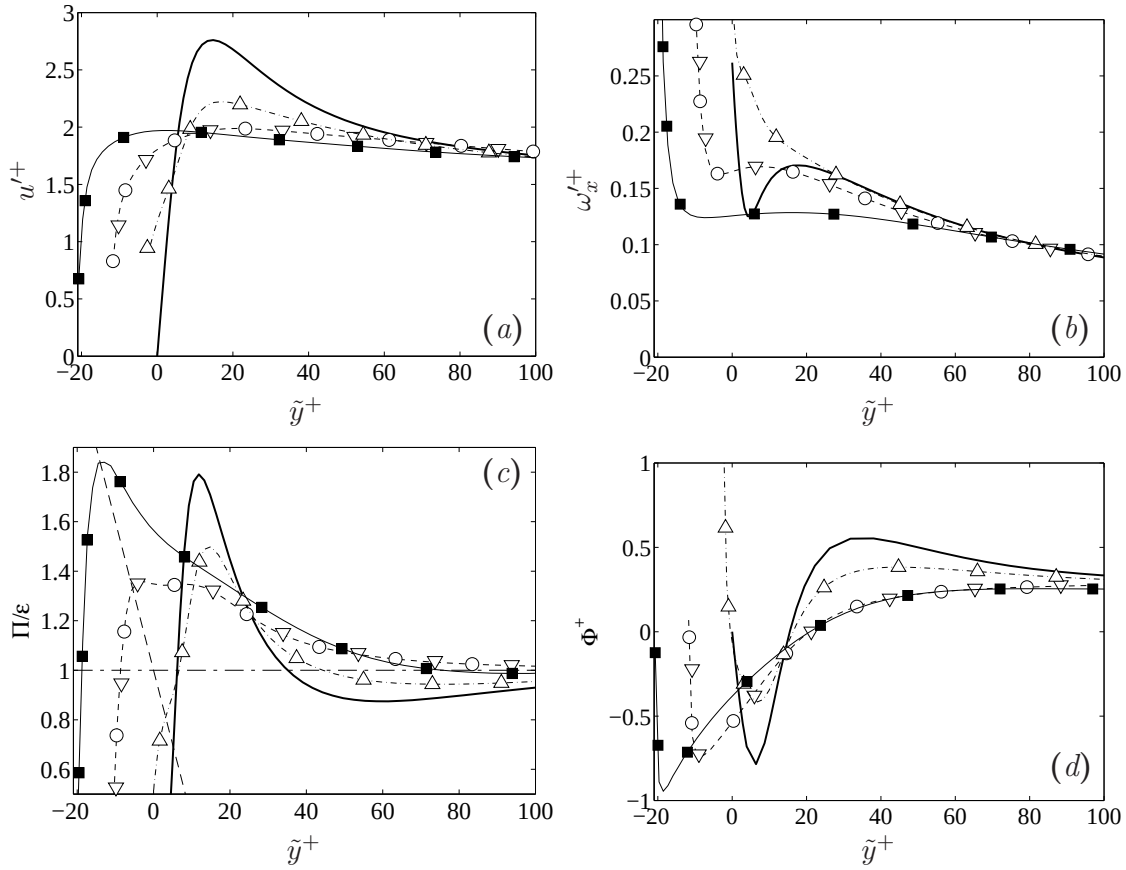

Figure 2.2: Near-wall behavior. (a) Intensities of the streamwise velocity fluctuations and, (b) of the streamwise vorticity. (c) Ratio of turbulent energy production to dissipation. (d) Turbulent energy flux, defined in (2.2). ——, **S0**; △, **r1**; ▽, **r2**; ○, **R2**; ■, **r3**.

vortices. In smooth channels those structures are involved in the self sustaining near-wall energy cycle described by Jiménez & Pinelli (1999), which is responsible at the present Re_τ for roughly 35% of the total energy production in the channel. The damping of those peaks in figures 2.2(a) and 2.2(b) suggests that the cycle is perturbed in case **r1**, strongly perturbed in **r2** and **R2**, and effectively destroyed in **r3**.

These changes are also reflected in the ratio of the turbulent energy production (Π) to dissipation (ε), shown in figure 2.2(c). In the smooth-walled case there is a production peak at $\tilde{y}^+ \sim 20$, and a slightly dissipative layer in $40 < \tilde{y}^+ < 100$. As the roughness function increases, this peak decreases and the dissipative region disappears. There is a new peak of Π/ε just above the wall which is due to the additional Reynolds stress introduced by the forcing, and which has been highlighted in the figure with a dashed line. In the case **R2** both peaks form the two ends of a plateau, but for **r3** the new peak dominates and the old one has

essentially disappeared. In all cases the dissipation at the wall is much larger than the production, and the wall acts a net energy sink.

Figure 2.2(d) presents the energy flux Φ, computed by evaluating each term in

$$\Phi = \frac{1}{2}\overline{(u_i^2 v)} + \overline{(vp)} - \frac{\nu}{2}\frac{\partial^2}{\partial y^2}\overline{(u_i^2)}, \tag{2.2}$$

where the subindex implies a summation for all the velocity components, and p is the pressure fluctuation. In smooth-walled flows, part of the energy produced around $\tilde{y}^+ \sim 20$ is exported towards the center of the channel ($\Phi > 0$), to be dissipated by the background turbulence, while the rest is exported towards the wall ($\Phi < 0$), where viscosity takes care of it. The maximum of Φ near $\tilde{y}^+ = 40$ is compensated by the extra dissipation shown in figure 2.2(c) at that level. On the disturbed cases, the energy also flows both towards the center and towards the wall, but the maximum at $\tilde{y}^+ = 40$ progressively disappears, together with the dissipative layer.

The energy structure in the near-wall layer looks different in the smooth and in the disturbed cases, and it is clear that in the latter the canonical cycle of the smooth-walled channel has been severely perturbed. It is therefore significant that far from the wall all the variables tend to their smooth values. The comparison is extended to the whole channel in figure 2.3. Except near the wall, all the cases agree.

Specially significant is the energy flux. There is in all cases a region where $\Pi/\varepsilon \approx 1$, which suggests the formation of an equilibrium overlap layer. That is a local property of the turbulence at that wall distance, consistent with the usual arguments for a logarithmic law. Those arguments only require that Φ should be constant across that region, but they say nothing about its actual value. In order to investigate whether this value is fixed by the wall, by the outer region or by the log layer itself, we can compare Φ for flows with comparable Reynolds numbers but different wall regions (smooth and rough walls) or different outer regions (channels and boundary layers). As Φ is not always available in experiments, we will also use $\overline{(u^2 v)}$, which accounts for roughly one half of Φ in (2.2). The collapse shown in figure 2.3(d) and the results reported by Bakken *et al.* (2005) in channels and Flack *et al.* (2005) in boundary layers suggest that the energy flux in the overlap region is not imposed by the wall. On the other hand, Jiménez & Simens (2000) report that $\overline{(u^2 v)}^+$ collapses in the overlap region for turbulent channels and for boundary layers. This evidence suggests that the level $\Phi^+ \approx 0.3$ should be intrinsic to the log layer, instead of dependent on its boundary conditions.

It is also interesting in figure 2.3(b) that the transverse intensities v' and w' increase near the wall as the roughness increases, even as ω_x' decreases. Examination of their spectra shows that the extra energy is approximately isotropic in the wall-parallel plane, and therefore unrelated to the usual vortices found over smooth walls.

The collapse of the velocity fluctuation intensities, of the ratio of production to dissipation, and of the energy flux in the outer region agrees with most of the literature comparing flows over smooth and rough walls, as already mentioned in

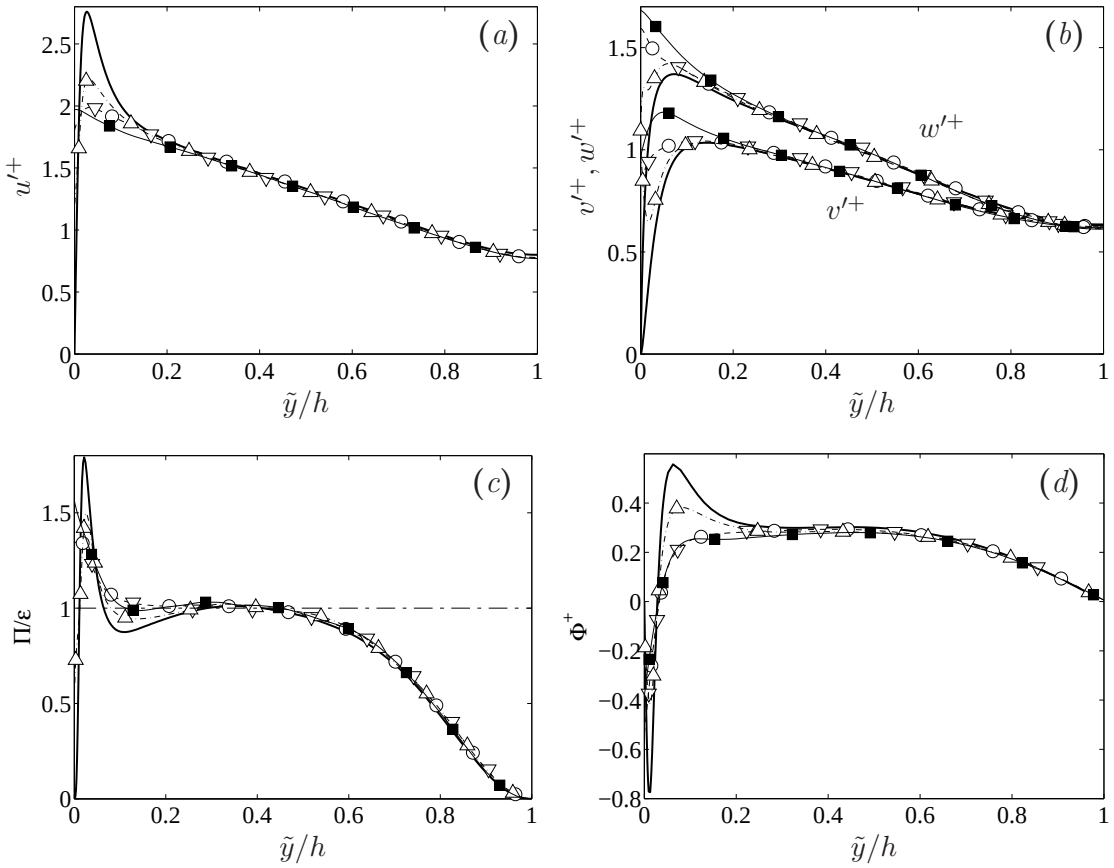

Figure 2.3: Turbulent statistics in the outer region. (*a*) Intensity of the streamwise velocity fluctuations and, (*b*) of the wall-normal and spanwise velocity fluctuations. (*c*) Ratio of turbulent energy production to dissipation. (*d*) Turbulent energy flux, defined in (2.2). ——, **S0**; △, **r1**; ▽, **r2**; ○, **R2**; ■, **r3**.

the introduction. It however disagrees with Krogstad *et al.* (1992), where the high growth rate of the boundary layer thickness may introduce distortions in the wall-normal mean velocity component. Orlandi *et al.* (2003) also find a different behavior in channels with only one rough wall, but their mean profiles are asymmetric, and the additional shear introduced by the difference in wall friction between the smooth and the rough wall is not negligible at moderate Reynolds numbers. That extra shear may modify the structures in the core region of the channel, as reported in asymmetric channels by Hanjalić & Launder (1972).

As expected, the results from cases **r2** and **R2** are almost indistinguishable in figures 2.2 and 2.3, and only **R2** will be used from now on. The good agreement between the two boxes confirms that the $4\pi h \times 2\pi h$ boxes contain most of the active scales in the turbulent channel flow.

We can also analyze the effect of the wall on the advection velocity of the u structures, which corresponds to that of ω_y in the limit of infinitely elongated struc-

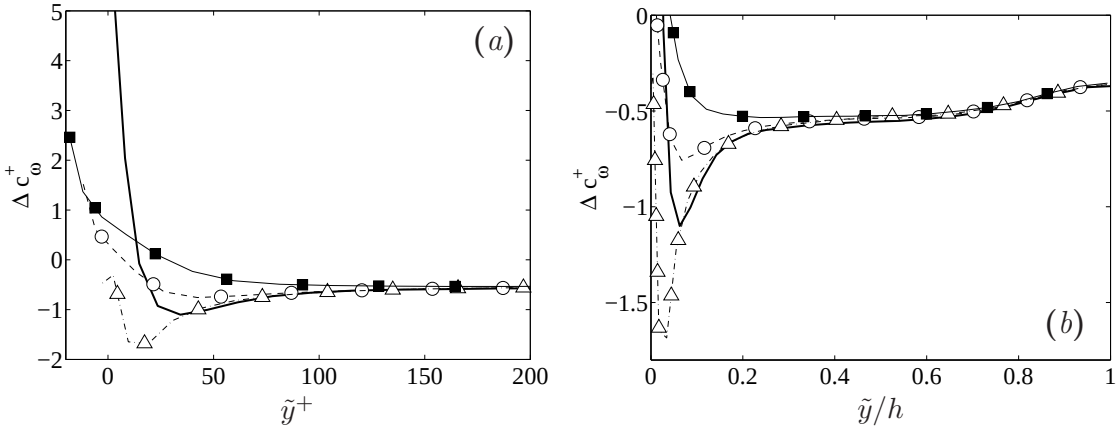

Figure 2.4: Advection velocities in the outer region. Δc_ω^+ computed for all wavenumbers, plotted as a function of the wall distance (a) in wall units and (b) normalized with h. ——, **S0**; △, **r1**; ○, **R2**; ■, **r3**.

tures. The method used here to compute the advection velocity was previously used by Jiménez *et al.* (2004), and is based on the equation verified by a simple wave,

$$\mathrm{Im}(\widehat{\varphi}^* \cdot \partial_t \widehat{\varphi}) = -k_x (\widehat{\varphi}^* \cdot \widehat{\varphi})\, c, \tag{2.3}$$

where c is the phase velocity, $\widehat{\varphi}$ is the corresponding Fourier mode, k_x is the streamwise wavenumber and the asterisk indicates complex conjugation. This equation only works for a single Fourier mode. For larger sets of wavenumbers it can be generalized by averaging the spectral quantities in both sides of (2.3), so that the advection velocity of ω_y is defined as

$$c_\omega = -\frac{\mathrm{Im}\langle \widehat{\omega}_y^* \cdot \partial_t \widehat{\omega}_y \rangle_\Omega}{\langle k_x\, \widehat{\omega}_y^* \cdot \widehat{\omega}_y \rangle_\Omega} = U + \Delta c_\omega, \tag{2.4}$$

where $\langle\rangle_\Omega$ implies that the average is taken over all the wavenumbers in the Fourier domain Ω. Note that the term Δc_ω contains the non-linear advection and viscous contributions, but not the mean velocity U. Therefore, Δc_ω describes the interaction of ω_y with the mean flow, and is a first-order indicator of the dynamics.

The comparison of (2.4) with the more usual definitions of advection velocity given by Willmarth & Woolridge (1962) and Wills (1964) is documented in del Álamo & Jiménez (2008). Anyways, since the same definition is used here for both the rough- and the smooth-walled simulations, the exact relationship of c_ω with the classical definitions of advection velocity is not critical for the purposes of this section.

Figure 2.4 presents the distribution of Δc_ω^+ with respect to the wall distance, computed over the whole wavenumber domain. Figure 2.4(a) shows that near the wall the distribution of Δc_ω^+ is very different in the four cases. The smooth-walled channel has higher Δc_ω^+ at the wall than the disturbed cases, due to its higher

$\partial U/\partial y|_w$, and also because of the negative contribution to Δc_ω^+ of all the structures which are essentially attached to the wall forcing. The negative peak in **S0** around $\tilde{y}^+ \approx 30$ is less prominent in **R2** and **r3**, as a consequence of the interruption of the near wall cycle in the later. In the transitional case **r1** this peak remains roughly unchanged, and the more intense negative peak below it is again due to the structures attached to the wall forcing.

Despite the big differences observed near the wall, the disturbed cases tend to the smooth-walled values when $\tilde{y}^+$ increases, and figure 2.4(b) shows that they compare well for $\tilde{y} > 0.2h$. This suggests that to a first approximation, the dynamics of the outer region are not modified by the wall. This result is consistent with the advection velocities of u computed by Sabot *et al.* (1977) in rough- and smooth-walled pipes, using space-time correlations for the large streamwise separation limit.

2.4. Box-filtered flow fields

In §2.3 we have seen that the present forcing is able to strongly modify the near-wall region of a smooth-walled channel, effectively destroying its self-sustaining cycle. In fact, the flow just above the wall is complex, with locally separated regions ($u < 0$) attached to the areas being blown ($v_w > 0$), and high velocity gradients over the regions under suction ($v_w < 0$). We can observe an example of these instantaneous separation bubbles in figure 2.5(a). Because of the observed inhomogeneity, plane-averaged quantities are not adequate to study the flow features near the wall, while figure 2.5(a) shows that instantaneous realizations are hard to comprehend. Hence, we compute the averaged flow in boxes of size $\Lambda_x \times \Lambda_z/2 \times h$ containing a forcing cell, which consists of a single blow and a single suction, as shown in figure 2.5(b). This box averaging is performed using a Fourier filter that retains only those modes which are conserved by the group of translations in physical space that keeps the forcing invariant, but excluding the uniform $(0,0)$ mode. We denote with the subindex B the variables averaged in this way.

Note that strict time averaging of the velocity fluctuations, without the homogeneity assumption, would lead us to a flow field composed of boxes like the one shown in figure 2.5(b). This is true provided that the forcing does not develop sub-harmonic perturbations before breaking in fully developed turbulence, which is confirmed by the spectral analysis. Therefore, it is possible to derive an equation for $\mathbf{u}_B$, by time averaging the Navier-Stokes equations for the velocity fluctuations. In the resulting equations, and for wall distances $y \sim \Lambda_x$ and $U \gg u_\tau \gtrsim u_B$, the contribution from the mean velocity advection and the pressure gradient are dominant. On the other hand, the advection due to u_B and the Reynolds stresses produced by the remaining velocity fluctuations are negligible. This leads to the linearized Rayleigh equation, whose solution for $y \sim \Lambda_x$ decays as

$$u_B \sim \exp(-\sqrt{K_x^2 + K_z^2}\, y) = \exp(-2\pi\sqrt{5} y/\Lambda_x), \tag{2.5}$$

where $K_x = 2\pi/\Lambda_x$ and $K_z = 2\pi/\Lambda_z$ are the wavenumbers of the forcing. Note that,

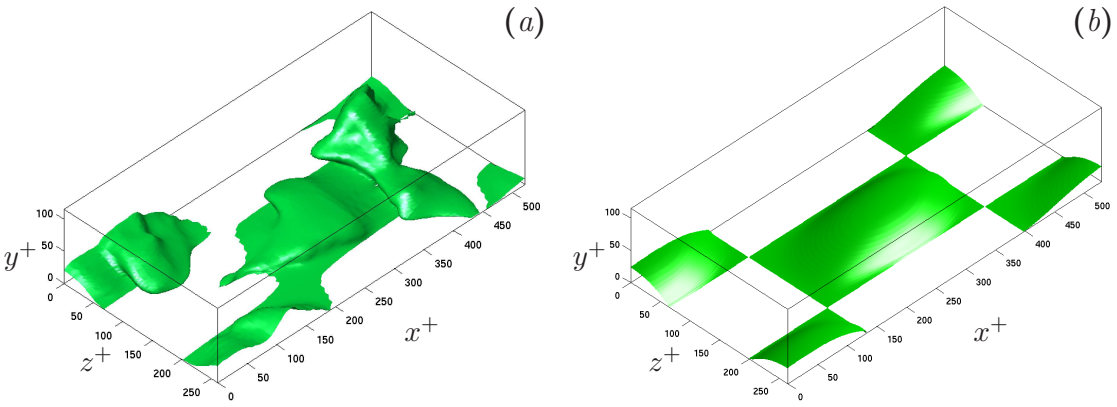

Figure 2.5: (a) Instantaneous and (b) averaged separation bubbles for case **R2**, identified by isosurfaces of $u = 0$.

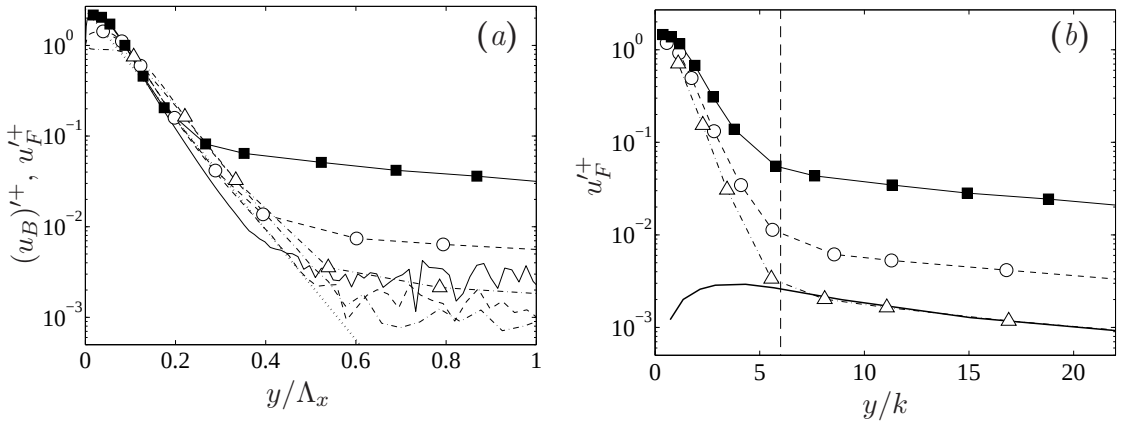

Figure 2.6: Streamwise velocity fluctuations near the wall, $(u_B)'^+$ from box-averaged flow fields (lines), and $u_F'^+$ from filtered spectra (symbols). (a) Wall distances normalized with Λ_x. △, and − − −, **r1**; ○, and ——, **R2**; ■, and −·−·, **r3**. The dotted straight line is (2.5). (b) Wall distances normalized with k, defined in (2.6). △, **r1**; ○, **R2**; ■, **r3**; ——, **S0** using the filter and the value of k calculated for **r1**. The dashed vertical line is $\tilde{y} = 6k$.

as $\Lambda_x = 2\Lambda_z$ in the present simulations, there is no difference in normalizing y with Λ_x or $(K_x^2 + K_z^2)^{-1/2}$ in (2.5), except for a constant factor.

Figure 2.6(a) shows $(u_B)'^+$ as a function of the wall distance normalized with the wavelength Λ_x of the forcing. Near the wall, $(u_B)'^+$ accounts for most of u', but it tends to zero as y increases. The ground level of $(u_B)'^+ \approx 10^{-3}$ for $y > 0.6\Lambda_x$ is consistent with the expected uncertainty due to the limited number of forcing cells used for the statistics, which is $5 \times 10^4 - 5 \times 10^5$ for the 150 available flow snapshots. Nevertheless, the statistics are good enough to observe the predicted exponential decay.

Similar exponential decays are also observed for the other two velocities and for

all the components of the vorticity vector. However, the tangential Reynolds stress $\langle u_B v_B \rangle$ of the rough cases does not collapse either with y^+, with y/Λ_x or with y/h. Hence, we define a new length scale

$$k = -\int_0^h \overline{(u_B v_B)}^+ \, dy, \tag{2.6}$$

that corresponds to the height at which the full tangential Reynolds stress u_τ^2 would exert the same moment as the actual $\overline{(u_B v_B)}$ distribution. This definition is similar to the method proposed by Thom (1971) and Jackson (1981) to calculate the origin for y, defined as the position in which a uniform stress would exert the same moment on the flow as the real rough wall. It is interesting that in the present cases k is roughly equal to the maximum height of the separated flow regions of the box-averaged fields ($u_B < 0$), located above the areas being blown. The wavelength Λ_x and k are not proportional, as can be observed in the last column of table 2.1. In fact, k not only depends on Λ_x, but also on the other parameters of the forcing and on the Reynolds number of the flow. However, if we assume that (2.5) applies for the whole wall region with $(u_B)'_w = -(v_B)'_w = u_\tau$, and that u_B and v_B are in phase, we can integrate (2.6) to get

$$\frac{\Lambda_x}{k} \approx 2\pi\sqrt{5} = 14. \tag{2.7}$$

This crude estimate of k gives values which are of the same order as those in table 2.1.

Figure 2.6(a) also shows $u_F'^+$, which is the square root of the sum of the filtered spectra, where the filter is the one defined at the beginning of the section. Note that ${u'_F}^2$ contains both $(u_B)'^2$ and the incoherent contribution of the velocity in the forced modes. Therefore, u'_F agrees with $(u_B)'$ near the wall, and decays with y/Λ_x until the slope of u'_F changes. The wall distance at which the change occurs does not scale with Λ_x, as can be observed in the symbols of figure 2.6(a). On the other hand, when $u_F'^+$ is plotted as a function of y/k in figure 2.6(b), the change in the slope takes place roughly at $y \sim 6k$ for the three rough cases. In the layer below $6k$, limited by the dashed line in the figure, the non-homogeneous contribution from the forcing dominates the background-filtered turbulence, and thus it can be interpreted as the roughness sublayer associated with the disturbed boundary condition. For reference, figure 2.6(b) also includes the energy contained in case **S0** computed with the filter from case **r1**. The wall-normal distance is also normalized with the value of k obtained for **r1**. The collapse of $u_F'^+$ from **r1** and **S0** supports that turbulence is not affected by the boundary condition outside the roughness sublayer.

This roughness sublayer substitutes the buffer region of smooth walls, and it is between it and the outer region where the overlap region is located, $6k < y < 0.2h$. In this region the tangential Reynolds stress is almost constant, and we can apply the same arguments used for the logarithmic region of smooth-walled flows.

2.5. Spectral analysis

More details about the influence of the wall disturbances in the outer region can be extracted from spectral analysis. Figure 2.7(a) shows the premultiplied spectral energy density of the streamwise velocity fluctuations at $\tilde{y}/h = 0.5$ for the disturbed and for the smooth-walled cases. The collapse is excellent except for the longest wavelengths, supporting the hypothesis that the effect of the wall-disturbances is confined to the roughness sublayer. Even better collapse is found for the other two velocity components, in which the large-scale modes contain less energy. The minor differences found in the smallest scales are due to the different Reynolds numbers, since this region of the spectrum collapses when the wavelengths are expressed in wall units.

When we check the wall-normal distribution of ϕ_{uu} (figure 2.7b), we observe that the situation presented in figure 2.7(a) holds for most of the channel, with good agreement between the smooth and the rough cases for $\tilde{y}/h \approx 0.2 - 1$. As expected, strong differences are observed at wall distances corresponding to the buffer region over smooth walls, with the streaks becoming shorter and eventually disappearing as the roughness function increases. This is consistent with the discussion of figure 2.2. In the disturbed cases, the narrow peaks located at $\lambda_x < h$ contain around 13% of the energy in the roughness sublayer, and correspond to the wavenumber of the forcing and to its harmonics. The total energy contained in these modes is ${u'_F}^2$, discussed in §2.4. The other two velocity components and the uv-cospectrum (not shown) for the rough cases also agree with the smooth channel in the outer region. The spectra presented in figure 2.7 are consistent with the agreement in the outer region between the smooth- and rough-walled velocity fluctuation intensities presented in figure 2.3.

These results contradict those reported by Krogstad *et al.* (1992), Krogstad & Antonia (1994) and Krogstad & Antonia (1999) in boundary layers. In their experiments, the roughness strongly affects the wall-normal velocity through the whole layer, and the correlation lengths in the streamwise direction for u and v are twice longer for the smooth-walled case than for the rough-walled one at all heights. Note that, although the spectrum is the Fourier transform of the correlation, separation and wavelengths have different meanings, and it is not possible to directly compare spectra and correlations. Therefore, to check for the change in the correlation lengths in the present simulations, figure 2.8 shows the correlation coefficients ρ_{uu} and ρ_{vv}, which are defined as

$$\rho_{rs}(\delta x, \delta z, \tilde{y}, \tilde{y}_0) = \frac{\overline{r(x, \tilde{y}, z, t) \cdot s(x + \delta x, \tilde{y}_0, z + \delta z, t)}}{r'(\tilde{y}) s'(\tilde{y}_0)}. \tag{2.8}$$

In the above equation $\delta x, \delta z$ are the separations in the homogeneous directions, $\tilde{y}, \tilde{y}_0$ are the wall distances and r, s are the corresponding velocity fluctuations components. The reference wall distance used in figures 2.8(a) and (b) is $\tilde{y}_0 = 0.16h$, the same used in Krogstad & Antonia (1994). There are large differences in the wall region between **S0** and **R2**, both in ρ_{uu} and in ρ_{vv}, located upstream from the reference

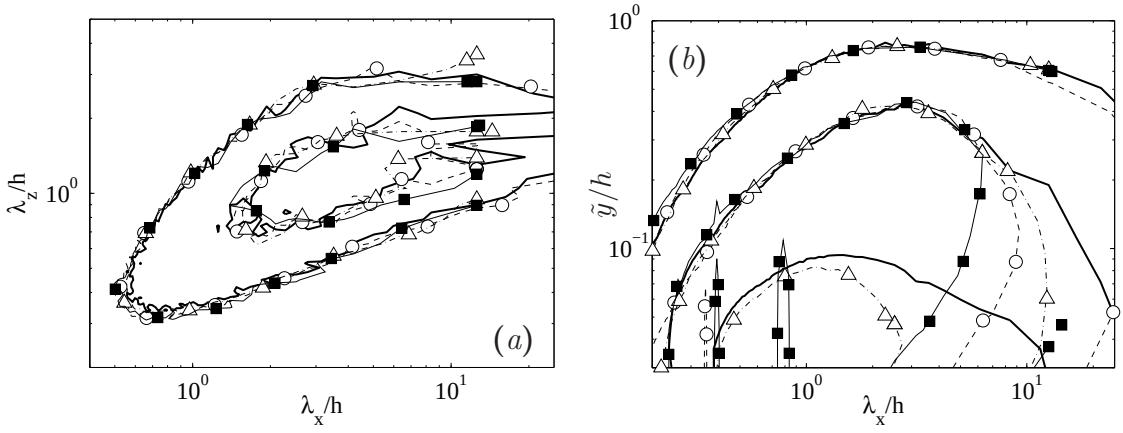

Figure 2.7: Premultiplied spectral energy density of the streamwise velocity, ϕ_{uu}, normalized with u_τ^2. (a) At a fixed wall distance $\tilde{y} = 0.5h$. The contours are 1/3 and 2/3 of the maximum of **S0**. (b) Wall-normal distribution of ϕ_{uu}, integrated for all spanwise wavelengths. The contours are 1/8, 1/4 and 1/2 of the maximum of the smooth case. ——, **S0**; △, **r1**; ○, **R2**; ■, **r3**.

location and at wall distances and streamwise separations that roughly corresponds with the near-wall streaks. There are also smaller differences for $\tilde{y} > 0.2h$, which are clearer for the largest separations of ρ_{uu}. However, these differences do not account for the large changes in the correlation length documented by Krogstad & Antonia (1994), except in the wall region. When the reference height is $\tilde{y}_0 = 0.5h$ (figure 2.8c and d), the contours of the correlation coefficients for **S0** and **R2** coincide better, although some differences are still observed for the longest separations.

In figure 2.8(b) we can observe that the blocking effect of the smooth wall on v is relaxed for the rough-walled case, and the contours of ρ_{vv} in **R2** get closer to the wall than those in **S0**.

2.5.1. Global modes

The differences observed in figure 2.8(a) and (c) between **S0** and **R2** in the outer region for long separations are consistent with those observed in the streamwise velocity spectrum. Note that in figure 2.7(a) there is an energy peak for **S0** for $\lambda_x > 10h$ at $\lambda_z \sim 2h$, which is not visible in **R2**, suggesting that the very long scales are affected by the wall disturbances. In fact, very large structures in turbulent channels are known to be correlated from the wall up to the center of the channel, as shown by Bullock *et al.* (1978) and by del Álamo & Jiménez (2003). It is therefore not surprising that they are modified everywhere in response to changes at the wall. The instantaneous realizations plotted in figure 2.9 confirm that similar large scale streaks are present in the outer region of both the smooth- and the rough-walled cases, and suggest that they are at least qualitatively similar.

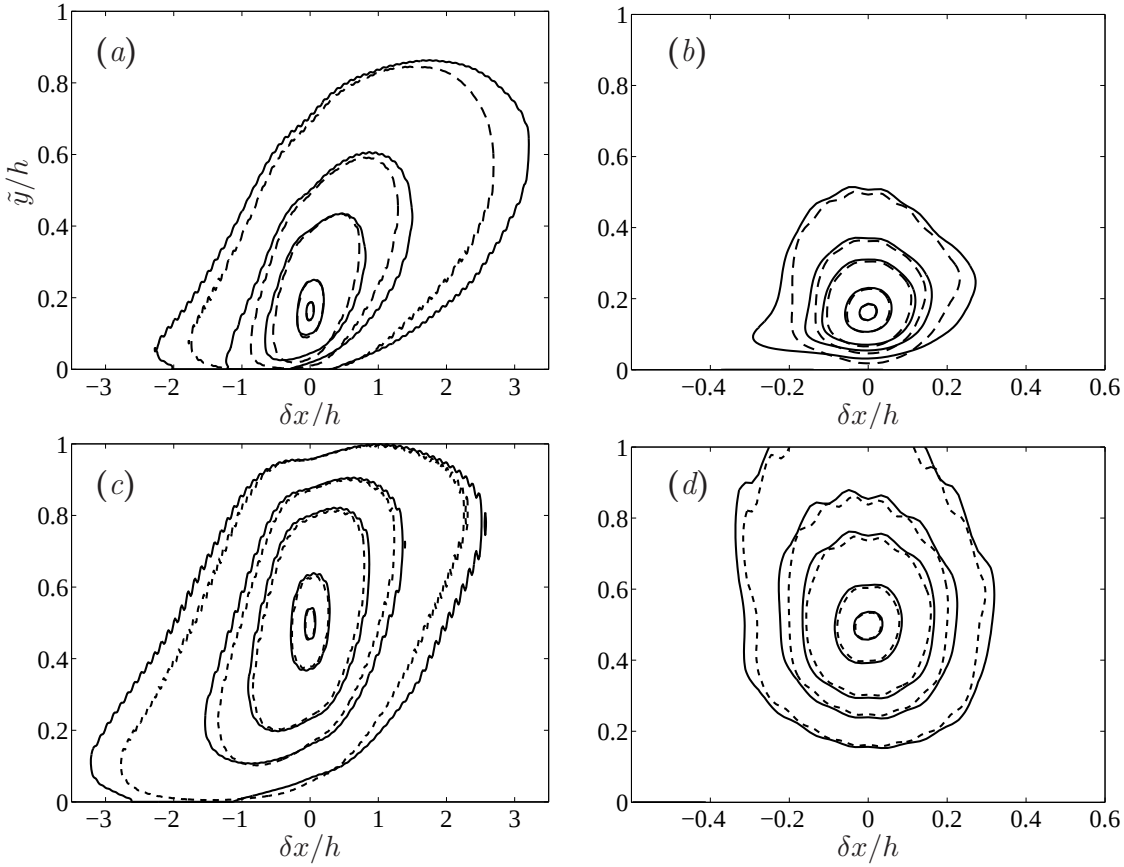

Figure 2.8: Correlation coefficients for zero spanwise separation. (*a*) and (*c*) show ρ_{uu}, (*b*) and (*d*) show ρ_{vv}. The reference wall-distance is $\tilde{y}_0 = 0.16h$ for (*a*) and (*b*), and $\tilde{y}_0 = 0.5h$ for (*c*) and (*d*). The contours corresponds to 0.1, 0.2, 0.3, 0.6, 0.9. ——, **S0**; − − −, **R2**.

In order to perform a quantitative analysis of the global modes over smooth and rough walls, we define the correlation height H_{uu} of the streamwise velocity,

$$H_{uu}^2(\lambda_x, \lambda_z) = \int_0^h \int_0^h C_{uu}(\lambda_x, \lambda_z, y, y_0) dy dy_0, \tag{2.9}$$

where the correlation coefficient C_{uu} between individual Fourier modes is the modulus of the Fourier transform of the spatial correlation ρ_{uu} defined in (2.8). The correlation height of the four cases agree well in figure 2.10(*a*), in particular for the two large boxes, **S0** and **R2**. The global modes, defined as those for which $H_{uu} > 0.75h$, are roughly located in $\lambda_x > 6h$ and $\lambda_z > h$.

In figure 2.10(*b*) we have represented the energies q_{S0} and q_{R2} contained in the modes with streamwise wavelengths in the range $6h < \lambda_x < 24h$ and spanwise wavelengths in the range $\lambda_z > h$. We do not include the energy of the two longest wavelengths of the simulation to avoid effects coming from the long-wavelength

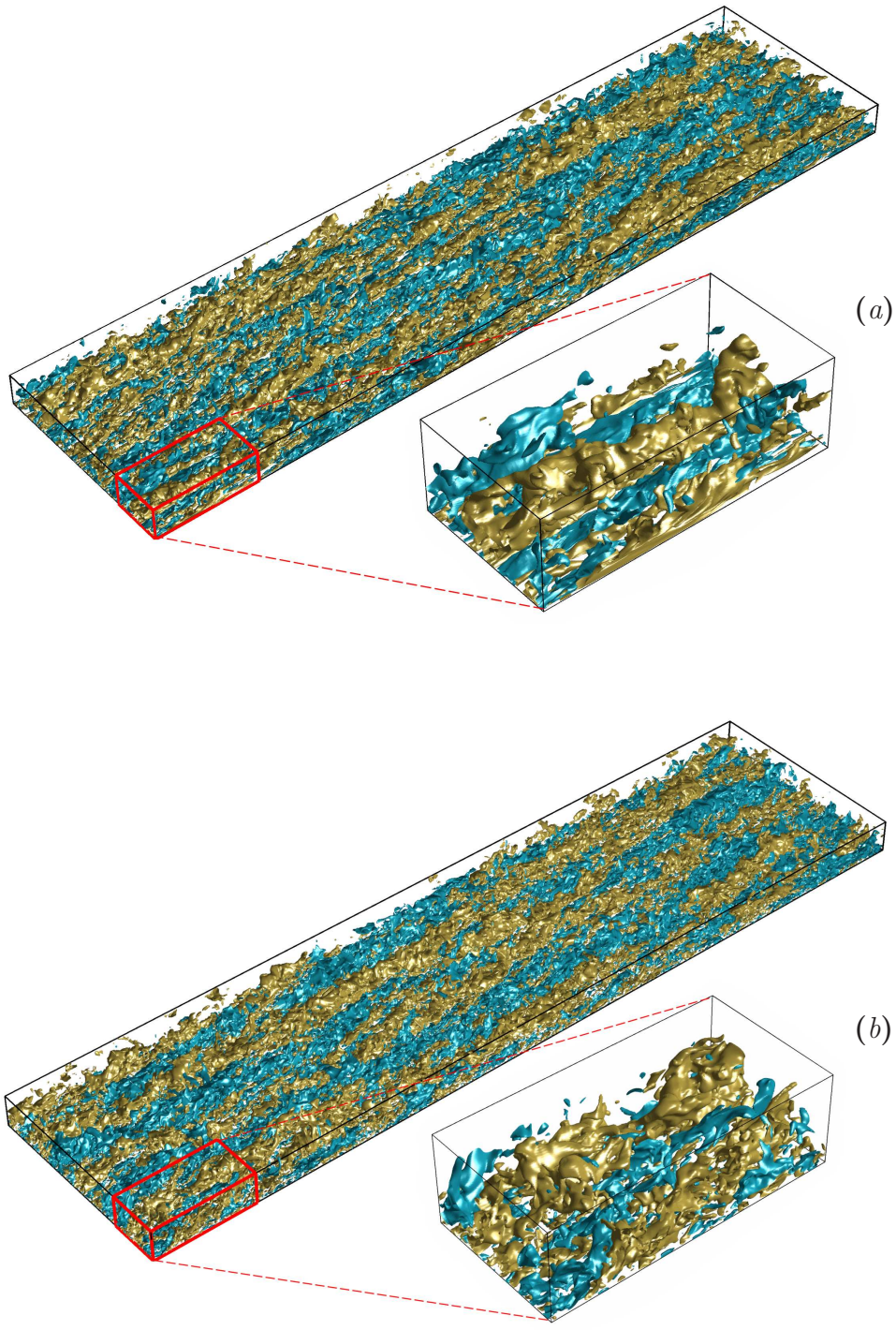

Figure 2.9: Instantaneous isosurfaces $u^+ = 2$ (blue) and $u^+ = -2$ (gold). Flow is from left to right. (a), **S0**. (b), **R2**.

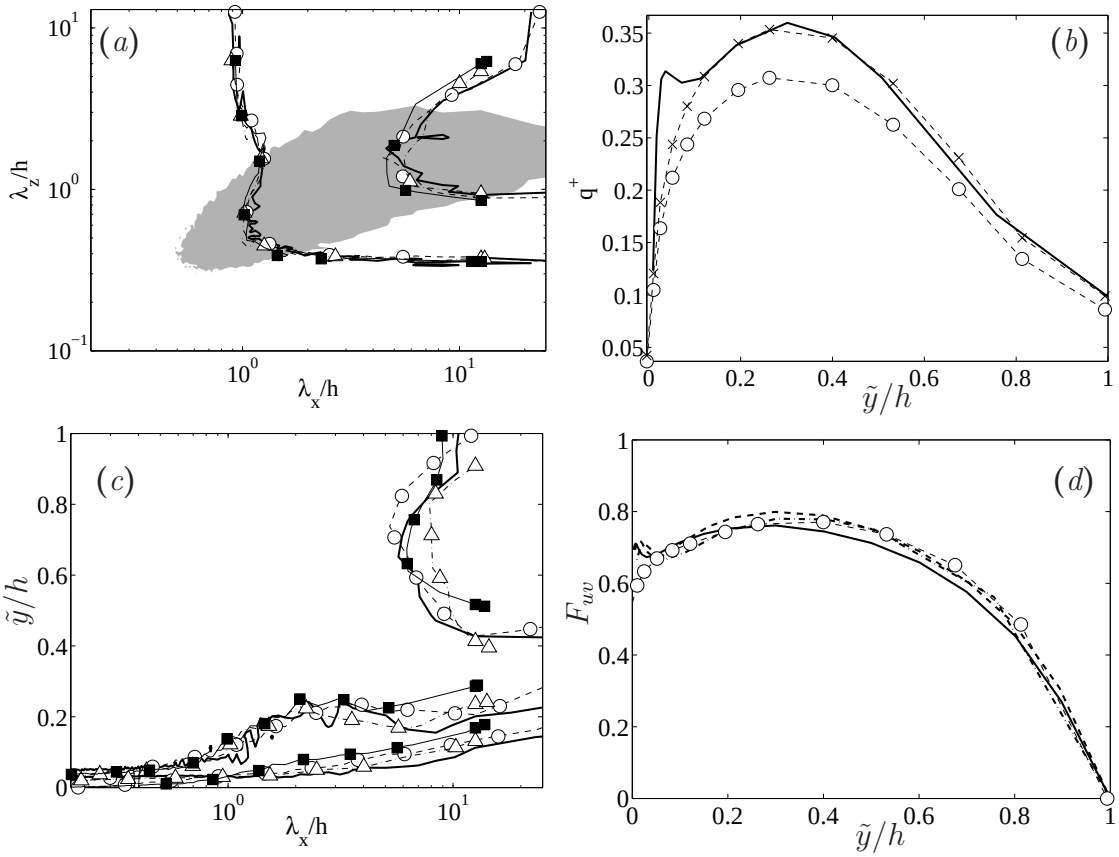

Figure 2.10: (a) Correlation height H_{uu}, defined in (2.9). The contours correspond to 1/2 and 3/4, increasing from left to right. The gray patch corresponds to 1/3 of the maximum of the premultiplied streamwise velocity spectra of case **S0**, at $\tilde{y} = 0.5h$. (b) Energy contained in the global modes, $6h < \lambda_x < 24h$ and $\lambda_z > h$. (c) Δc_ω^+ computed for $\lambda_z > h$, defined in (2.4). The contours, from top to bottom correspond to $\Delta c_\omega^+ = -1, 0, 1$. In these three figures ——, **S0**; △, **r1**; ○, **R2**; ■, **r3**. In (c), × is $1.15\, q_{R2}^+$. (d) Structure function F_{uv}, defined in (2.10), computed for $6h < \lambda_x < 24h$ and $\lambda_z > h$. ——, $Re_\tau \approx 2000$ (Hoyas & Jiménez, 2006); − − −, $Re_\tau \approx 950$ (del Álamo *et al.*, 2004); −·−·, $Re_\tau \approx 550$ (**S0**); ○, $Re_\tau \approx 630$ (**R2**).

truncation of the spectra. For the same reason, only the cases in the long boxes **R2** and **S0** are considered. In the figure, the energies normalized with u_τ^2 do not collapse, and the small peak at $\tilde{y} \approx 0.05h$ in q_{S0}^+, which is related to contributions from the near-wall streaks to the global modes, is not present in q_{R2}^+. However, for $\tilde{y} > 0.1h$ the shape of the global modes intensities is the same for **S0** and **R2**, and their differences can be accounted by a constant factor, $q_{S0}^+ \approx 1.15 q_{R2}^+$, as can be observed in the extra line of figure 2.10(b).

The reason why the differences between q_{S0}^+ and q_{R2}^+ are not observed in the streamwise velocity fluctuations presented in figure 2.3(a) is because their effect is

weak for the present Re_τ. The fraction of the total energy at each wall distance carried by the global modes is less than 25% for the present Reynolds numbers. Therefore, the difference shown in figure 2.10(b) corresponds to less than 4% of the total energy.

Figure 2.10(c) shows the $\lambda_x - y$ distribution of the advection velocities Δc_ω^+ defined in (2.4), averaged over those modes with $\lambda_z > h$. They compare well, specially for the two cases computed on large boxes, suggesting that the dynamics of the global modes are essentially the same over smooth and rough walls, even when their intensity is not.

In figure 2.10(d) we see another indicator of that the differences observed in the global modes over smooth and rough walls are caused by a difference in their velocity scale rather than by a different structure or dynamics. This figure shows the structure function

$$F_{uv} = \frac{-\mathrm{Re}\overline{(\hat{u}\hat{v}^*)}_\Omega}{\sqrt{\overline{(\hat{u}\hat{u}^*)}_\Omega \, \overline{(\hat{v}\hat{v}^*)}_\Omega}}, \tag{2.10}$$

where the average $\overline{(\cdot)}_\Omega$ stands for time averaging over the Fourier domain Ω, $6h < \lambda_x < 24h$ and $\lambda_z > h$. Only data from long computational boxes are included in the figure, as well as two extra numerical experiments of turbulent channels with smooth walls at $Re_\tau = 950$ (del Álamo *et al.*, 2004) and $Re_\tau = 2000$ (Hoyas & Jiménez, 2006).

The profiles of F_{uv} from the disturbed and the smooth-walled cases compare well, specially for **S0** and **R2** outside the wall region. The small differences observed are more plausibly connected to Reynolds number effects. This collapse again supports the idea that the wall does not modify the structure and the dynamics of the global modes. Moreover, the high value of F_{uv} on most of the channel shows that u and v are strongly correlated for long streamwise wavelengths. This implies that the global modes are very efficient generating Reynolds stresses, which had already been reported by del Álamo & Jiménez (2001) for smooth-walled turbulent channels.

According to del Álamo *et al.* (2004), the proper scale for the energy in the global modes in turbulent flows over smooth walls is U_c^2, because they are created by stirring the mean velocity profile all across the channel height. However, figure 2.10(b) shows that this scaling fails for our disturbed case, because the ratio of the energy in the global modes of **S0** and **R2** is much smaller than the actual ratio of their centerline velocities. The same happens with the mixed scaling ($u_\tau U_c$) of de Graaff & Eaton (2000).

This evidence opens two possibilities. Either the velocity scale of the global modes depends on the roughness or it does not. Unfortunately, the present simulations do not provide enough data to analyze this question directly. However, the scaling of the global modes is also eventually felt in the intensity of the streamwise velocity fluctuations in the outer region as the Reynolds number increases, and there are more experimental intensities than spectral data in the literature. Note that rough-walled flows are very sensitive indicators for any anomalous scaling of

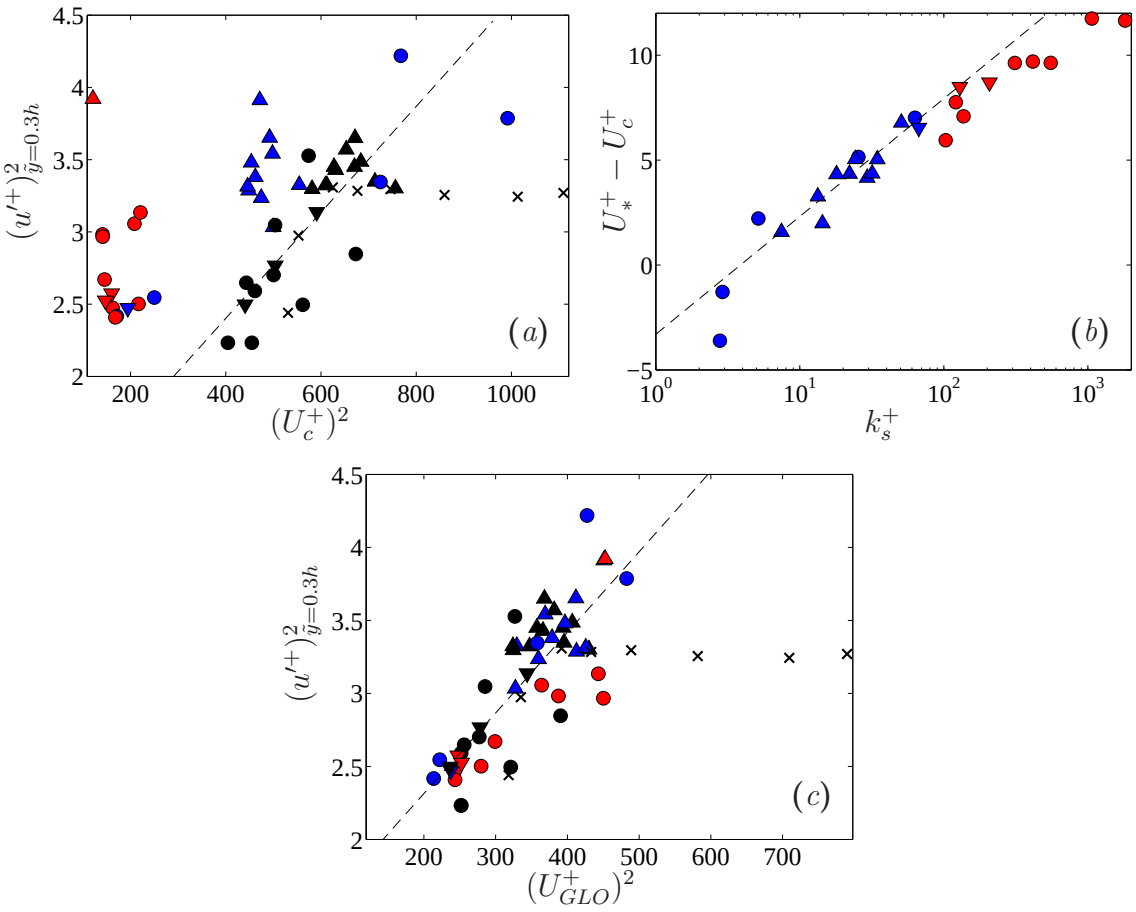

Figure 2.11: (a) Streamwise velocity fluctuations at $\tilde{y} = 0.3h$ as a function of $(U_c^+)^2$. (b) Difference between U_c^+ and the *ad hoc* velocity scale U_*^+ for rough-walled flows. (c) Streamwise velocity fluctuations at $\tilde{y} = 0.3h$ as a function of $(U^+_{GLO})^2$. Black symbols denote smooth-walled flows, blue symbols denote transitionally rough flows, while red symbols are used for fully rough flows with $k_s^+ > 100$. ○, channels from Ashafarian *et al.* (2004), Bakken *et al.* (2005) and Comte-Bellot (1965); △, pipes from Sabot *et al.* (1977), Perry & Abell (1977) and Perry *et al.* (1986); ×, superpipe data from Morrison *et al.* (2004); ▽, present channels, del Álamo *et al.* (2004) and Hoyas & Jiménez (2006). In (a), − − −, is (2.12). In (b), − − −, is (2.13). In (c), − − −, is $(u'^+)^2 = 1.2 + 5.5 \times 10^{-3} \, (U^+_{GLO})^2$.

the fluctuations, because their range of U_c is larger than in smooth-walled flows. We will limit our selves to turbulent flows in channels and pipes, because the structure of the global modes in the outer region of boundary layers might be different (Monty *et al.*, 2007).

Following del Álamo *et al.* (2004), the intensity of the streamwise velocity fluctuations when $\tilde{y}/h \gtrsim 0.2$ should have the form

$$u'^2 \sim \log^2(h/\tilde{y}) u_\tau^2 + f(\tilde{y}/h) U_0^2. \tag{2.11}$$

In this expression u'^2 has two components, one coming from the active eddies, proportional to u_τ^2, and another one proportional to the square of the characteristic velocity of the global modes, U_0. The proposition of del Álamo *et al.* (2004) is that $U_0 = U_c$, a possibility that is explored in figure 2.11(a), where we have plotted $(u'^+)^2$ at a given wall distance, $\tilde{y}/h = 0.3$, for several pipes and channels. The color of the symbols indicate the flow regime: hidraulycally smooth (black), transitionally rough (blue) of fully rough (red). We can see in the figure a relatively good collapse of the smooth-walled data along the dotted line corresponding to the linear law

$$(u'^+)^2 = 0.94 + 3.7 \times 10^{-3} \, (U_c^+)^2, \tag{2.12}$$

which is a particular case of (2.11) with $U_0 = U_c$, except for the single unexplained data set from Morrison *et al.* (2004). As expected, the different rough-walled cases do not collapse on the same law, and their streamwise velocity fluctuations intensities are generally higher than those expected from their centerline velocities.

We therefore work backwards and define U_* as the velocity scale that collapses each rough-walled data point of figure 2.11(a) onto (2.12), and plot in figure 2.11(b) the values of $U_*^+ - U_c^+$ as a function of the equivalent sand roughness. The data collapse around the line

$$U_*^+ - U_c^+ = \kappa^{-1} \log(k_s^+) + A^+ - 8.5 = \Delta U^+. \tag{2.13}$$

This suggests that $U_{GLO} = u_\tau \kappa^{-1} \log(Re_\tau)$ could be a better velocity scale for the global modes than U_c. We test this scaling in figure 2.11(c), where we can observe that the rough- and smooth-walled data now compare much better. Note that while U_* is computed *ad hoc* for each data point of figure 2.11(a), U_{GLO} is computed *a priori* for figure 2.11(c). Similar results are obtained for other wall distances in the range $\tilde{y}/h > 0.2$. Since for smooth-walled flows $U_c^+ - U_{GLO}^+$ is constant to a first order approximation, using $U_0 = U_{GLO}$ instead of $U_0 = U_c$ only introduces a small square root correction to the law given by del Álamo *et al.* (2004). This correction is not observable when comparing the collapse of smooth-walled data over the limited range of U_c in figures 2.11(a) and 2.11(c).

The collapse of the rough-walled cases along the linear law plotted in figure 2.11(c) needs some discussion. According to the arguments presented in §1.2.1, the turbulent structures of rough-walled flows in the fully rough regime should not depend on the viscosity ν. On the other hand, this dependence is expected in the transitionally rough regimes and in the smooth-walled cases, where viscosity is always important near the wall. Note that only three data sets in figure 2.11 correspond to the fully rough regime: the pipe of Sabot *et al.* (1977) at $(u'^+)^2 \sim 4$, the experimental channels of Bakken *et al.* (2005) and cases **R2** and **r3**. It could be argued the channels of Bakken *et al.* (2005) show a leveling-off around $(u'^+)^2 \sim 3$, which would be consistent with the classical theory. Definitely, data over smooth and rough walls at $Re_\tau \gtrsim 2 \times 10^4$ (${U_{GLO}^+}^2 \gtrsim 600$) are needed to clarify the scaling of the global modes.

The need of data at higher Reynolds numbers was already pointed out by del Álamo *et al.* (2004), where it was found that in order to distinguish between U_c^2 and $u_\tau U_c$ as scales for the global modes, Re_τ would have to be higher than 10^8. However, the collapse of smooth- and rough-walled flows with U_{GLO} as opposed to U_c is unambiguous, because there are big differences between both quantities in rough- and smooth-walled flows. All that can be said is that u' does not scale exclusively on u_τ, and figures 2.11(a) and 2.11(c) provide strong evidence that the other velocity scale is closer to U_{GLO} than to U_c.

2.6. Conclusions

In the present chapter we have studied the effect of the boundary condition at the wall on the outer region of turbulent channels. The non-slip and impermeability boundary conditions that are natural to smooth walls have been replaced with single-harmonic velocity disturbances with non-zero tangential Reynolds stresses at the wall. Three different forcings have been explored, in order to analyze the effect of the different parameters characterizing the perturbations.

We have shown that the main effect of the wall disturbances in the flow is to modify the mean streamwise velocity gradient in the near-wall region, changing the intercept constant of the logarithmic velocity profile. The disturbances also change the structure of the smooth-walled buffer region, shortening the streaks and the quasi-streamwise vortices. Consequently, the intensities of the streamwise velocity fluctuations and of the streamwise vorticity decrease. On the other hand, the wall-normal and spanwise velocity fluctuations are enhanced by the disturbances in the near-wall region. This increase is related to structures which are approximately isotropic in the wall-parallel plane, and which contribute little to the streamwise vorticity intensity. All these observations are caused by the disruption of the near-wall energy cycle by the disturbances at the wall. The ratio of production to dissipation and the energy flux shows not only that the disturbances interrupt the near-wall energy cycle, but also that the Reynolds stresses imposed at the wall generates an additional energy that is dissipated locally.

Since most of these changes are typically observed in turbulent flows over rough walls, we can interpret the present boundary condition as a method for emulating the effect of the roughness without having to deal with the details of the flow around the roughness elements, as previously suggested by Jiménez (2004). Hence, we have characterized the different wall forcings by their equivalent sand roughnesses. Three of the cases correspond to the fully rough regime, while the remaining one is transitional.

We have analyzed the flow over individual forcing cells by computing the averaged flow field around a single disturbance. The characteristic length scale for the decay of the velocity disturbances is the forcing wavelength, but the tangential Reynolds stress has its own characteristic length scale, k. The height of the layer where the intensity of the forcing and its harmonics prevails over the background turbulence

is roughly $6k$. This layer can be interpreted as a roughness sublayer, which plays in rough-walled flows the same role as the buffer layer over smooth walls.

Special attention has been paid to the effect of our wall disturbances on the outer flow. Using one-point statistics we have shown that the smooth wall values are recovered in the disturbed cases when $\tilde{y}^+$ increases, and all across the outer region. The spectral analysis and the advection velocities have shown that the structure and the dynamics of the detached scales of the core region in the present simulations are not affected by the perturbations imposed at the walls. This conclusion is coherent with the idea that the detached eddies are controlled by the local mean shear, which is only modified within the roughness sublayer. These ideas will be further analyzed in §3.3 in the next chapter.

We have also seen that the structure of the largest scales of the flow is essentially the same over the forced and over smooth walls. They are global modes, in the sense that they are correlated all across the channel. In smooth-walled flows, del Álamo *et al.* (2004) proposed that they scale with the centerline velocity U_c, and that therefore the square of the velocity fluctuations increase with U_c^2 for a given wall distance. We have shown that this scaling does not work for rough-walled flows, and we have proposed a new velocity scale proportional to $u_\tau \kappa^{-1} \log(Re_\tau)$ for the global modes. We have shown that the modified scaling collapses the streamwise velocity fluctuations for smooth- and rough-walled cases, for a wide range of Reynolds numbers and wall roughnesses, even if this collapse is not justified for the fully rough cases.

The results presented in this chapter suggests that the outer flow region is fairly independent on the wall layer, even if the opposite is not true (del Álamo & Jiménez, 2003; Hoyas & Jiménez, 2006). The present results also suggest that even in rough-walled boundary layers it could be expected that the detached eddies remain unchanged, at least if the mean shear does. On the other hand, the effect of the roughness in the largest scales of the outer region of turbulent boundary layers and channels might be different. While the effect of the roughness on the global modes is symmetric in channels, in boundary layers only the wall is modified, and the free stream remains unchanged.

Chapter 3

Vorticity organization in the outer layer of turbulent channels with disturbed walls [1]

3.1. Introduction

We have seen in chapter 2 that the outer region of turbulent channel flows is fairly independent of the details of the wall region. In the present chapter, we extend the comparison between smooth- and rough-walled flows to the coherent structures of vorticity found in the overlap and outer regions. The idea that inner-outer interactions are due to vortex loops connecting the inner and outer layers of turbulent wall flows is a recurrent argument in the literature of wall turbulence (see the review by Robinson, 1991*a*). The analysis presented in this chapter is aimed to clarify the details of that interaction.

The best-known theoretical models for those vortex loops are variations of the vortex hierarchies proposed by Perry & Chong (1982) and Perry *et al.* (1986), loosely based on Townsend's (1976, pages 150–162) attached-eddy hypothesis. Although those models were initially constructed from abstract eddies, with larger elements emerging from smaller ones through unspecified processes, they eventually evolved into collections of Λ-vortices growing from the wall. Such objects have been observed in low-Reynolds-number numerical simulations (Robinson, 1991*b*; Blackburn *et al.*, 1996; Chong *et al.*, 1998), and in experiments with relatively coarse resolutions (Adrian *et al.*, 2000; Ganapathisubramani *et al.*, 2003).

Based on the identification of hairpin-vortex signatures in PIV measurements of turbulent boundary layers, Adrian *et al.* (2000) proposed a model built on packets of hairpins that grow from the buffer region. The packets form due to a non-linear mechanism called *autogeneration* (Zhou *et al.*, 1999), with the hairpins in each packet working cooperatively to generate the long low-momentum ramps observed in their experiments (Meinhart & Adrian, 1995). Signatures of similar packets were

[1] Part of the contents of this chapter have been published in the Journal of Fluid Mechanics, volume 591, pages 145-154, with Javier Jiménez and Juan C. del Álamo as coauthors.

observed in wall-parallel PIV measurements by Ganapathisubramani *et al.* (2003), who showed that the elongated low-momentum regions associated with those signatures were responsible for a large fraction of the Reynolds stresses. Using linear stochastic estimation, Tomkins & Adrian (2003) concluded that the spanwise size of the packets varies linearly with wall-distance, suggesting a self-similar growth in an averaged sense. They proposed that this growth takes place by a combination of self-induction, autogeneration and mergers. A recent revision of the state of the art of the vortex packet paradigm can be found in Adrian (2007).

A different view is emerging from the work of del Álamo *et al.* (2006). They extracted coherent structures of vorticity from DNSes of turbulent channels with friction Reynolds numbers up to $Re_\tau \leq 1900$, and observed that individual vortices with diameters of the order of the Kolmogorov length scale appeared grouped in clusters, similar to the vortex tangles reported by Tanahashi *et al.* (2004). In both works, instantaneous realizations of the largest clusters revealed complex objects in which few hairpin-like vortices could be identified. Note that this is not necessarily inconsistent with the previous deterministic descriptions, which did not usually include a statistical estimation of the frequency of hairpins with respect to other structures. Del Álamo *et al.* (2006) showed that the clusters separate naturally into wall-attached and wall-detached families, and the attached ones have sizes and dimensions similar to the hairpin packets reported in Ganapathisubramani *et al.* (2003) and Tomkins & Adrian (2003). The average velocity field conditioned to these attached clusters consist of a Λ-vortex with a wall-normal velocity ejection between its legs, and an cone-shaped low-momentum wake extending downstream of the cluster.

Based on their observations, del Álamo *et al.* (2006) proposed a model in which wall-normal velocity *bursts*[2] were responsible for the formation of the low-momentum wakes by pumping low-velocity fluid from the wall. They suggested that the higher local dissipation within the burst leads to the percolation of the vortices inside it, implying that the cluster is the consequence of the bursts, rather than their cause. Estimations of the lifetimes of the bursts showed that they were of the order of their eddy turn-over times, suggesting that the clusters could not grow from the wall to their observed sizes, and had to be generated at all sizes and heights. Also, the measured lengths of the conical wakes, and the available velocity difference across the burst, indicated that several bursts had to be associated with a single wake, and that they had to already have been generated in that configuration.

Note that the original hairpin model is hard to reconcile with the Townsend's hypothesis. If the structure of the logarithmic and outer regions is governed by hairpins growing from the wall, it could be possible to change the properties of these regions modifying the properties of young hairpins near the wall, as suggested by Coceal *et al.* (2007). Their arguments contradict the results presented in chapter

[2]Note that the term burst is not used here to refer to the passing of a coherent structure over a sensing element, but to refer the transient ejection of fluid in a region of the flow that evolves coherently until it is dissipated (Kim *et al.*, 1971).

Case	Re_τ	L_x/h	L_z/h	Δx^+	Δz^+	Δy_c^+	k_s^+	h_R^+	α_c	N_C	N_{att}
S0	547	8π	4π	13.4	6.7	6.7	–	–	0.0024	1.9×10^6	1.4×10^5
R2	632	8π	4π	11.6	5.8	8.0	129	93	0.0046	2.3×10^6	1.7×10^5
r3	674	4π	2π	12.4	6.2	8.6	207	146	0.0034	1.0×10^6	0.8×10^5

Table 3.1: Parameters of our experiments. L_x and L_z are the streamwise and spanwise dimensions of the domain and h is the channel half-height. Δx and Δz are the streamwise and spanwise collocation resolutions. Δy_c is the wall-normal resolution at the center line. In cases **R2** and **r3**, k_s is the equivalent sand roughness height and h_R is the height of the roughness sublayer, defined in 2.4. α_c is the percolation threshold, N_C is the number of extracted clusters, and N_{att} is the number of those classified as wall-attached.

2, where we have shown that the structures of the outer region of turbulent channels are rather insensitive to the details of the walls, except for the long wavelength limit of the streamwise velocity spectrum. The latter are global modes, correlated across the whole flow thickness, and they feel the effect of the wall trough the changes in their characteristic velocity scale, nor through modifications of their dynamics.

In this chapter we analyze the effect of the wall on the coherent structures of vorticity that populate the outer region, by comparing the vortex clusters extracted from the DNSes of turbulent channels with smooth and rough walls presented in chapter 2. The organization of the chapter is as follows. Section 3.2 describes the vortex identification method. The geometrical properties and spatial distributions of the wall-detached clusters are described in §3.3, while those of the attached clusters are analyzed in §3.4. Finally, the conditionally averaged velocity fields are discussed in §3.5, and section 3.6 concludes.

3.2. Cluster identification methodology

The DNSes described in chapter 2 are used here to analyze the effect of the wall on the vortical structures populating the logarithmic and outer region of turbulent channels. Only the cases **R2**, **r3** and **S0** will be used here. The case **r1** has been excluded from the analysis because it is transitionally rough. On the other hand, **R2** and **r3** correspond to fully rough cases, where the near-wall energy cycle has been effectively destroyed by the velocity disturbances imposed at the walls. The reference smooth-walled turbulent channel is **S0**, with a friction Reynolds number comparable to the wall-disturbed cases. An extensive list of the parameters of the three simulations is presented in table 2.1, although table 3.1 recovers some of them here in order to ease the reading of the chapter.

We employ the method described by del Álamo *et al.* (2006) to extract $O(10^6)$ vortex clusters from instantaneous flow realizations. A vortex cluster is defined as a set of connected points where the discriminant D of the velocity gradient tensor is larger than a certain fraction of its standard deviation D' in the wall parallel plane,

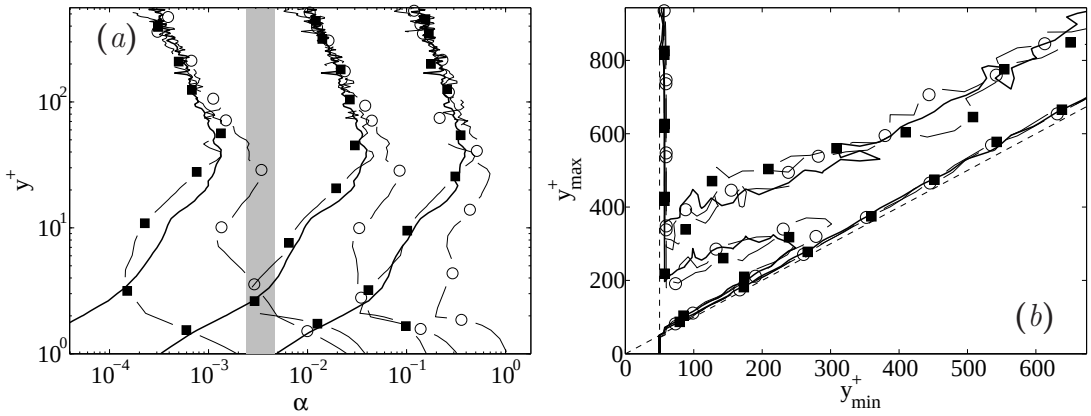

Figure 3.1: (a) Isolines of the relative volume V_r occupied by the points satisfying the relation (3.1) as a function of the threshold α and of the wall distance. The levels represented are, from left to right, $V_r = 0.2, 0.04, 0.008$. The gray strip covers the range of variability of α_c for the present experiments. (b) Volume distribution p_V of the clusters as a function of their minimum and maximum wall distances, $y_{\min}$ and $y_{\max}$. The levels contain 60 and 85% of the data. The vertical dotted line is $y^+_{\min} = 50$ and the diagonal one is $y_{\min} = y_{\max}$. ——, **S0**. ○, **R2**. ■, **r3**.

$$D > \alpha D'(y). \tag{3.1}$$

Figure 3.1(a) shows the relative volume V_r occupied by the clusters as a function of α, and of the wall distance. The three flows agree fairly well above the roughness sublayer, $y^+ > 100 \approx h_R^+$, but differ appreciably below that level, especially for $y^+ \leq 50$. These discrepancies lead to different connectivities in the roughness sublayer which affect all the wall-attached objects, including those reaching into the logarithmic and outer layers. We therefore apply the cluster identification algorithm to the truncated domain $50 < y^+ < 2Re_\tau - 50$ for the three flows in table 3.1, which allows us to compare consistently the clusters from the rough- and the smooth-walled cases. The results obtained from full channels, and from channels truncated at other wall distances, agree qualitatively with those presented here.

In our analysis, we use $\alpha = 0.0055 \approx \alpha_c$, where α_c is the critical threshold below which a cluster percolates throughout the truncated channel (see table 3.1). The percolation thresholds from cases **S0**, **R2** and **r3** differ little from one another, taking into account that α multiplies a sixth power of the vorticity. This is emphasised by the narrowness of the gray bar representing the range of variability of α_c in figure 3.1(a). The value of α used here is closer to the percolation threshold than that used by del Álamo *et al.* (2006), because only when $\alpha \approx \alpha_c$ does the vortex distribution become independent of Re_τ in the outer region. This allows us to compare the results from **S0**, **R2** and **r3** despite their different Reynolds numbers. These arguments will be clearer after §3.4.

Figure 3.1(b) shows isocontours of the distribution of volume occupied by the

clusters as a function of the minimum and maximum wall distances of these objects, $p_V(y_{\min}, y_{\max})$. Similar to the smooth wall cases reported by del Álamo *et al.* (2006), the shape of p_V suggests that the population of clusters in rough-walled channels may be divided into a wall-detached and a wall-attached family. The wall-detached family is the wide inclined strip where the volume distribution is approximately homogeneous, $p_V \approx p_V(y_{\max} - y_{\min})$, and is formed by clusters that reside away from the wall. The wall-attached family is the thin vertical strip formed by clusters whose minimum wall distance coincides with the boundary of the truncated-height channel, $y^+_{\min} = 50$. Two examples of clusters of the wall-attached family have been highlighted from their background vorticity in figure 3.2. They are particularly large examples of these objects, with a wall-normal height around $600\nu/u_\tau$, a streamwise length around $2000\nu/u_\tau$ and a spanwise width close to $1000\nu/u_\tau$.

Because the present definition of attached cluster is slightly different from that used in del Álamo *et al.* (2006) ($y^+_{\min} < 20$), we classify as attached some objects that they would have classified as detached. However, the differences are small, especially for large clusters reaching the outer region. The analysis of $p_V(y_{\min}, y_{\max})$ in full channels (plotted in del Álamo *et al.*, 2006) shows that 25% of the clusters in **S0** with $y^+_{\max} = 100$, and 10% of those with $y^+_{\max} = 200$, switch families between the two definitions. These figures only represent 6% of the total cluster population. Similar results are obtained for cases **R2** and **r3**.

In the following sections, we analyze the wall-attached clusters over the disturbed walls to evaluate the possibility of inner-outer interactions caused by vortex loops emanating from the buffer layer. We focus on them because they are important for the dynamics of the outer region, and because their wall-attached nature might cause them to depend on the details of the wall. Before that, the detached clusters are briefly analyzed in the next section. They will be shown to be essentially dissipative eddies that are not affected by the wall.

3.3. The geometry and distribution of the detached clusters

Figure 3.3(a) shows p.d.f.s of the logarithms of the wall-parallel sizes and wall distances of the detached clusters in the present flows. The position and size of a detached cluster are defined equal to those of its circumscribed Cartesian box, and are denoted (x_c, y_c, z_c) and $(\Delta_x, \Delta_y, \Delta_z)$ respectively. In the preparation of the figure, those objects with $\Delta_x < 12\eta_k(y_c)$ or $\Delta_y, \Delta_z < 9\eta_k(y_c)$, where η_k is the local Kolmogorov scale, have been rejected because their size is comparable to the resolution of our simulations. The data show that the sizes of the detached clusters are proportional to $\eta_k(y_c)$ and comparable to the enstrophy containing scales. The latter are represented in figure 3.3(a) by the shaded contours, which are isolines of the spectral enstrophy density from case **S0**. This result agrees with the scaling of the detached clusters reported by del Álamo *et al.* (2006) for smooth channels and

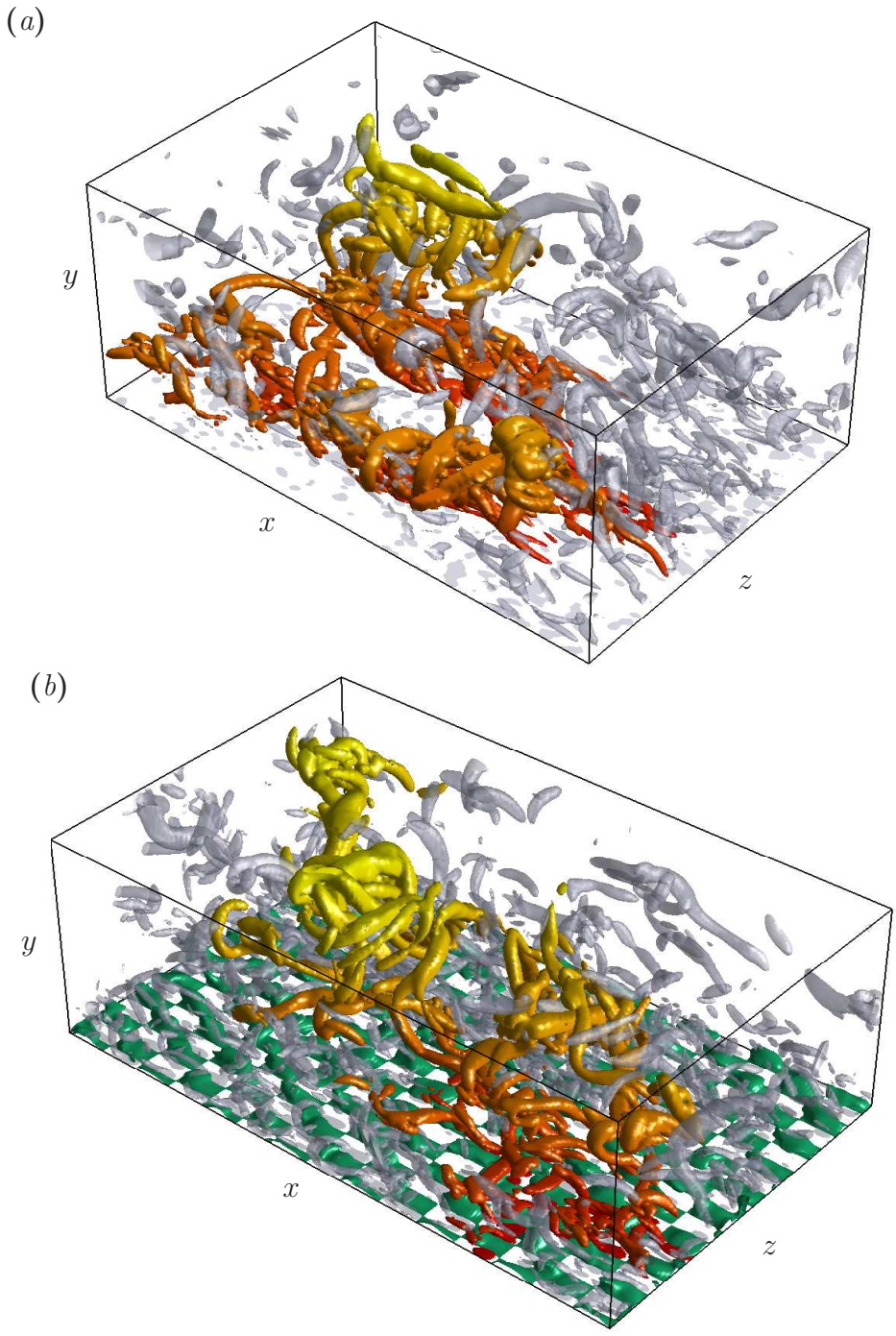

Figure 3.2: Isosurfaces of $D = 0.0055D'$, for cases **S0** (a) and **R2** (b). The attached cluster is colored with the wall-normal distance, while the translucent objects are the background structures surrounding it. The green surfaces at the bottom wall in (b) are surfaces of $u = 0$, and represent the wall-disturbances. In both cases, the size of the plotted domain is approximately $(2000 \times 600 \times 1000)\nu/u_\tau$, and the mean flow goes from right to left.

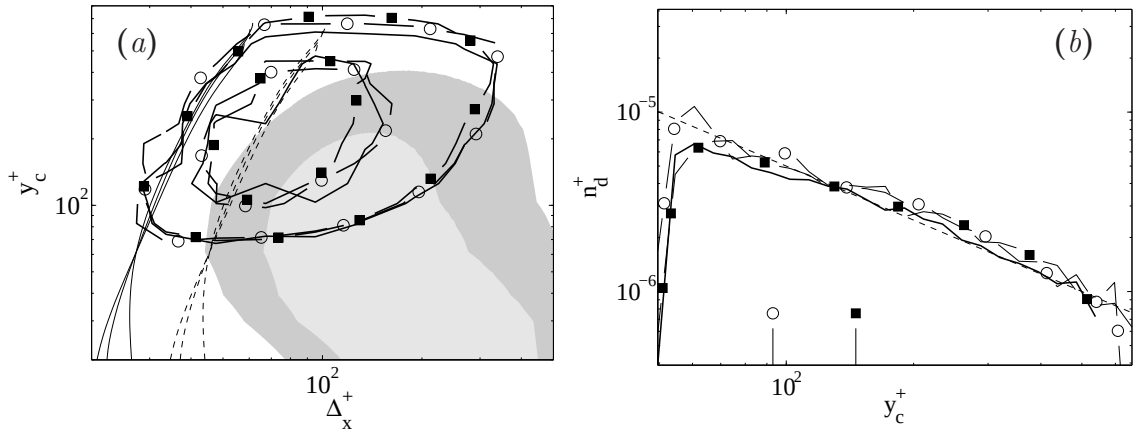

Figure 3.3: (a) Joint p.d.f.s of the logarithm of the lengths of the detached clusters and the wall distances of their centers, $p_\Delta(\Delta_x^+, y_c^+)$, . The contours contain 40 and 90% of the data. The shaded contours are the spectral enstrophy density from **S0**. The levels represented are 1/2 and 3/4 of its maximum. We have used the correspondence $\lambda \sim \Delta$ and $y \sim y_c$ to compare the p.d.f.s and the spectral density. The dashed lines show $\Delta^+ = 20\eta_k(y_c)^+$ for the three channels, while the solid lines show the limit $\Delta^+ = 12\eta_k(y_c)^+$. ($b$) Density n_d^+ of detached clusters per unit wall-parallel area and unit height as a function of y_c^+. The vertical lines indicate $y = h_R$ for the rough-walled cases. The dashed line is $n_d^+ \propto 1/y_c^+$. ——, **S0**. ○, **R2**. ■, **r3**.

indicates that these objects are not affected by the nature of the wall.

Likewise, the wall forcing does not influence the volume density of detached clusters, which is denoted n_d^+ and has been plotted in figure 3.3(b). This magnitude scales as $n_d^+ \sim 1/y^+$, in agreement with the properties of the vortices of isotropic turbulence reported by Jiménez & Wray (1998). The radius of these vortices is of the order of η and their length is of the order of the Taylor microscale λ, yielding a volume $V_1 \sim \eta^2\lambda$. In turbulent channels we have $\eta^+ \sim (y^+)^{1/4}$ and $\lambda^+ \sim (y^+)^{1/2}$, so V_1 increases with the wall distance as $V_1^+ \sim y^+$. Assuming that the total volume V^+ occupied by the detached vortices does not depend on y far from the wall, which is supported by figure 3.1(b), we obtain $n_d^+ \sim V^+/V_1^+ \sim 1/y^+$.

Finally, the behaviour of the densities of detached clusters in the roughness sublayer ($y_c^+ \lesssim 100 \sim h_R^+$) is consistent with the results presented in figure 3.1(a), with higher V_r and n_d^+ for case **R2** than for cases **r3** and **S0**.

3.4. The geometry and distribution of the attached clusters

Figure 3.4(a) shows joint p.d.f.s of the streamwise and wall-normal sizes of the attached clusters (Δ_x, Δ_y), defined as in §3.3. In del Álamo *et al.* (2006), the

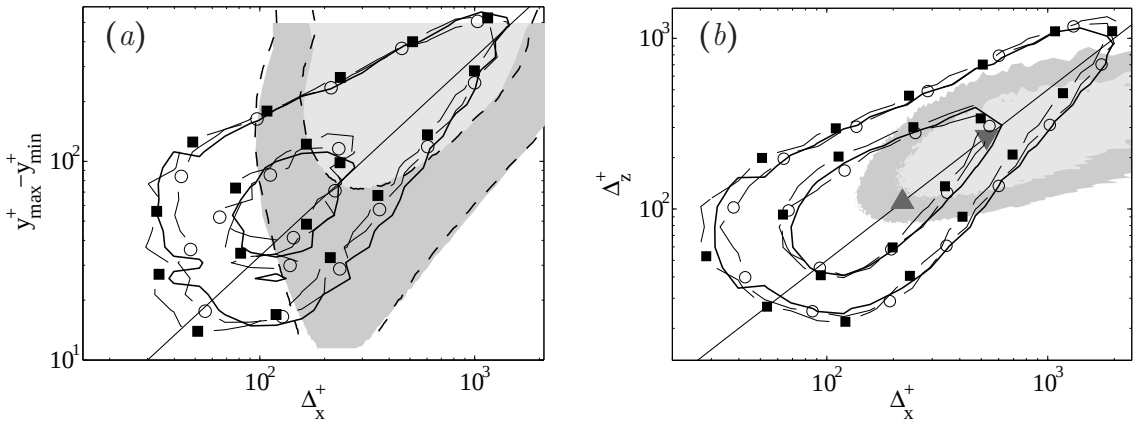

Figure 3.4: Joint p.d.f.s of the logarithms of the wall-parallel sizes and wall-normal height of the attached clusters. (*a*) $p_\Delta(\Delta_x^+, \Delta_y^+)$, the contours containing 40 and 94% of the data. The shaded patches are contours of the premultiplied spectral density $\phi_{vv}(\lambda_x, y - y_{\min})$ from case **S0**, while the dashed lines correspond ϕ_{vv} from case **R2**. We have plotted the levels 1/4 and 1/2 times the maximum of ϕ_{vv}, using the correspondence $\lambda \sim \Delta$. (*b*) $p_\Delta(\Delta_x^+, \Delta_z^+)$ for the tall attached clusters with $y^+_{\max} > 100$, the contours containing 40 and 90% of the data. The shaded contours come from the uv-coespectrum of case **S0** $y^+ = 100$, at 1/20 and 1/5 of its maximum. The shaded triangles show the wavelengths of the wall forcing for cases **R2** ($\triangle$) and **r3** ($\triangledown$). In both panels, the straight solid line is (3.2). ——, **S0**. $\circ$, **R2**. ■, **r3**.

attached clusters had $y^+_{\min} < 20$, and it was assumed that $\Delta_y = y_{\max} - y_{\min}$ was roughly equal to $y_{\max}$. Here, the actual minimum wall distance of the attached clusters very likely lies below the truncation level, $y^+_{\min} = 50$. Since this cutoff can be an appreciable fraction of the cluster height, $y_{\max}$ seems a better measure of that height than Δ_y. However, Δ_y is used in the abscissae of figure 3.4(*a*) because the length of the cluster Δ_x is only measured above $y^+_{\min} = 50$.

In the preparation of the figure, clusters with vortex volumes smaller than 30^3 wall units have not been considered because their sizes are of the order of the simulation grid. The results show that the distributions of sizes of the attached clusters do not depend on the wall forcing, with the only exception of the clusters that are fully contained in the roughness sublayer of channels **R2** and **r3** ($\Delta_y^+ \lesssim 50$). Even in that case, the size of the clusters is not set by the wavelength of the forcing. Similar results are obtained for $p_\Delta(\Delta_z^+, \Delta_y^+)$ (not shown) and in $p_\Delta(\Delta_x^+, \Delta_z^+)$, shown in figure 3.4(*b*). In all of these distributions, the clusters from the three cases show the self-similar scalings reported by del Álamo *et al.* (2006),

$$\Delta_x \approx 3\Delta_y, \quad \text{and} \quad \Delta_x \approx 2\Delta_z. \tag{3.2}$$

Figure 3.4(*a*) also includes the spectral energy density of v for **S0** (shaded) and **R2** (dashed lines), as functions of $y - y_{\min}$, showing the good agreement between the rough- and the smooth-walled cases. Furthermore, the most energetic scales

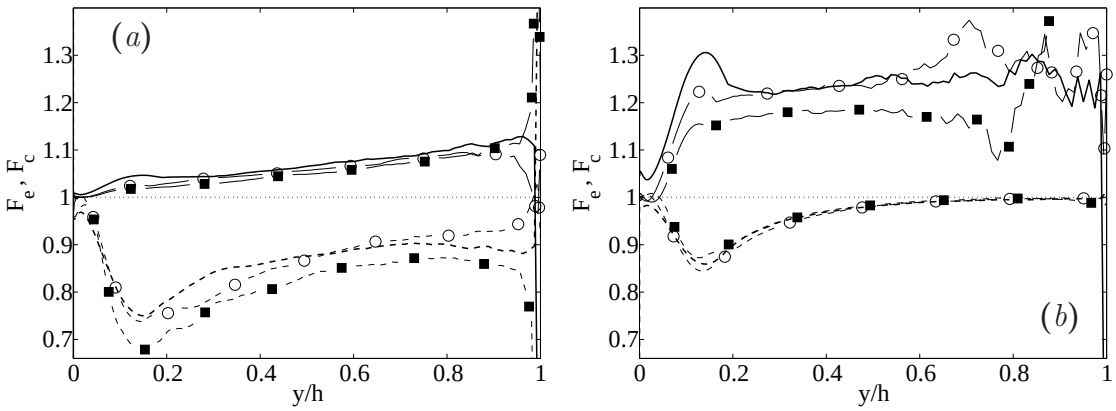

Figure 3.5: Averaged Reynolds stresses in the areas covered/not-covered by attached clusters with $y^+_{\max} > 100$, as defined in (3.3). (a), $\alpha = 0.0055$. (b), $\alpha = 0.022$. Solid lines correspond to F_c, while dashed lines corresponds to F_e. ——, **S0**. ○, **R2**. ■, **r3**.

coincide reasonably well with the cluster sizes, suggesting that the attached clusters are associated to wall-normal velocity structures. Notice that this conclusion is not invalidated by the imperfect agreement in figure 3.4(a), because the correspondence between wall distance and cluster height is only approximate, and because sizes are proportional but not equal to spectral wavelengths (Jiménez *et al.*, 2004). The relationship between the clusters and wall-normal velocity structures was already pointed out in del Álamo *et al.* (2006).

Figure 3.4(b) also shows a fair agreement between the sizes of the largest attached clusters and the energy containing scales of the uv-coespectrum, suggesting that these objects contribute to the Reynolds stress and are hence active in Townsend's (1976) sense. Further analysis reveals that the largest clusters are actually "super-active" both in rough and smooth channels. In order to quantify the intensity of the Reynolds stress of the attached clusters, we define the ratios

$$F_c = \frac{\overline{(uv)_c}}{\overline{(uv)}}, \text{ and } F_e = \frac{\overline{(uv)_e}}{\overline{(uv)}}, \tag{3.3}$$

where $\overline{(uv)}$ are the total Reynolds stress, $\overline{(uv)}_c$ are the Reynolds stresses averaged in the area occupied by the boxes circumscribed to attached clusters, and $\overline{(uv)}_e$ are the Reynolds stress averaged in the remaining area.

Figure 3.5(a) shows F_c and F_e computed for clusters with $y^+_{\max} \geq 100$. We can observe that in the logarithmic layer $\overline{(uv)}_c$ is roughly 5% higher than $\overline{(uv)}$. However, when in figure 3.5(b) the identification threshold α is increased to $\alpha = 0.022$ (in order to extract the most intense structures), F_c increases to 1.2 in the logarithmic layer, confirming that the attached clusters are "superactive". Of course, as α increases, the volume occupied by the clusters diminishes (see figure 3.1a), and F_e approaches unity.

Ganapathisubramani *et al.* (2003) also found that the Reynolds stress in low-momentum regions matching hairpin packets were very strong, with instantaneous values up to $40u_\tau^2$. The contribution of these regions to the total Reynolds stresses were about 25%, even when they only covered a 4.5% of the total area. In the present case, the area covered by the boxes circumscribing attached clusters with $y^+_{\max} > 100$ and $\alpha = 0.022$ is roughly 35%, and they account for roughly 40% of the total Reynolds stress of the channel in the logarithmic region. The differences in the relative areas between the present work and Ganapathisubramani *et al.* (2003) can be explained taking into account that, as reported by del Álamo *et al.* (2006), the vortices forming the cluster are organized in surfaces or shells. Therefore, while the latter authors measure the contributions from the low-momentum and strong Reynolds stress regions, here we measure the contribution from the boxes that circumscribe the tall attached clusters, resulting in larger relative areas. Note that the relative volumes reported in figure 3.1(a) show reasonable agreement with the relative areas reported by Ganapathisubramani *et al.* (2003).

It is also interesting to check the effect of the wall forcing on the density of attached clusters in the outer region. We have seen in figure 3.1(a) that the wall disturbances in cases **R2** and **r3** drastically increase the relative area ocuppied by vortical structures below $y^+ = 50$, and it could be argued that if the attached clusters are grown from these structures, they should be more frequent in the outer region of the wall-disturbed cases. Figure 3.6(a) shows that this is not the case. The figure shows the density of attached clusters per unit wall parallel area and unit height, n_a, as a function of the cluster height, $y_{\max}$. We have only considered those clusters whose volume is larger than 30 cubic wall units. Consistent with figure 3.4(a), the cluster densities from our three channels peak near $y^+_{\max} = 100$ and agree fairly well. Del Álamo *et al.* (2006) reported that the decay of the density of tall attached clusters in smooth channels is described by power laws $n_a^+ \propto (y^+_{\max})^\beta$, where β depends on the identification threshold α. They noted that because the lengths and widths of these objects are proportional to their heights, their influence may reach the outer region even if their density decreases steeply with y. That influence becomes independent of Re_τ and only decays logarithmically with the wall distance for $\beta = -3$, which is precisely the logarithmic slope of the dashed line that fits the data from smooth and rough channels in figure 3.6(a).

Figure 3.6(b) illustrates this behavior by displaying the decay exponent of n_a as a function of the identification threshold. For each case, β is determined by computing a least squares linear fit to $\log(n_a^+)$ in the range $200 < y^+_{\max} < 500$. The results from smooth and rough channels agree well for all values of α except past the percolation crisis, supporting the independence of the spatial distribution of attached clusters from the nature of the wall. As reported by del Álamo *et al.* (2006), the decay exponent increases as the clusters population growths with decreasing α, but saturates around $\beta = -3$ when the percolation transition is reached.

Finally, the averaged shape of the attached clusters is neither modified by the wall roughness. This is shown in figure 3.7, which presents p.d.f.s of the coordinates

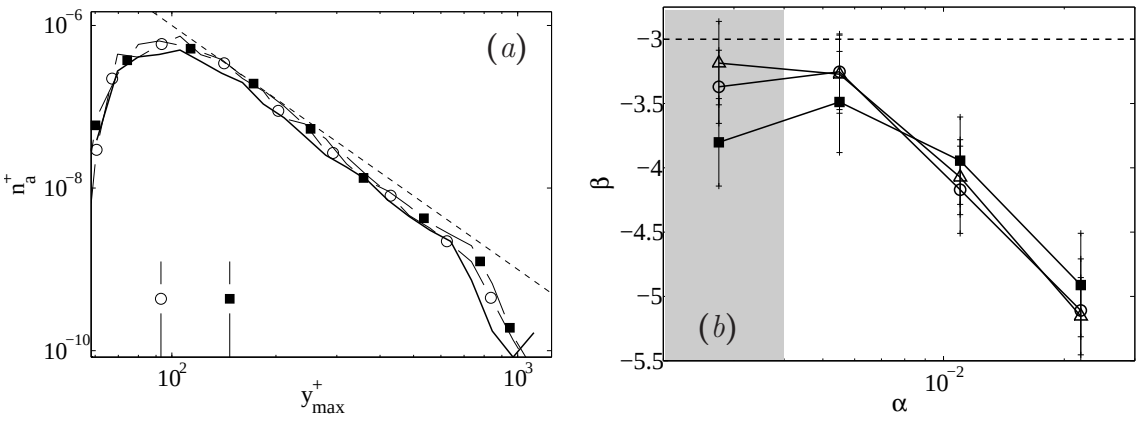

Figure 3.6: (*a*) Density n_a^+ of attached clusters per unit wall-parallel area and unit height as a function of their height; the vertical lines indicate $y = h_R$ for the rough-walled cases. $---$, $n_a^+ \propto (\Delta_y^+)^{-3}$. (*b*) Decay exponent β of n_a as a function α. The vertical lines are 95% confidence intervals for β. The lines are plotted to aid the eye only and the symbols correspond to data points. The shaded area indicates the range of α where the cluster population percolates. ——and △, **S0**. ○, **R2**. ■, **r3**.

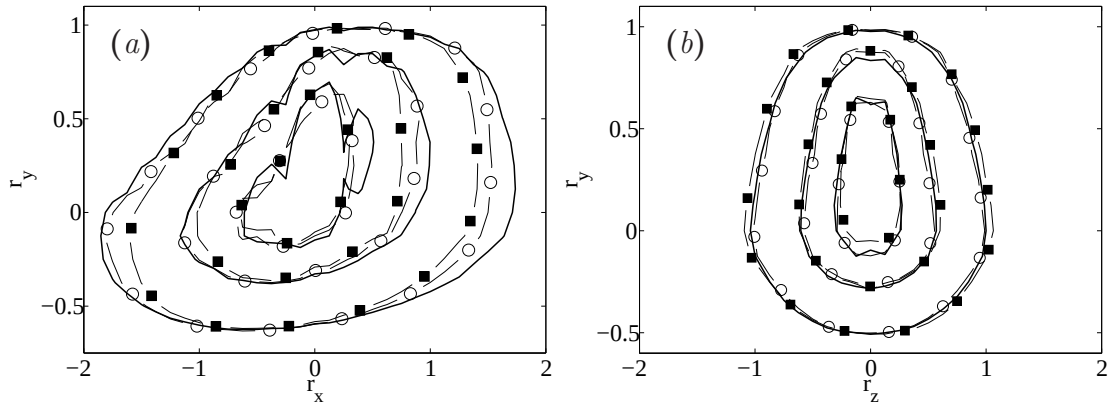

Figure 3.7: P.d.f. of the relative positions of the vortex cores in the circumscribed boxes of the attached clusters with $y^+_{\max} > 100$. The contours contain 20%, 50% and 80% of the data. (*a*), (r_x, r_y) plane. (*b*), (r_z, r_y) plane. ——, **S0**. ○, **R2**. ■, **r3**.

of the points belonging to each cluster, with respect to the center, x_c, z_c, and $y_c = y_{\max}/2$, of its circumscribed box. The scaled position vector in that reference frame is defined as $\mathbf{r} = (\mathbf{x} - \mathbf{x_c})/y_c$. The results show that the p.d.f.s of (r_x, r_y) depend little on the nature of the wall. The slight discrepancy observed for the outer contour at $|r_x| \approx 1$ shows that the attached clusters are slightly more elongated in the smooth-walled channel than in the rough-walled ones. The observed differences disappear when larger clusters are considered, or when the channel is truncated at $y^+_{min} = 100$, which suggests that these differences are caused by the lower mean shear

near the rough walls, rather than by the direct effect of the wall disturbances. This is confirmed because the p.d.f.s of (r_z, r_y) in figure 3.7(b), which are not affected by the shear, agree perfectly for the smooth- and rough-walled cases.

The results presented in figures 3.4 and 3.7 indicate that the sizes and shapes of the attached clusters are not affected by the nature of the wall. We have seen that this is also true for other cluster properties, such as the fraction of Reynolds stresses contained in their circumscribed boxes (see figure 3.5), or their volume density per unit wall distance (see figure 3.6). Particularly interesting is the fact that n_a^+ collapses even for attached cluster laying within the roughness sublayer, with $y_{\max} \lesssim h_R$. All these results suggest that the attached clusters are either generated away from the wall, or that they forget their origin soon after they are born. Note that the two possibilities do not exclude each other. In fact, the lifetimes of the wall-normal velocity reported by del Álamo *et al.* (2006) support the first, while the analysis of the linear evolution of concentrated perturbations in a logarithmic layer presented in chapter 4 supports the second.

3.5. The average velocity field conditioned to the tall attached clusters

We mentioned in §3.1 that the conditionally averaged flow field in the neighborhood of the attached clusters contains a Λ-vortex and a v-ejection. Del Álamo *et al.* (2006) showed that, in smooth channels, it also anchors a conical low-u structure that was too long to be contained within their averaging box, but that was at least 10 times longer than the conditioning cluster. In this section, we analyze the effect of wall roughness on those structures. We have excluded data from **r3**, whose box length is marginally too short for that purpose, even if its conditionally averaged fields are in qualitative agreement with those shown below.

We define the average velocity fluctuations conditioned to a cluster set as

$$\langle \mathbf{u} \rangle (\mathbf{r}) = \sum_i^N \mathbf{u}(\mathbf{x_{c,i}} + y_{c,i}\mathbf{r}) y_{c,i}^3 \Big/ \sum_i^N y_{c,i}^3, \tag{3.4}$$

where the vector $\mathbf{u}$ contains the velocity fluctuations with respect to the mean flow, and the subindex i refers of the i-th cluster of the set. As in del Álamo *et al.* (2006), the weight factor $y_{c,i}^3$ ensures that (3.4) is an unbiased ensemble average, since the probability of sampling a given structure is proportional to its volume. Figure 3.8 shows that the averaged velocity field around the cluster is the same reported by del Álamo *et al.* (2006) over smooth walls at higher Reynolds numbers: a cone-shaped low-momentum region (red) extending mostly downstream of the conditioning object (black), flanked by a pair of counter rotating vortices (green) and high-momentun regions (blue).

A more quantitative comparison is presented in figure 3.9, which shows $\langle \mathbf{u} \rangle (r_z = 0)$ for tall attached clusters, defined here as those with $y_{\max}^+ > 200$. The results from

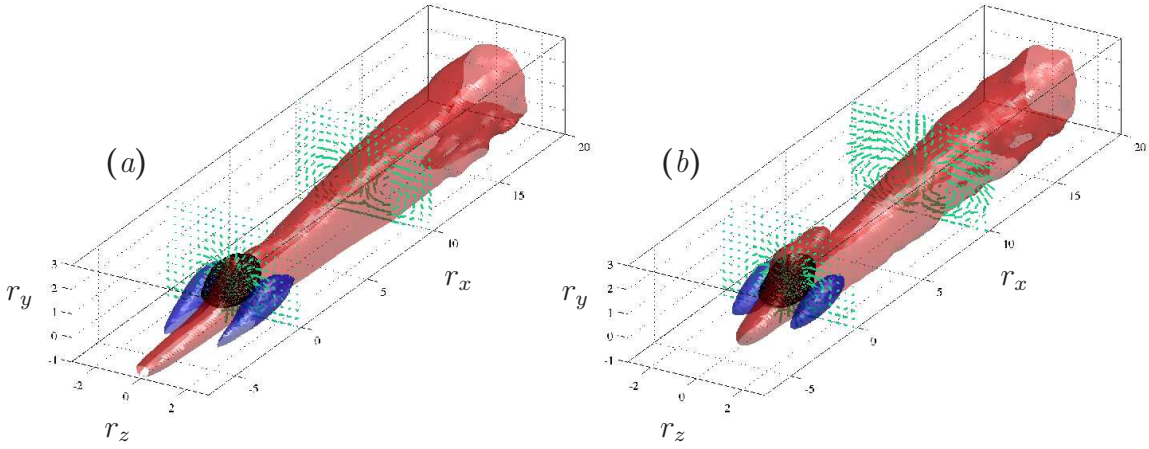

Figure 3.8: Visualization of the $\langle \mathbf{u} \rangle$ for attached clusters with $y^+_{\max} > 200$. The blue surface corresponds to $\langle u \rangle^+ = 0.2$, and the red surface corresponds to $\langle u \rangle^+ = -0.02$. The black surface contains the %60 of the p.d.f. of the relative positions of the points of the cluster. The green arrows show the cross-flow velocities at $r_x = 0$ and $r_x = 10$. (a), **S0**. (b), **R2**.

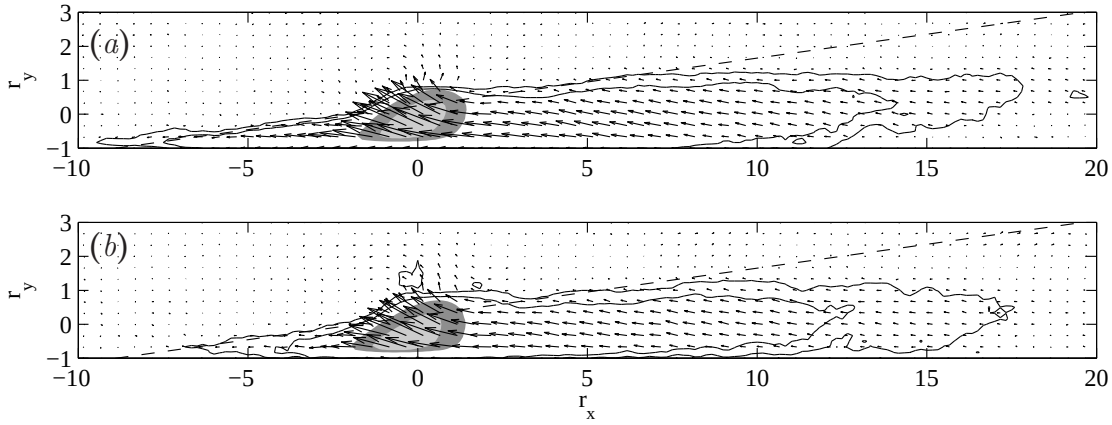

Figure 3.9: Quiver plot of the average fluctuating velocity field $(\langle u \rangle, \langle v \rangle)$ conditioned to the presence of tall attached clusters ($y^+_{\max} > 200$). The data are taken at the plane $r_z = 0$. The contour lines are $\langle u \rangle^+ = -0.05, -0.1$. The shaded contours contain 33 and 66% of the p.d.f. of the position of points inside the conditioning clusters. The dashed lines have a slope of 8°. (a) S, longest arrow $0.93u_\tau$. (b) R1, longest arrow $0.81u_\tau$.

the two cases are nearly identical. The main difference is that the upstream (left) part of the wake is shorter for **R2**, probably due to the lower mean shear of this flow below $y^+ \approx 100$.

The slope of the u-structures in figures 3.9(a) and 3.9(b) is approximately equal to 8° for $-2 < r_x < 5$. It decreases beyond $r_x \approx 5$, and the low-speed cones level off

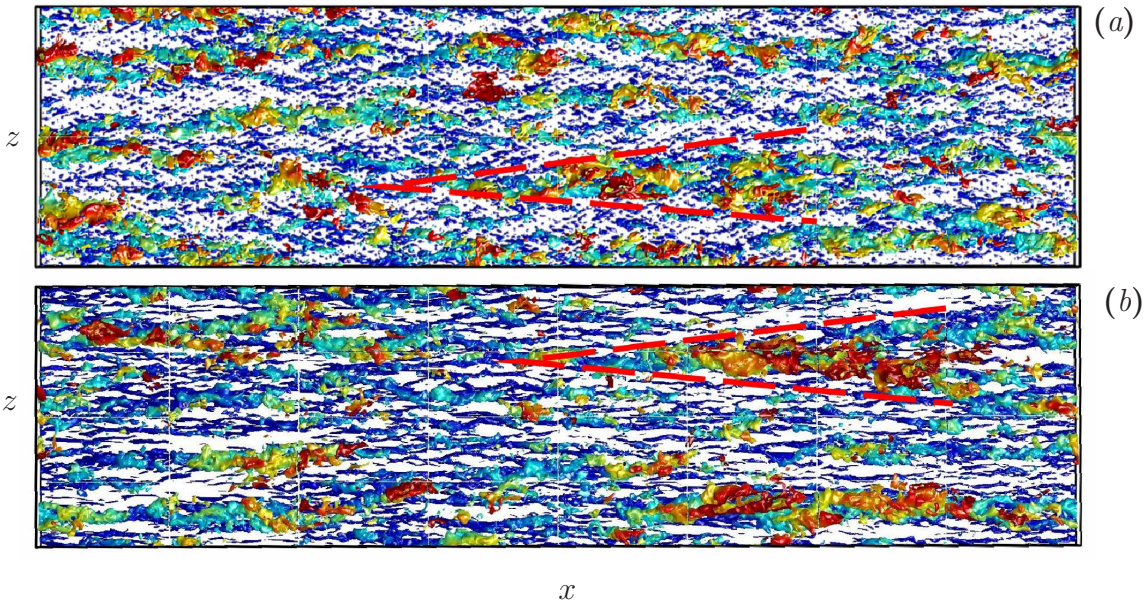

Figure 3.10: Snapshots of the surface $u^+ = -2$ in cases (a) **R2** and (b) **S0**, colored with the wall distance (blue corresponds to the wall, red to the center of the channel). The flow goes from left to right. The size of the plotted boxes is $8\pi h \times 2\pi h \times h$. Two large structures similar to the $u < 0$ cones in figure 3.9 have been manually highlighted in each case, using a red dashed line.

to $r_y \approx 1.5$, and to a width $r_z \approx \pm 1$ for $r_x \gtrsim 8$. We can estimate the size of a typical, tall attached cluster as the mean of the distribution $p_V(y^+_{\min} = 50, y^+_{\max} > 200)$, which is $y^+_{\max} \approx 400$. For this typical cluster, the saturation height and width of the low-u wake in figure 3.9 would be approximately $500\nu/u_\tau$. Figure 3.8 shows that the low-u wake is flanked by high-speed regions, resulting in an spanwise wavelength around $\lambda^+_z \approx 900$.

This saturation is probably due to the limited Reynolds number of our simulations, and it was not observed by del Álamo *et al.* (2006). They used a somewhat higher threshold to identify vortices, a lower near-wall cutoff, and a higher Reynolds number. As a consequence, their cluster population was dominated by smaller objects with respect to the channel height, and the leveling-off was not observed within their averaging box. Note that the coordinates in figure 3.9 are scaled with the size of the conditioning cluster.

In the present case, the leveling-off occurs at cross-stream dimensions of the order of the channel half-width, which agree well with the spectral wavelengths of the global modes identified in chapter 2. The length of the cylindrical sections in figure 3.9 is about $x/h \approx 3-7$, which corresponds to the shorter end of these global modes. Del Álamo *et al.* (2004) had already concluded that the widest modes in the spectra of u were determined by the saturation in the growth of the u-structures when they reach diameters comparable to the channel height.

The connection between figure 3.9 and the global modes is confirmed by instantaneous flow visualizations. Figure 3.10 shows a three-dimensional representation of the surface $u^+ = -2$ in sub-domains of **S0** and **R2**. All the inspected realizations were qualitatively similar to those shown here. In both panels, a large conical structure reminiscent of the averaged velocity fields in figure 3.9 has been highlighted. Although the details of the highlighting are arbitrary in that both structures could be continued into much longer roughly cylindrical streaks, the identification of the initial conical part is in each case essentially unambiguous. The longer downstream structures attached to these regions have lengths of the same order as the simulation box, and recall the very long u-structures already shown in figure 2.9 of chapter 2. Apart from the highlighted cones, a few more examples of cone-like structures of different sizes can be found in the figure. However, it is important to bear in mind that the association of clusters and cones is only strictly true in an averaged sense, as discussed later in §4.4.3. Finally, figure 3.10 clearly illustrates the disruption of the near-wall energy cycle in case **R2**: while the near-wall streaks are clearly visible in case **S0**, they are substituted by a regular array of spots in case **R2**.

It was shown in §2.5.1 that the global modes are very efficient in generating Reynolds stresses, because their wall-normal and spanwise velocity components are highly correlated (see figure 2.10*d*). The same happens with the saturated part of the cones shown in figure 3.9. We define the mean velocity fluctuations inside the cones,

$$U_w(r_x) = A_\Omega^{-1} \int_{\Omega(r_x)} \langle u \rangle dA, \qquad \text{and} \qquad V_w(r_x) = A_\Omega^{-1} \int_{\Omega(r_x)} \langle v \rangle dA, \tag{3.5}$$

where $\Omega(r_x)$ is the region where $\langle u \rangle^+ < -0.05$ at each streamwise location. These velocities are shown in figure 3.11(*a*) for clusters with $y^+_{\max} > 200$. Both U_w^+ and V_w^+ peak at the center of the cluster but the mean fluctuating velocities from case **R2** are somewhat weaker than those from case **S0**. This agrees with the results shown in figure 2.10(*b*) in chapter 2, where the global modes in **S0** were shown to be slightly stronger than in **R2**.

Figure 3.11(*b*) shows that the ratio U_w/V_w agrees for **S0** and **R2**, showing a reasonable plateau in the range $5 < r_x < 15$. Note that U_w/V_w is a measure of the efficiency of v in creating u-perturbations from the mean velocity profile, and the level of the plateau is quite higher: for instance, the overall ratio of the r.m.s. turbulent intensity in the outer layer is $(\overline{u^2})/(\overline{v^2}) \approx 1.5 - 2$ (the overline denotes time and wall-parallel averaging). The level in figure 3.11(*b*) is of the same order as the structure parameter for the Reynolds stresses $-(\overline{u^2})^{1/2}/(\overline{uv})^{1/2} \approx 4.5 - 5$, which measures only the part of v correlated with u. It is also of the order of the ratio between the energy spectrum of the streamwise velocity and the Reynolds-stress cospectrum, which is $-\phi_{uu}/\phi_{uv} \approx 3 - 7$ for wavelengths of the order of $5h \times h$, outside the buffer layer. These figures are consistent with the interpretation of the saturated parts of the structures in figure 3.9 as global modes. Other values of the threshold in the definition of $\Omega(r_x)$, and any reasonable range of sizes for the attached clusters with $y^+_{\max} > 100$, lead to the same plateau as in figure 3.11(*b*).

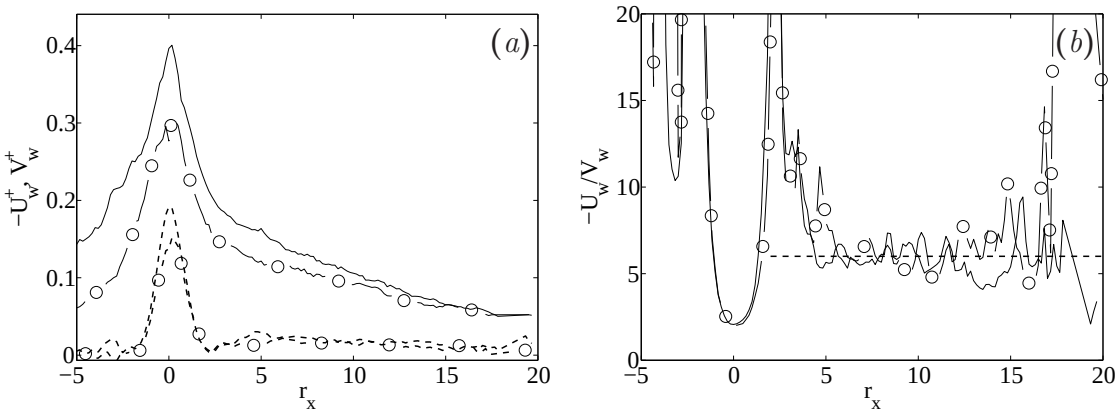

Figure 3.11: Mean velocity fluctuations inside the cone, U_w and V_w (see 3.5), for attached clusters with $y^+_{\max} > 200$. (a) Velocities in wall units, solid lines correspond to $-U_w^+$ and dashed lines corresponds to V_w^+. (b) Ratio $-U_w/V_w$, the horizontal line is $-U_w/V_w = 6$. ——, **S0**. ○, **R2**.

3.6. Conclusions

In the present chapter we have investigated the properties of the vortex clusters found in turbulent channels with rough walls at moderate Reynolds numbers. As in the smooth-walled case, they separate into wall-attached and wall-detached families. We have paid especial attention to those attached clusters that reach above the roughness sublayer and into the outer region of the flow. They play an important role on the dynamics of the turbulent outer layer (del Álamo *et al.*, 2006), and have many characteristics in common with the constitutive elements of a number of models that represent that part of the flow by hierarchies of vortex loops emanating from the wall (Perry & Chong, 1982; Perry & Marusic, 1995).

Our results indicate that the distribution of sizes and shapes of the attached clusters are virtually the same in the smooth- and in the rough-walled cases. The sizes of the clusters are proportional to their heights, indicating a self-similar distribution of objects, consistent with the attached-eddy hypothesis of (Townsend, 1976, pages 150–162). The density of attached clusters in the outer region is not modified by the wall-disturbances either. This result holds even if the relative volume occupied by the identified vortices is larger in the roughness sublayer of the rough-walled cases than in the near-wall region of the smooth-walled case.

The sizes of the attached clusters correspond to the energy containing scales of the wall-normal velocity spectrum, consistently with the interpretation of del Álamo *et al.* (2006) that in an averaged sense, the clusters are markers of wall-normal velocity bursts. We have also shown that the attached clusters are "superactive", meaning that the Reynolds stresses averaged in the boxes containing the attached clusters are larger than the average. This confirms that the attached clusters are dynamically important structures in rough-walled flows, as they are in smooth-

walled flows (del Álamo *et al.*, 2006).

As in the smooth-walled cases, the attached clusters over disturbed walls are associated with cones of negative streamwise velocity fluctuations that extend downstream of the position of the cluster. The only appreciable effect of the wall in these cones is found in their upstream part, which is shorter in the rough-walled cases than in the smooth-walled ones. That part of the cones is immersed in the roughness sublayer, and probably the shortening of the streamwise velocity structure is connected with the lower mean shear of the rough-walled cases in this region.

These observations, together with the lifetimes obtained by del Álamo *et al.* (2006) for the structures in channels at higher Re_τ, suggest that either the attached clusters are generated at all heights, or that they quickly become self-similar and forget about their origin. The results presented here help to reconcile the attached-eddy models with Townsend's hypothesis that the outer layer is independent of the wall details, in agreement with the results presented in chapter 2.

Finally, we have also shown that the cones level off when their widths and heights become of the order of the channel half-height. These parts of the cones are the global modes identified in chapter 2, and the analysis of their mean streamwise and wall-normal velocity fluctuations show that their streamwise and wall-normal velocity components are highly correlated, in agreement with the results of §2.5.1 and by del Álamo & Jiménez (2003).

Chapter 4

Linear analysis of self-similar structures in the turbulent logarithmic region

4.1. Introduction

In the previous chapters we have seen that there is a clear connection between the vortical structures populating the logarithmic and outer regions, and the very large streamwise velocity structures reported in many experimental and numerical works, like Hites (1997), Jiménez (1998), Kim & Adrian (1999), del Álamo *et al.* (2004) and Hutchins *et al.* (2007). As discussed in §3.1, there are in principle two different structural models that attempt to explain that connection. Both of them are, for the moment, incomplete.

The most extended one is the hairpin packet paradigm, originally proposed by Adrian *et al.* (2000), and based on the horseshoe vortex originally proposed by Theodorsen (1952). According to this model, several hairpin vortices appear organized in packets, growing linearly from the wall into the outer region. The growth of the packets involves several mechanisms, including self-induction, autogeneration and mergers with other packets, as discussed in Tomkins & Adrian (2003). The low-momentum regions are caused by the cooperatively work of all the hairpins within the packet.

However, the origin and evolution of these hairpin packets remains elusive, specially regarding how they move away from the wall. Zhou *et al.* (1999) described an autogeneration mechanism whereby a hairpin packet could be created from an initial lambda vortex in a laminar channel with a turbulent mean profile. They however neglected the background fluctuations of real turbulent flows. We will see in this chapter that this effect might be able to alter significantly the process, shortening the lifetimes and lowering the intensities of the vortices. Moreover, the hairpins in the laminar simulations move only moderately away from the walls.

A less organized model is proposed by del Álamo *et al.* (2006). The characteristic vortical structure in this case is a vortex cluster that shares many of the properties of the large-scale eddies of the hairpin model. However, the clusters are bags of vortices

in which individual hairpins are difficult to identify. In average, the attached clusters are associated with wall-normal velocity bursts, where the local dissipation is higher than the average. Chapter 3 shows that these clusters/bursts are also present over rough walls. The estimation of their lifetimes over smooth walls (del Álamo *et al.*, 2006), together with the results of chapter 3, suggest that they are generated at all heights, or alternatively that the clusters form at the wall, but that they quickly forget their origin and reach some local equilibrium with the outer layer. Either way, the importance of the wall is diminished.

However, it is not clear in this model whether the bursts align with each other to create the ramps, or whether the ramps should be considered as the original structures that determine where the bursts form.

It is important to note that, from the kinematic point of view, the model proposed by Adrian *et al.* (2000) (hairpin packet) and the one proposed by del Álamo *et al.* (2006) (cluster) are statistically equivalent, and that they are both consistent with the velocity statistics and spectra reported in wall-bounded turbulent flows. For example, Marusic (2001) successfully used the hairpin packet model to reproduce the second-order statistics of a turbulent boundary layer, while del Álamo *et al.* (2006) showed that the educed clusters and wakes were representative enough of the flow as a whole to explain the global statistics. Beyond that, the two models are not dynamically equivalent. First, the hairpin vortex is thought to be the cause of the ejection, while the cluster is the effect of the burst. Second, while the hairpin packet model is based on structures that grow from the wall, the observations suggest that the clusters are generated at all heights. Also, the hairpin packets are long-lived structures with lifetimes much longer than their characteristic turn-over time (Zhou *et al.*, 1999), while the lifetimes of the bursts are much shorter. Finally, while the clusters are intrinsically turbulent, complex objects, the hairpin is a laminar, simple structure, which seems unlikely to extend to an important fraction of the logarithmic region in a high-Reynolds-number wall-bounded turbulent flow.

The aim of the analysis presented in this chapter is to describe the evolution of a wall-normal burst in a turbulent environment, investigating how it creates the elongated low-momentum regions identified in the logarithmic and outer regions. The interaction of the wall-normal velocity with the mean shear has long been recognized to play an important role in the generation of large structures in the streamwise velocity (Robinson, 1991*a*). Indeed, del Álamo *et al.* (2004) and del Álamo *et al.* (2006) proposed that the bursts interact linearly with the mean velocity profile and with the background turbulence to generate the very long wakes, or streaks, of low streamwise velocity. This interaction was studied by del Álamo & Jiménez (2006) through a temporal transient growth analysis of the Fourier transform of the linearized Orr–Sommerfeld–Squires equations, showing good agreement between the modes with maximum transient growth and the dominant scales of the energy spectrum. We study here the initial value problem, analyzing the evolution in space and time of an initially localized disturbance, given by an idealized version of the average burst reported by del Álamo *et al.* (2006). The results presented in this chapter

complete the model proposed by del Álamo *et al.* (2006), offering new explanations for the origin of the bursts, and highlighting the weak points of the hairpin packet paradigm.

The present analysis shares some features with the published works describing the dynamics of hairpin vortices, both numerically (Singer & Joslin, 1994; Zhou *et al.*, 1999; Suponitsky *et al.*, 2005) and experimentally (Acarlar & Smith, 1987*a*,*b*; Haidari & Smith, 1994). However, while the previous works describe the evolution of individual hairpin-like vortices in a laminar flow, in the present work we deal with the evolution of an averaged eddy in a turbulent environment. The chaotic packet evolution described by Adrian & Liu (2002) is neither comparable with the present approach. They introduced a 5% of white noise in their initial condition to simulate the background turbulence. However, this noise was quickly removed by the viscosity, with the subsequent laminar evolution of the (noisy) hairpin.

The chapter is organized as follows. Section 4.2 presents the linearized equations in the limit of elongated structures in a turbulent environment, which are solved using the numerical method described in §4.3. The main results for the linear model are presented in §4.4, while the possible origin of the bursts is discussed in section 4.5. Finally, conclusions are presented in §4.6.

4.2. The linearized equations for elongated turbulent structures

The linearized equations that describe the evolution of organized turbulent structures in an incompressible parallel flow are

$$\partial_t \mathbf{u} + U\partial_x \mathbf{u} + (v\partial_y U, 0, 0) = -\rho^{-1}\nabla p + \left[\nu_T(\partial_{xx} + \partial_{zz}) + \partial_y(\nu_T\partial_y)\right]\mathbf{u}, \qquad (4.1)$$

and the continuity equation, where $\mathbf{x} = (x, y, z)$ are the streamwise, wall-normal and spanwise coordinates, $\mathbf{u} = (u, v, w)$ is the corresponding velocity perturbation vector, $U(y)$ is the mean velocity, p is the rapid pressure (Kim, 1999), and ρ is the constant density of the fluid. We have replaced the molecular viscosity ν with a turbulent eddy viscosity $\nu_T(y)$, to incorporate the dissipative effect of the incoherent background turbulence. Its magnitude is chosen, in principle, as that needed to maintain the mean velocity profile, although some corrections will be introduced later. This approximation, introduced by Reynolds & Hussain (1972), was successfully used by Jiménez *et al.* (2001*b*) and by del Álamo & Jiménez (2006) to analyze the temporal stability of the large scales in turbulent channels.

The general idea behind equation (4.1) is that the dynamics of the large scales in wall turbulence are well described by the rapid-distortion theory (RDT), which assumes that the lifetimes of the structures are longer than the shear time, so that the mean shear linearly distorts them before they can evolve (Jiménez, 1998). We can show that this situation applies for the attached clusters/bursts. Consider an attached eddy with height $2y$ whose characteristic velocity is the friction velocity

u_τ. Its turn-over time is $O(2y/u_\tau)$, and its viscous time is $O(y^2/\nu)$. Moreover, if y is within the logarithmic layer, the shear time at the center of the eddy is $(\partial_y U)^{-1} \sim O(\kappa y/u_\tau)$, much shorter than the viscous time, and about 5 times shorter than the eddy turn-over time for the typical values of the Kármán constant, $\kappa \approx 0.4$.

Therefore, we can assume that the dynamics of an attached eddy are approximately driven by the mean shear, and that the main role of its non-linear interactions with itself and with the background turbulence is to limit its growth. This effect is modeled here with the coarse eddy-viscosity approximation in (4.1), but it could also be implemented by explicitly limiting the lifetime of the structures, as in Butler & Farrel (1993). However, the latter approach requires a previous knowledge of the temporal evolution of the solution, while the former only requires the knowledge of the mean velocity profile.

We now proceed to the analysis of the orders of magnitude of the terms in (4.1). We will consider velocity structures that are attached to the wall, meaning that their size is of the order of their wall distance. We will also assume that the wall-normal and spanwise sizes of these structures are of the same order ($l_y \sim l_z$), from where continuity yields characteristic velocities $v_c \sim w_c$. The analysis of the terms of the y-component of (4.1) shows that

$$\frac{l_x}{l_y} \sim \frac{U_e}{u_\tau}, \quad t_c \sim \frac{l_y}{u_\tau} \sim \frac{y}{u_\tau}, \quad \text{and} \quad p_c \sim \rho u_\tau v_c, \tag{4.2}$$

where l_x is the length scale in the streamwise direction, t_c and p_c are the characteristic time scale and rapid pressure fluctuations, and U_e is the mean velocity difference between the top and the bottom of the eddy. If the eddy is tall enough to reach the logarithmic layer ($l_y^+ > 100$), we have that $U_e/u_\tau \gtrsim 10$ and hence $l_x/l_y \gtrsim 10 \gg 1$. Even if the eddy lies within the buffer layer, we still have $l_x/l_y \sim U_e/u_\tau \gtrsim 5$. Therefore, we will consider $u_\tau/U_e \sim l_y/l_x$ as a small parameter, and we will simplify equation (4.1) accordingly. The dissipation coming from streamwise derivatives is $O(l_y/l_x)^2$ compared to the leading-order terms in (4.1), and is neglected. The $\partial_x p$ term in the streamwise component of (4.1) can also be neglected because it is $O(l_y/l_x)$ relative to the remaining terms. This simplification implies that the pressure can be obtained by solving a Laplace equation only in the cross-flow.

After these simplifications, we can write the following two equations for the perturbations of the streamwise velocity u, and vorticity ω_x,

$$\partial_t u + U\partial_x u + v\partial_y U = \left[\nu_T \partial_{zz} + \partial_y(\nu_T \partial_y)\right] u, \tag{4.3}$$

$$\partial_t \omega_x + U\partial_x \omega_x + \partial_x w\, \partial_y U = \left[\nu_T \partial_{zz} + \partial_y(\nu_T \partial_y)\right] \omega_x + \left[\nu_T' \partial_{zz} + \partial_y(\nu_T' \partial_y)\right] w, \tag{4.4}$$

where $\nu_T'(y) = \partial_y \nu_T(y)$. These two equations are completed with the continuity equation

$$\partial_x u + \partial_y v + \partial_z w = 0, \tag{4.5}$$

where in principle all the terms may be of the same order if the streamwise velocity perturbation becomes much larger than the characteristic cross-flow perturbation.

4.2.1. Self-similar form of the linearized N-S equations

The Navier–Stokes equations only become invariant to scaling transformations in the limit of infinite Reynolds number, and self-similarity is normally restricted to that inviscid case. However, the turbulent eddy viscosity model used for the logarithmic region does not introduce any fixed length-scale, opening the possibility of invariance to scale transformations. Here we derive the self-similar form for the linearized equations (4.3) and (4.4), but the introduction of the non-linear advection terms ($u\partial_x$, $v\partial_y$ and $w\partial_z$) results in similar expressions.

We consider an idealized logarithmic layer with $\partial_y U = u_\tau/(\kappa y)$ and $\nu_T = \kappa u_\tau y$. In that case, (4.3) and (4.4) can be expressed in self-similar form using the velocity $\tilde{\mathbf{u}} = \mathbf{u}/u_0$, the rescaled streamwise vorticity $\tilde{\omega}_x = t\omega_x u_\tau/u_0$, and the coordinates

$$\chi = \frac{x - U(y_0)t}{u_\tau t} - \frac{1}{\kappa}\left[\log\left(\frac{u_\tau t}{y_0}\right) - 1\right], \quad \eta = \frac{y}{u_\tau t}, \quad \text{and} \quad \zeta = \frac{z}{u_\tau t}. \tag{4.6}$$

Here y_0 is an arbitrary wall distance that fixes the origin of the new streamwise coordinate, and the free scale factor u_0 appears due to the linearity of the equations. The self-similar equations for $\tilde{u}$ and $\tilde{\omega}_x$ are

$$-(\chi\partial_\chi + \eta\partial_\eta + \zeta\partial_\zeta)\tilde{u} + \kappa^{-1}\left(\log(\eta)\partial_\chi\tilde{u} + \eta^{-1}\tilde{v}\right) = \kappa\left(\partial_\eta(\eta\partial_\eta) + \partial_\zeta(\eta\partial_\zeta)\right)\tilde{u}, \tag{4.7}$$

$$\begin{aligned} -(\chi\partial_\chi + \eta\partial_\eta + \zeta\partial_\zeta)\tilde{\omega}_x + \kappa^{-1}\left(\log(\eta)\partial_\chi\tilde{\omega}_x + \eta^{-1}\partial_\chi\tilde{w}\right) = \\ \kappa\left(\partial_\eta(\eta\partial_\eta) + \partial_\zeta(\eta\partial_\zeta)\right)\tilde{\omega}_x + \kappa\left(\partial_{\eta\eta} + \partial_{\zeta\zeta}\right)\tilde{w}. \end{aligned} \tag{4.8}$$

These equations suggest that a typical burst emanating from a wall distance y within the logarithmic layer spreads linearly with time in the cross-stream directions, and as $t\log t$ in the streamwise direction. The linear spreading in the cross-stream directions is caused by the turbulent eddy viscosity, and is reflected in the scaling of η and ζ in (4.6). The faster streamwise spreading comes from the effect of the mean shear, and can be deduced from the time dependence of χ in (4.6). While decaying and spreading, the burst stirs the mean profile and generates a streamwise velocity streak which is larger and lives longer than the original burst. This process is invariant to scale transformations, and it may therefore occur at all wall distances in the logarithmic layer, provided that there is some mechanism that creates the bursts. These ideas should not be restricted to the limit of elongated structures, because the set of variables given in (4.6) can also be used to express (4.1) in self-similar form. In fact, del Álamo *et al.* (2004), Hoyas & Jiménez (2006) and del Álamo *et al.* (2006) provided evidence for self-similar kinematics in a wide range of scales within the logarithmic region of turbulent channels up to $Re_\tau = 2003$.

The arguments presented above provide some theoretical support for models based on self-similar hierarchies of eddies, such as the attached eddy theory of Townsend (1976), or the hairpin forest model of Perry & Chong (1982). Those models are essentially based on two assumptions: linearity (to use a superposition

of elementary solutions) and self-similarity (to relate these elementary solutions to each other by a scale factor). We have shown at the beginning of §4.2 that the linear approximation is appropriate for the structures of the logarithmic region of wall-bounded flows. Equations (4.7)-(4.8) suggest that self-similarity is compatible with the averaged structures of the logarithmic region.

From now on, we will put aside the self-similar formulation presented here, to move to the numerical resolution of the linearized Navier–Stokes equations (4.3)-(4.4) in a logarithmic layer with very large Re_τ.

4.3. Numerical solution

In the present section we describe the numerical scheme developed to solve (4.3)-(4.5) for the evolution of a wall-attached burst in the logarithmic region of a plane channel flow with a virtually infinite Reynolds number $Re_\tau = u_\tau h/\nu = 10^9$. The mean velocity and eddy viscosity profiles are prescribed using a modification of the Cess's (1958) formula for turbulent channels,

$$\frac{\nu_T}{\nu} = \frac{\beta}{2}\left\{1 + \frac{K^2 Re_\tau^2}{9}\left[2Y - Y^2\right]^2\left[3 - 4Y + 2Y^2\right]^2\left[1 - e^{\left(\frac{-YRe_\tau}{A}\right)}\right]^2\right\}^{1/2} + \frac{2-\beta}{2}, \tag{4.9}$$

where $Y = y/h$, and the molecular viscosity ν is already included. The parameter $\beta \in [0, 1]$ controls the fraction of the Reynolds stresses that is assumed to be generated by the background turbulence. The rest is assumed to come from the linear superposition of eddies with sizes of the same order of magnitude as the structures being computed. Note that this does not imply that a single burst has to generate the full missing fraction $(1 - \beta)$ of the Reynolds stress. The limit $\beta = 1$ recovers the original formula proposed by Cess, while $\beta = 0$ would imply that $\nu_T = \nu$, and that the background turbulence is completely neglected. The mean velocity profile is always obtained from the full ν_T ($\beta = 1$), assuming that the total shear stress is independent of y, as in the limit of $Re_\tau \to \infty$. It then follows that $\partial_y U = {u_\tau}^2/\nu_T(\beta = 1)$. The constants A and K have been adjusted by a least square fit to the mean velocity profile of the turbulent channel simulated by Hoyas & Jiménez (2006), with $Re_\tau = 2003$.

The spatial discretization uses Fourier series in z and the same fourth-order, spectral-like, compact finite differences presented in chapter 2 for the wall-normal direction, y. Since the solution is smooth in the streamwise direction, we have employed second-order finite differences with a staggered grid in this direction. The time integration is performed with a third-order, semi-implicit Runge-Kutta scheme of the family derived by Spalart *et al.* (1991). The reference system is advected at the constant velocity $U(y_0)$, where y_0 is the position of the center of the initial wall-attached burst.

From the self-similar analysis presented in §4.2.1, we can expect the solution of (4.3)-(4.5) to spread in space as time advances. For this reason, we use large

domains in the linear simulations, with $L_y \times L_z/2 = 60y_0 \times 23y_0$. We use a stretched mesh in the wall normal direction, to ensure that the wall-normal velocity gradient is well captured by the compact finite differences. The resolution in z is fixed in all the cases to $\Delta z = y_0/6$, so that the burst is initially described by 10 points.

Note that the spreading of the initial burst in the streamwise direction will be higher than in y or z, since it is driven by the mean velocity gradient. Because of this, the streamwise length of the computational box is increased in time following the law $L_x = 35y_0 + 20u_\tau t$, evaluated at discrete increments of $\Delta t = 5y_0/u_\tau$. The number of points in x is kept constant when the length of the box is increased. The expanded $\mathbf{u}$ and ω_x fields are obtained by linear interpolation, padding with zeros the new part of the domain. Since L_x is increased before the disturbance reaches the x-boundaries, this procedure ensures that the solution is not affected by the boundary conditions at the inlet and at the outlet, while avoiding the numerical cost of tracking the whole evolution of the initial burst in a large domain with a high resolution.

We use the standard non-slip and impermeability conditions for the velocity at the wall, and $\mathbf{u} = \omega_x = 0$ and $\partial_x \mathbf{u} = \partial_x \omega_x = 0$ respectively at the inlet and at the outlet of the domain. Since the latter is necessarily truncated in the wall-normal direction, we replace the boundary conditions at $y \to \infty$ with

$$\partial_y \hat{g}(L_y) = -k_z \hat{g}(L_y), \tag{4.10}$$

where $\hat{g}$ stands for the spanwise Fourier mode of either u, v, w or ω_x, and k_z is the corresponding spanwise wavenumber. This boundary condition is obtained from the asymptotic form of (4.3)-(4.4) in the limit $\nu_T \to \infty$. In that case, the remaining equation for $\mathbf{u}$ and ω_x is a homogeneous Laplace equation, whose solutions are $\hat{g} \sim e^{\pm k_z y}$. Discarding the growing exponential, we obtain (4.10).

Finally, the initial condition considered here is a wall-normal burst associated to a compact pair of counter rotating vortices. Its analytical expression is

$$\psi = \frac{u_0 z y^2}{y_0^2} \exp\left(-\frac{x^2}{4y_0^2} - \frac{y^2}{y_0^2} - \frac{z^2}{y_0^2}\right), \tag{4.11}$$

where $\mathbf{u} = (0, \psi_z, -\psi_y)$. This flow pattern resembles the characteristic wall-attached eddy found by Moin & Moser (1989) in the proper orthogonal decomposition (POD) of the velocity field from an $Re_\tau = 180$ turbulent channel. It is also similar to the average transverse velocity field conditioned to the presence of wall-attached vortex clusters found by del Álamo *et al.* (2006) in the logarithmic layer of turbulent channels up to $Re_\tau = 1900$. A similar velocity structure was used in Zhou *et al.* (1999) as initial condition, although in that case the structure had been extracted from the application of the linear stochastic estimation method to the $Re_\tau = 180$ turbulent channel of Kim *et al.* (1987). In the present case, the length and width of the initial burst in (4.11) are proportional to its wall distance, y_0. We have chosen the coefficients of (4.11) so that the streamwise and spanwise aspect ratios of the initial burst, measured as the region where $\omega_x < 0.1 \max(|\omega_x|)$, are approximately equal to

3 and 1.5, in agreement with the experimental values reported by del Álamo *et al.* (2006). Finally, due to the linearity of equations (4.3) and (4.4), the free velocity-scale factor u_0 appears explicitly in the expression of the initial condition, but it can be discounted.

4.4. Results from the linear model

We present here results from our linear model for initial bursts at $y_0^+ = 25$, 50, 100, 200, 400 for a virtually infinite Reynolds number ($Re_\tau = 10^9$) and different values of β in (4.9). Since the problem is roughly self-similar, the resolution in the wall-parallel planes has been kept proportional to y_0, using $N_x = N_z = 192$ grid points to discretize the numerical domain. The grid resolution and stretching in the wall-normal direction has been kept constant in wall units, to guarantee the proper resolution of the wall-normal derivatives in the buffer region. The number of points used in the y-direction is $N_y = 94$, 130, 185, 274, 423 for the corresponding y_0^+ given at the beginning of the paragraph. The results of the linear simulation are relatively independent of the initial position, shape and orientation of the vortices in (4.11), consistent with the self-similar evolution of the burst described below.

4.4.1. Energy growth and lifetimes

The evolution of the initial condition (4.11) can be characterized by the streamwise and cross-flow kinetic energies,

$$Q_u(t) = \frac{1}{2}\int_V u^2 dV \qquad \text{and} \qquad Q_{vw}(t) = \frac{1}{2}\int_V (v^2 + w^2) dV, \tag{4.12}$$

where V is the volume of the computational domain. These energies are shown in figure 4.1(a), normalized with the total initial energy $Q_0 = Q_{vw}(0)$ and computed for $\beta = 1$. Consistent with the analysis in the previous section, the kinetic energies of bursts emanating from different wall distances only depend on $\tau = tu_\tau/y_0$ for y_0 in the logarithmic region. Initially, all the energy of the bursts is contained in v and w, but these cross-flow disturbances decay more than one order of magnitude during their first turn-over time, $\tau \approx 1$. During this process they generate streamwise velocity fluctuations through the lift-up term $v\,\partial_y U$ in (4.3). After the maximum of Q_u, both energies decrease, although the rate of decay of Q_u is slower. Note that when the burst has decayed to the level of $Q_{vw}/Q_0 \approx 10^{-2}$ ($\tau \approx 2$), between $10 - 30\%$ of the initial energy still remains in the u-structure.

This behavior is similar to the transient growth of the Orr–Sommerfeld–Squires modes in channels with turbulent profiles and eddy viscosities, which was computed by del Álamo & Jiménez (2006). However, the energy amplifications in figure 4.1(a) are smaller than those reported by del Álamo & Jiménez (2006) for logarithmic-layer modes, because the initial condition employed here (4.11) excites all the eigenfunctions of the Orr–Sommerfeld–Squires operator, instead of only the most amplified ones.

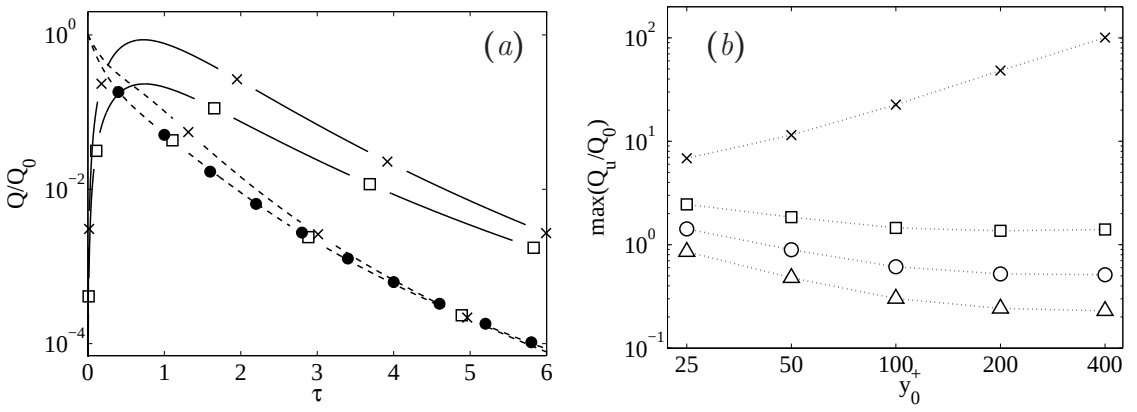

Figure 4.1: (a) Evolution of the streamwise energy Q_u/Q_0 (——) and the cross-flow energy Q_{vw}/Q_0 (− − −) for $\beta = 1.0$. $-\times-$, $y_0^+ = 25$; $-\square-$, $y_0^+ = 400$. The closed circles ($\bullet$) correspond to $Q_{vw}/Q_0 = 2700(3+\tau)^{-7.85}$. ($b$) Maximum of the streamwise energy, $\max(Q_u/Q_0)$, as a function of y_0^+ and β. Note that the abscissa is in logarithmic scale. $\times$, $\beta = 0$; $\square$, 0.3; $\circ$, 0.6; $\triangle$, 1.0.

Figure 4.1(a) only shows cases with $y_0^+ = 25$ and 400, but the evolution of Q_{vw}/Q_0 for $y_0^+ > 50$ closely matches the case with $y_0^+ = 400$ shown in the figure. The evolution of Q_u/Q_0 is qualitatively the same for all y_0, although the peak values of Q_u, shown in figure 4.1(b), depend on the initial size of the burst. For $\beta > 0$, the maximal amplifications decrease with the size of the burst, since $\partial_y U$ is higher in the buffer layer than in the logarithmic region. Once $y_0^+ \gtrsim 100$ the bursts are essentially embedded in the logarithmic region, and their peak streamwise energies no longer depend on their sizes.

It is important to assess the influence of β on the velocity perturbations. This parameter represents the fraction of the Reynolds stress that is modeled by the eddy viscosity, as explained above. Figure 4.1(b) shows that $\max(Q_u/Q_0)$ increases by more than one order of magnitude when β varies from 1.0 ($\triangle$) to 0 ($\times$), regardless of y_0^+. Also, while $\beta > 0$ smaller bursts have higher $\max(Q_u/Q_0)$, but for $\beta = 0$ the peak values are roughly proportional to the size of the burst. These changes have to be related to the time needed by ν_T to dissipate the initial burst, since the parameter β does not appear explicitly in the lift-up term $v\partial_y U$. Figure 4.2(a) shows the time needed to reach the peak of Q_u/Q_0, for different values of β and y_0. It is clear from the figure that $T_{\max} \propto y_0/u_\tau$ for $\beta > 0$, while $T_{\max} \propto y_0^2/\nu$ when the molecular viscosity is used ($\beta = 0$). The transition between the turbulent ($\beta > 0$) and the laminar ($\beta = 0$) behavior is rather sharp, and even for the case $\beta = 0.3$, the increase in $T_{\max} u_\tau/y_0$ when y_0^+ varies from 25 to 400 is only a factor of 1.4.

The change on the time scale of the burst is related to the introduction of a fixed length scale by the molecular viscosity, breaking the self-similarity of the governing equations (see §4.2.1). Also, the molecular viscosity is much weaker than the turbulent eddy viscosity, and a burst that would be quickly dissipated in short times

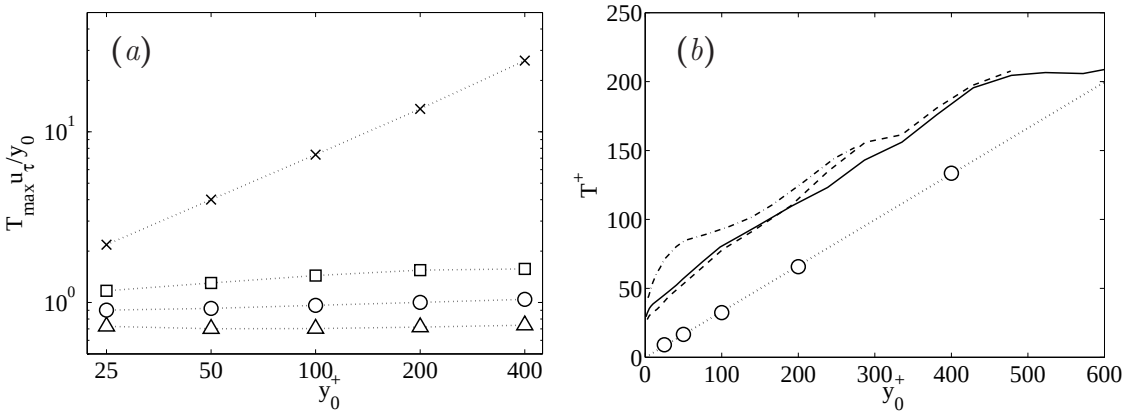

Figure 4.2: (a) Scaling of the time to maximum growth, $T_{\max}$. The abscissa of the plot is in a logarithmic scale. $\times$, $\beta = 0$; $\square$, 0.3; $\circ$, 0.6; $\triangle$, 1.0. (b) Integral times for the linear model and for turbulent channel flows. The circles correspond to T_l^+ for $\beta = 0.6$. The lines correspond to T_v^+ for the turbulent channels of del Álamo *et al.* (2004), with the correspondence $y \sim 2y_0$. —·—, $Re_\tau = 550$. − − −, 950. ——, 1880. The dotted straight line has $dT^+/dy_0^+ = 0.35$.

by the small scale turbulence survives in the laminar flow for much longer times.

In order to compare the evolution of the burst of the liner model with those present in real turbulent flows, we analyze the integral times of the wall-normal velocity component. For the linear model we have

$$T_l = \frac{1}{Q_v(0)} \int_0^\infty Q_v(t) dt, \tag{4.13}$$

where Q_v is analogous to the Q_u defined in (4.12). For the DNS channels we use the definition of integral time given by Wills (1964),

$$T_v(y) = \frac{\iint \phi_{vv}(k_x, k_z, -ck_x, y) dk_x dk_z}{\iiint \phi_{vv}(k_x, k_z, f, y) dk_x dk_z df}, \tag{4.14}$$

where $\phi_{vv}(k_x, k_z, f, y)$ is the wavenumber-frequency spectrum of the wall-normal velocity component, k_x and k_z are the streamwise and spanwise wavenumbers, f is the frequency and c is the phase velocity of each wave component. The integrals in (4.14) are performed over the spectral bands $y/2 < \lambda_x < 2h$ and $y/4 < \lambda_z < h$, which correspond to the range of sizes of the wall-normal bursts. We have seen in the previous chapter that the density of those bursts decreases faster than y^{-3}, so that a given wall-distance y, ϕ_{vv} is dominated by the contribution of eddies of height y. Since the initial conditions of the linear simulations have a height approximately equal to $2y_0$, we use the correspondence $y \sim 2y_0$ to compare $T_v(y)$ with $T_l(y_0)$.

These integral times are presented in figure 4.2(b), for turbulent channels with $Re_\tau = 550 - 1880$, and for the linear case with $\beta = 0.6$. We have selected that case

because it is the one that matches best the slope of the turbulent cases, $dT^+/dy_0^+ = 0.35$. Guala *et al.* (2006) and Balakumar & Adrian (2007) showed that the fraction of Reynolds stresses contained in structures with $l_x/l_y \lesssim 5$ in the logarithmic layer of turbulent pipes, boundary layers and channels is about 30%. The selected value $\beta = 0.6$ is reasonably close to that fraction, taking into account the crudeness of the eddy viscosity approximation. Both T_l^+ and T_v^+ grow linearly with time, and the differences in the origin of the curves are due to the different initial transients of real turbulent bursts and those in the linear model. Although not included in figure 4.2(b), the integral times of the linear case for other values of $\beta > 0$ are also proportional to y_0^+, although with different slopes. For $\beta = 0$ we obtain $T_l^+ \propto (y^+)^2$, in agreement with figure 4.2(a).

The differences between the evolution of disturbances in laminar ($\beta = 0$) and in turbulent ($\beta > 0$) environments cast doubts on the validity of the of extrapolating laminar vortex dynamics to the turbulent logarithmic and outer regions. Other works for laminar flows indicate time scales comparable to those shown in figure 4.2(a) for $\beta = 0$, which are longer and which scale differently than those reported for $\beta > 0$ and for real turbulent flows. For instance, the times to maximum growth reported by Suponitsky *et al.* (2005) for a uniform shear flow are $T_{\max}\Omega \gtrsim 6$, where Ω is the mean shear and the Reynolds number is $Re = \Omega y_0^2/\nu = 40$. If we assume that $\Omega = u_\tau/\kappa y$, this would correspond to $\tau_{\max} \gtrsim 2.5$ for $y_0^+ = 16$. Also, Zhou & Adrian (1995) report that weak initial hairpins with sizes $2y_0^+ \approx 100$ dissipate (without generating new individuals) in $t^+ \approx 500$, corresponding to $\tau = t^+/y_0^+ \approx 10$. In a later paper Zhou *et al.* (1999) report that increasing the initial amplitudes of those hairpins leads to generation of secondary hairpins in times $t^+ \approx 70 - 110$, which corresponds to $\tau \approx 1.5-2$. Had those hairpins been embedded in the weak turbulent environment given by $\beta = 0.3$, their initial cross-flow energy would have decreased to less than 30% of its initial value by that time (less than 10% for $\beta = 0.6$), probably precluding their regeneration.

4.4.2. Self-similarity

As discussed in §4.2.1, the system (4.3)-(4.5) admits self-similar solutions, at least within the logarithmic region. Self-similarity implies that there is no fixed length or time scale, so that there are no natural scales for E and t. In that case, any scaling transformation of the latter ($\tau \to \xi = \tau/\tau_c$) should result at most in a scaling transformation of the former,

$$Q(\tau) = S(\tau_c)F(\xi), \tag{4.15}$$

Since $Q(\tau)$ has to be independent of τ_c, differentiation results in

$$\frac{dS(\tau_c)}{d\tau_c}F(\xi) = \frac{S(\tau_c)\tau}{\tau_c^2}\frac{dF(\xi)}{d\xi}, \tag{4.16}$$

which can be integrated to the power law

$$\frac{Q(\tau)}{S(\tau_c)} \sim F(\xi) \propto \left(\frac{\tau}{\tau_c}\right)^{-C}, \tag{4.17}$$

where $S(\tau_c)$ and $dS(\tau_c)/d\tau_c$ have been included in the constant C, and the minus sign has been selected by convenience. A power law has been included in figure 4.1(a), and it describes reasonably well the evolution of the cross flow energy for $\tau \gtrsim 1$, suggesting that the evolution of the burst becomes self-similar after that time. The same result is obtained for Q_u, although in that case the presence of the energy production term, $-\overline{uv}\partial_y U$, leads to a slightly lower absolute value of the exponent. For $\beta = 1$ and $y_0^+ = 400$ we have $C = 6.7$ for Q_u/Q_0 and $C = 7.85$ for Q_{vw}/Q_0.

The self-similarity of the solution to (4.3)-(4.4) can also be verified by considering the time evolution of the centroid of the v^2 distribution,

$$\mathbf{x_v} = (x_v, y_v, 0) = \frac{\int \mathbf{x} v^2 dV}{\int v^2 dV}. \tag{4.18}$$

The two cases with $\beta > 0$ and $y_0^+ = 400$ presented in figure 4.3(a) show that the evolution of y_v/y_0 becomes proportional to τ for $\tau \gtrsim 1$, consistent with the self-similar variables defined in (4.6). The symbols in figure 4.3(a) indicate the instant when $Q/Q_0 \approx 10^{-2}$ and beyond which the burst or the streak has effectively disappeared. The results for cases with $y_0^+ > 50$ agree well with case $y_0^+ = 400$. Although not important from the dynamical point of view, even the case with $y_0^+ = 25$ exhibits a $y_v/y_0 \propto \tau$ when the bursts reach the logarithmic region ($y_v/y_0 \gtrsim 3 \rightarrow y_v^+ \approx 75$), suggesting that even small disturbances coming from the buffer layer would become independent of the wall after long enough times. Note, however, that the energy in those bursts would be negligible by that time.

The wall-normal migration velocity of the centroid varies little with y_0^+ for $y_0^+ > 50$, but it increases considerably with β. However, this increase is roughly balanced by the decrease in the lifetimes, so that the size of the initial burst always increases by a factor of about 2 before its cross-flow energy vanishes. As shown in figure 4.2(a), the lifetimes of the cases with $\beta = 0$ are proportional to y_0^2/ν, and although not shown in figure 4.3(a), the dotted line corresponding to $\beta = 0$ reaches $y_v/y_0 \sim 2$ for $\tau \sim 400$.

Figure 4.3(a) also includes the evolution of y_u/y_0 for $\beta = 0.6$, defined analogously to (4.18) but for the streamwise velocity. It can be observed that y_u grows slower than y_v, remaining closer to the wall. This is because the mean shear is higher in that region, and the amplification is correspondingly larger.

We define the wall-normal distribution of the energy,

$$e_u(t,y) = \iint u^2 dxdz \qquad \text{and} \qquad e_{vw}(t,y) = \iint (v^2 + w^2) dxdz, \tag{4.19}$$

where the volume integrals of (4.12) have been replaced by integrals over wall-parallel planes. These energies are presented in figure 4.3(b), normalized with their

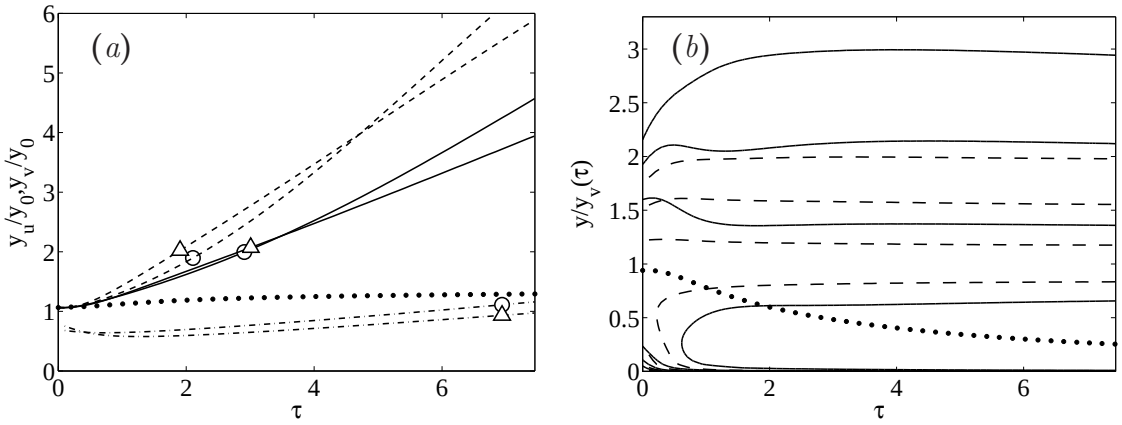

Figure 4.3: (a) Time evolution of the wall-normal position of the centroids of the v^2 and u^2 distributions, for different values of β' and initial sizes of the bursts, $\circ$ is $y_0^+ = 25$ and $\triangle$ is $y_0^+ = 400$. ——, y_v for $\beta = 0.6$;– – –, y_v for $\beta = 1.0$; —·—, y_u for $\beta = 0.6$; ·····, y_v for $\beta = 1.0$ and $y_0^+ = 400$. (b) Evolution of the wall-normal distribution of energy, normalized with its instantaneous value at $y = y_v$, for $y_0^+ = 400$. ——, e_{vw}; – – –, e_u. The levels (from top to bottom) are (0.03, 0.125, 0.5, 2). The dotted line is $y_0/y_v(\tau)$.

instantaneous values at $y = y_v$. The case shown in the figure is $y_0^+ = 400$ with $\beta = 0.6$, but the same results are obtained for $y_0^+ = 200$ and $y_0^+ = 100$, supporting that the evolution of the burst is independent of its initial size. Self-similarity is indicated by approximately horizontal iso-lines of e_{vw} for $\tau \gtrsim 2$ and of e_u for $\tau \gtrsim 1$. This suggests that the u-structures quickly forget about the initial disturbances from which they originate, consistently with the estimations given in §4.2, and in agreement with the results obtained by Suponitsky *et al.* (2005) in a laminar sheared flow.

4.4.3. Velocity structure

Next, we analyze the structure of the velocity disturbances obtained from our linear model. For this purpose we use the velocity field $\langle \mathbf{u} \rangle_L$, which is the time average of $\mathbf{u}$ computed in the interval $\tau \in (0.1, 6)$ and expressed in the reference frame $\mathbf{r} = (\mathbf{x} - \mathbf{x_v})/y_v$. Note that $\mathbf{r}$ is an experimental realization of the self-similar variables defined in (4.6). Because of the approximate self-similarity of the solution, $\langle \mathbf{u} \rangle_L$ resembles the instantaneous realizations of $\mathbf{u}$ for long enough times. Figure 4.4 compares $\langle \mathbf{u} \rangle_L$ for $y_0^+ = 100$ and $\beta = 0.6$, to the averaged velocity field $\langle \mathbf{u} \rangle$ conditioned to a vortex cluster, as described in §3.5. The latter is computed by averaging the velocity field around attached vortex clusters with maximal heights in the range $100 < y^+_{\max} < 300$, extracted from a turbulent channel with $Re_\tau = 950$. The averaged $\langle \mathbf{u} \rangle$ is computed in the reference frame $\mathbf{r} = (\mathbf{x} - \mathbf{x_c})/y_c$, where $\mathbf{x_c}$ is the center of the box that circumscribes each attached cluster. The figure

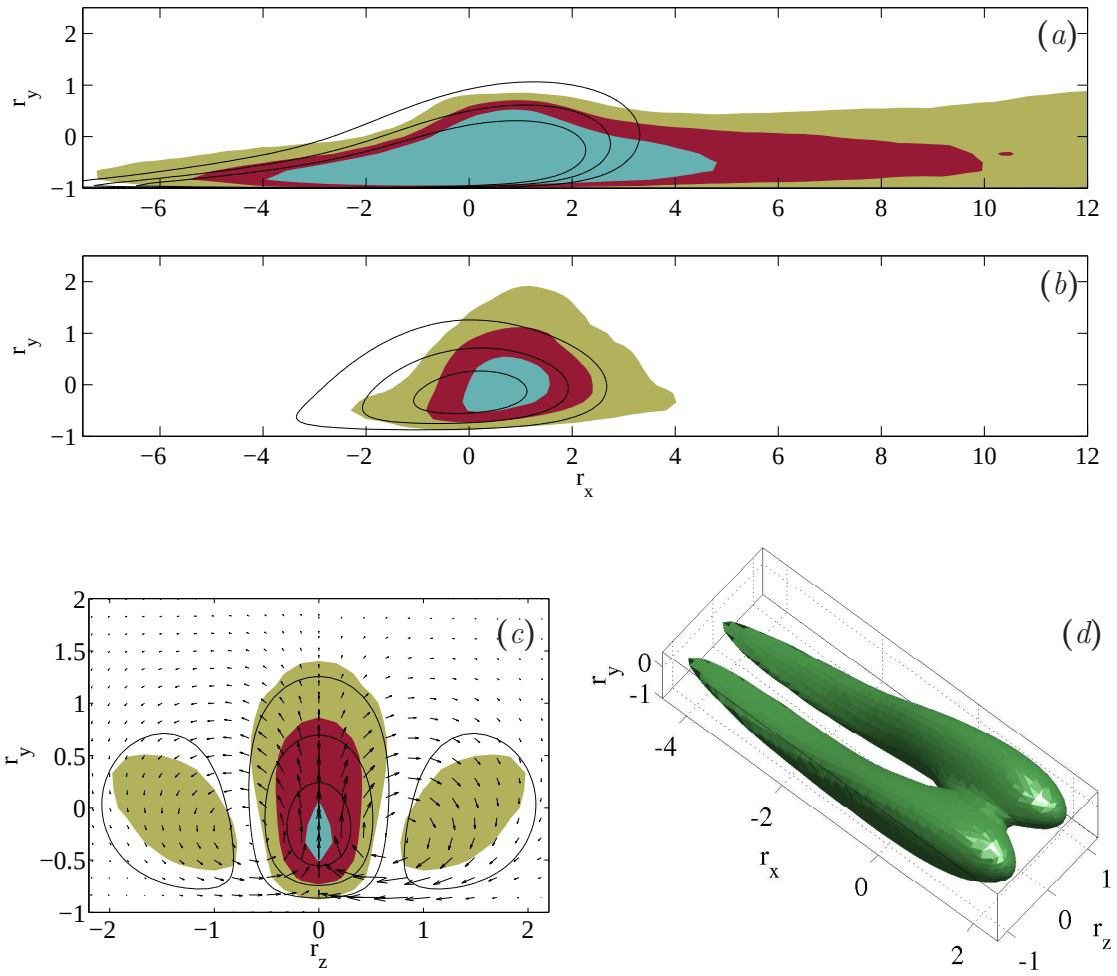

Figure 4.4: Structure of the velocity field around a burst. The line contours represent the average velocity field from our linear calculation, $\langle \mathbf{u} \rangle_L$, for $y_0^+ = 100$. The shaded contours represent the average velocity field conditioned to attached vortex clusters (see text for details). In both cases, the levels plotted are $(0.15, 0.4, 0.75)$ times the maximum wall-normal velocity. (a) Streamwise and (b) wall-normal components in the symmetry plane, $r_z = 0$. (c) Streamwise component in the plane $r_x = 0$. The arrows represent the cross-stream velocities from the linear model (right half of the plot, $r_z > 0$) and the turbulent channel (left half of the plot, $r_z < 0$), both normalized with the maximum of the wall-normal velocity component at $r_z = 0$. (d) Vortex visualization using the Q-criterion (Hunt *et al.*, 1988). The plotted surface is $Q = Q_{rms}$.

shows that the velocity structure of the linear model is approximately the same observed in turbulent channels: a low-momentum region (figure 4.4a) generated by a wall-normal ejection (figure 4.4b) flanked by a pair of hairpin-like quasi-streamwise vortices (figures 4.4c and 4.4d). The same structure is obtained for other values of β and y_0.

The most obvious difference between our linear solution and the simulation data

appears in the streamwise velocity downstream (to the right) of the burst in figure 4.4(a), where $\langle u\rangle_L \approx 0$ beyond $r_x \approx 3$ while $\langle u\rangle$ remains non-zero for the whole length of the box used for the conditional averaging ($r_x = 20$). This difference will be discussed in detail below. Apart from that, other smaller differences are worth noting. Figure 4.4(b) shows that $\langle v\rangle_L$ is located slightly upstream (to the left) of $\langle v\rangle$. The cross-flow visualization of the averaged streak presented in figure 4.4(c) shows that the high-speed regions around $r_z \approx \pm 1$ are slightly stronger in our linear model than in the turbulent channel. The same occurs for the wall-normal and spanwise velocity components, represented in that figure by the arrows, especially underneath the high-speed streaks. Note that the two halves of figure 4.4(c) do not contain the same data. While the half with $r_z < 0$ shows $\langle v, w\rangle$, the half with $r_z > 0$ presents $\langle v, w\rangle_L$. Although low-Reynolds number effects cannot be discarded, these discrepancies may be caused by large-scale inhomogeneities in the turbulent eddy viscosity sampled by the burst. Toh & Itano (2005) and Hutchins *et al.* (2007) have reported that the turbulence intensity below high-momentum structures is higher than average, leading to a locally-increased turbulent dissipation. Such non-linear effect is absent from our model, which might lead to stronger high-velocity streaks and transverse motions near the wall.

The absence of the downstream part of the u-structure of the linear model shown in figure 4.4(a) was anticipated by del Álamo *et al.* (2006). They noted that the velocity difference between the advection velocity of the burst and the upper part of the logarithmic region was not large enough to generate the long, downstream wakes within the observed lifetimes of the bursts. Based on those observations, they proposed that several burst should be associated with a single wake, with larger individuals in front of smaller ones. Unfortunately, instantaneous realizations of the flow are not conclusive on that point, as can be observed in figures 4.5 and 4.6. They show instantaneous realizations of the sizes of the boxes circumscribing clusters that intersect several (x, y) and (x, z) planes, superimposed on streamwise velocity fluctuations. Only the negative fluctuations are shown. The results correspond to the clusters extracted from a $Re_\tau = 950$ turbulent channel by del Álamo *et al.* (2006). We can observe in the figure similar ramps as those observed by Adrian *et al.* (2000). However, a clear ordering from small to large clusters is not discernible in the figures, and even the instantaneous relationship between clusters and low-momentum structures is inconclusive. Note that there is no guarantee that all the clusters in the visualizations are being observed at comparable moments of their lifetimes, and hence their particular relationship with the low-momentum structures is unknown.

Figures 4.5 and 4.6 reinforce the idea of that dynamics of the clusters/bursts and low-momentum structures can not be described by model based on instantaneous hairpins. A description of the dynamics in an averaged sense, like the one presented in this chapter, seems more suitable.

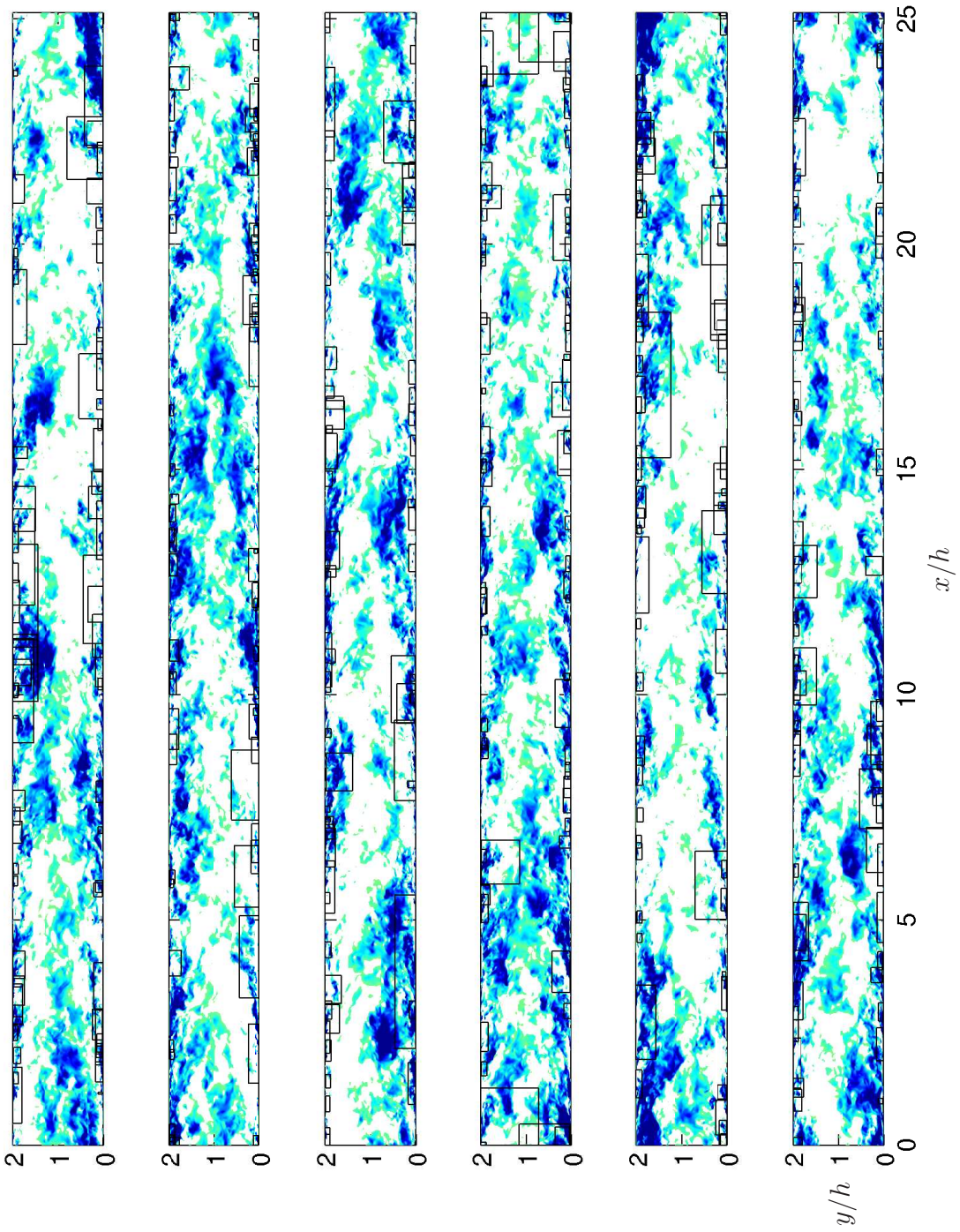

Figure 4.5: Instantaneous visualizations of the negative streamwise velocity fluctuations in a (x, y) plane of a turbulent channel with $Re_\tau = 950$. White is $u^+ > 0$ and blue is $u^+ < -3$. The boxes circumscribing the attached clusters with $y^+_{\max} > 100$ that are intersected by the planes are presented in black.

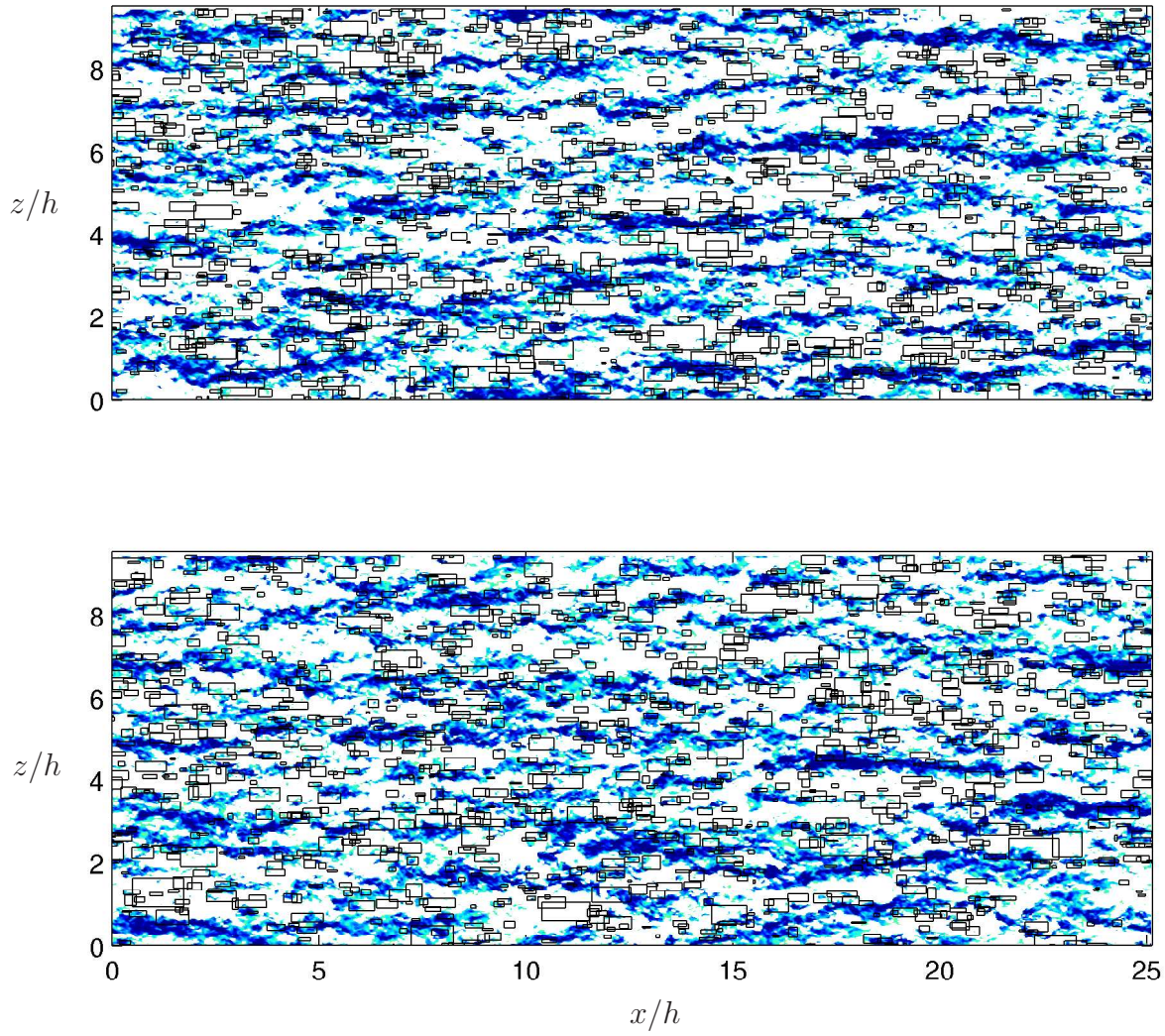

Figure 4.6: Instantaneous visualizations of the negative streamwise velocity fluctuations at $y^+ = 150$, for a turbulent channel with $Re_\tau = 950$. White is $u^+ > 0$ and blue is $u^+ < -3$. The boxes circumscribing the attached clusters with $y^+_{\max} > 100$ are presented in black.

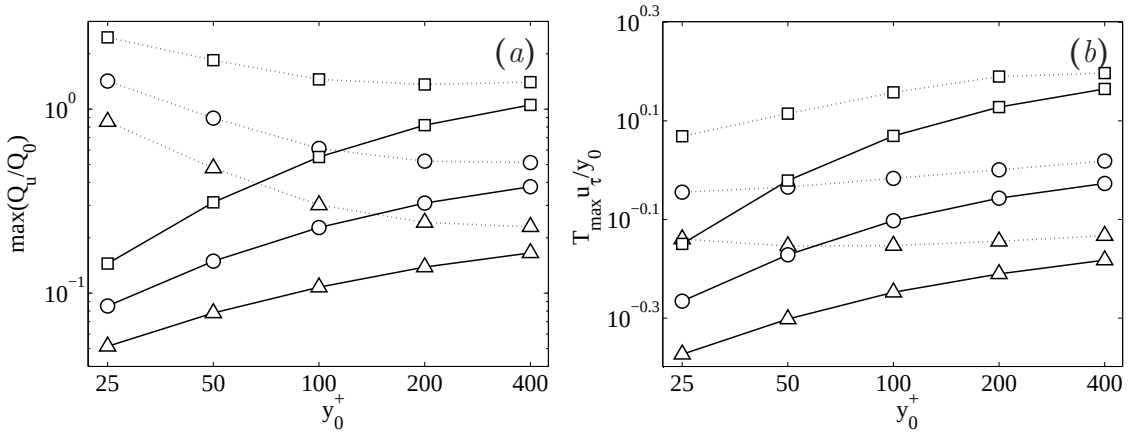

Figure 4.7: Comparison of linear model for smooth and rough walls. (a) Maximum of the streamwise energy, $\max(Q_u/Q_0)$, and (b) time to maximum growth, $T_{\max}$, as a function of y_0^+ and β. Note that the abscissa is in logarithmic scale. ·····, smooth-walled U and ν_T. ——, rough-walled U and ν_T. □, $\beta = 0.3$; ○, 0.6; △, 1.0.

4.4.4. Linear model over rough walls

It is interesting to note that the proposed linear mechanisms can also be adapted to rough-walled flows. Chapter 3 shows that the properties of the bursts/clusters and of their associated velocity fields are not changed when prescribed harmonic disturbances are applied at the walls, destroying the near-wall energy cycle. We tested the effect of a rough-walled mean velocity profile in the linear model by introducing in (4.9) an extra additive constant (ν_W) that takes into account the extra dissipation introduced by the roughness elements. The parameters A, K and ν_W for these rough-walled linear cases were adjusted using a least squares fit to the mean velocity profile of the rough-walled channel labeled **R2** in chapter 2, with $Re_\tau = 632$ and a equivalent sand roughness $k_s^+ = 129$. As in the smooth-walled case, the mean velocity profile used for the linear simulation is obtained for $Re_\tau = 10^9$, and the same computational domain and discretization used for the linear computations with smooth walls is used to solve the rough-walled cases.

In the linear models run with the rough-walled turbulent eddy viscosity, the increase of the dissipation and the reduction of mean velocity gradient near the rough wall weaken the fluctuations of u. As a consequence, small bursts have lower maximal amplifications than larger ones, opposite to the trend found over smooth walls (see figure 4.7a). As the size of the burst increases, the effect of the roughness layer decreases, and the case with $y_0^+ = 400$ has roughly the same $\max(Q_u/Q_0)$ in the smooth- and the rough-walled cases. Figure 4.7(b) shows that this changes on the maximum amplification also modify the time to maximum amplification, although the effect on $T_{\max}u_\tau/\nu$ is smaller than in $\max(Q_u/Q_0)$. Note that the ordinate in figure 4.7(a) varies by a factor of 60, while in figure 4.7(b) it only varies by a factor of 5.

When we focus on the velocity structure developed by the burst, we observe that the wake upstream (to the left) of the burst is shorter in the rough-walled cases, as shown in figure 4.8(a). The effect is the same reported in the velocity field conditioned to tall attached vortex clusters over rough walls in chapter 3. Figure 4.8 includes $\langle u \rangle$ for that case. The agreement between the velocity structure from the rough-walled linear model with that extracted from the fully rough channel is comparable to that observed for the smooth-walled cases, supporting that the linear generation of u-streaks from v-bursts in the logarithmic region is independent of the wall details.

Note that the linear model does not include any direct effect of the roughness over the structures of the logarithmic region. This effect is in fact weak in the wall-disturbed channels, as discussed in chapter 3. Jiménez (2004) estimates that, provided that the height of the roughness elements is smaller than $h/40$, more than one half of the logarithmic region is free from the direct effect of the roughness, which is the situation simulated by the rough-walled linear model studied here.

4.5. Origin of the bursts

In the previous sections we have shown that elongated u-streaks in the logarithmic region can be linearly generated from localized wall-normal velocity bursts. There is ample evidence to support that such bursts, modeled here by a pair of counter-rotating vortices, are frequent enough in wall turbulence to be statistically significant. Similar structures appear in the proper orthogonal decomposition of Moin & Moser (1989), and in the linear stochastic estimation of Moin *et al.* (1987) in low Reynolds number channels, as well as in the conditionally averaged structures of del Álamo *et al.* (2006) in channels at $Re_\tau = 550 - 1900$. Among the most representative properties of those bursts we can find their self-similar distribution of sizes across the logarithmic region (del Álamo *et al.*, 2006), and their relative independence on the details of the wall (see chapter 3). These properties are well captured by the present linear model.

It is worth noting that the u-streaks associated with the bursts have typical sizes much larger than those of the buffer layers streaks. Apart from this, the linear generation of streaks by the interaction of the bursts with the mean velocity profile is analogous to the part of the near-wall energy cycle in which the interaction of the quasi-streamwise vortices with the mean velocity profile give rise to near-wall streaks (Jiménez & Pinelli, 1999).

On the other hand we have seen that the bursts do not live long enough to explain the observations of del Álamo *et al.* (2006), and that the streaks that they generate are shorter than those in the conditional statistics. In particular most of the downstream wake, which is the most prominent feature of the conditionally averaged flow fields, is missing from the linear model. This suggests that the bursts have to be generated within the streaks to which they are associated, roughly aligned initially in the streamwise direction, and roughly with their observed sizes.

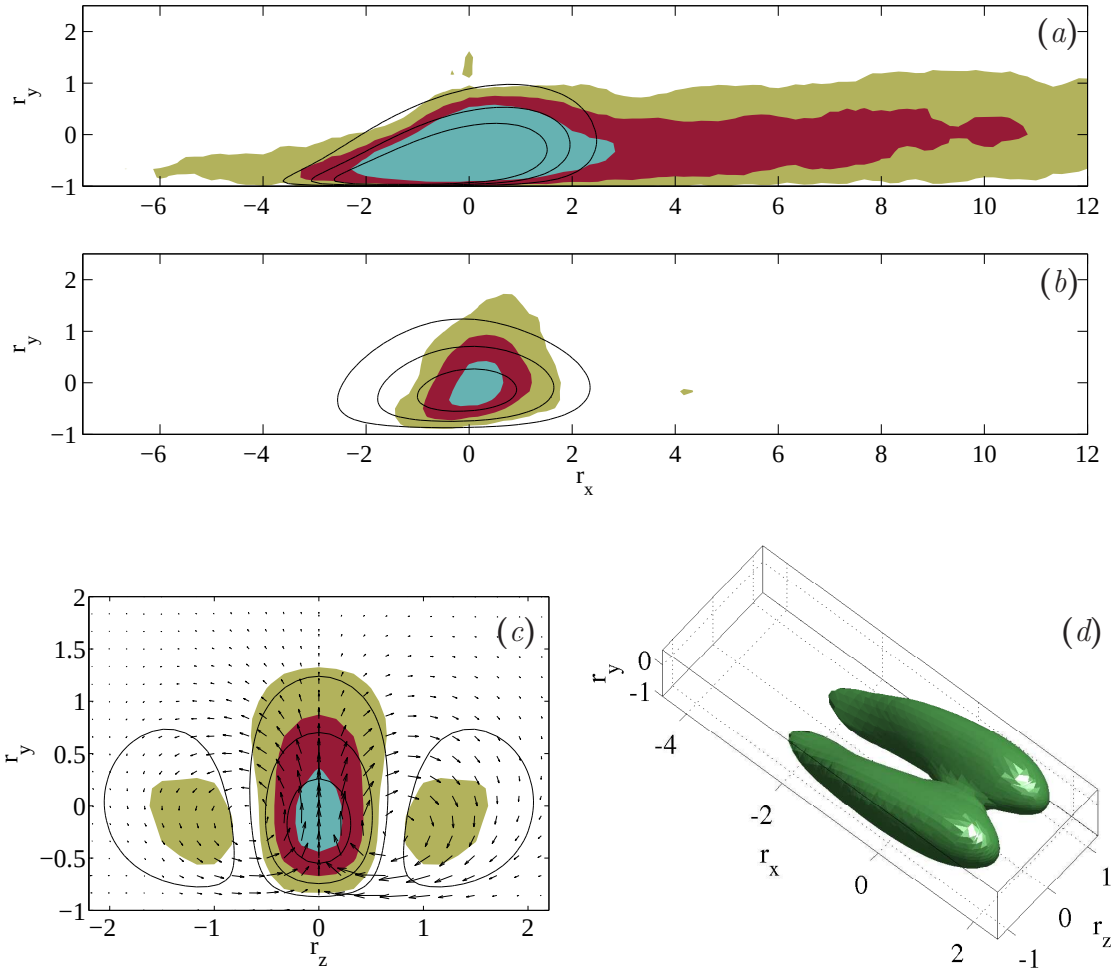

Figure 4.8: Structure of the velocity field around a burst with a rough-walled mean velocity profile. The line contours represent the average velocity field from our linear calculation, $\langle \mathbf{u} \rangle_L$, for $y_0^+ = 100$. The shaded contours represent the average velocity field conditioned to attached vortex clusters with $y^+_{\max} > 200$, extracted from the rough-walled channel presented in previous chapters, **R2**. In both cases, the levels plotted are $(0.15, 0.4, 0.75)$ times the maximum wall-normal velocity. (a) Streamwise and (b) wall-normal components in the symmetry plane, $r_z = 0$. (c) Streamwise component in the plane $r_x = 0$. The arrows represent the cross-stream velocities from the linear model (right half of the plot, $r_z > 0$) and the turbulent channel (left half of the plot, $r_z < 0$), both normalized with the maximum of the wall-normal velocity component at $r_z = 0$. (d) Vortex visualization using the Q-criterion (Hunt *et al.*, 1988). The plotted surface is $Q = Q_{rms}$.

The main remaining question is how are the bursts generated. Taking into account the similarities between u-structures in the present model and those involved in the turbulent cycle of the buffer region, the instability of the streaks appears as a reasonable candidate for the origin of the logarithmic-layer bursts. The results coming out from the linear model are not suitable for a stability analysis, since these streaks are *averaged* structures, rather than instantaneous ones. Hence, we will limit ourselves here to discuss the realizability of several instability mechanisms, using previous results for viscous models of the near-wall streaks.

The most likely sources of instability are the shear layers that surround the low-velocity streak along its sides and top. The easiest to analyze is the top layer, which is approximately two-dimensional and therefore unaffected by the presence of the mean shear. Its instability criterion should be close to the presence of an inflection point in the total velocity profile. The other candidates are the lateral shear layers, whose instability is controlled by the balance between a spanwise inflection point and the wall-normal shear. Schoppa & Hussain (2002) analyzed the normal-mode and transient-growth stability of synthetic buffer-layer low-speed streaks. They showed that they are unstable to normal modes whenever $\theta = \tan^{-1}(\partial_z u/\partial_y U) > 50°$, and that even marginally stable streaks are capable of significant transient growth, leading to solutions which are very similar to the least damped normal modes.

In order to trigger the lateral or the top shear layer instabilities, the streaks have to be quite strong. However, the streaks obtained in the linear model are somewhat weak, as anticipated by figure 4.1. We can directly check the effect of the linear streaks on the mean velocity profile by assigning them initial amplitudes of the order of those observed in real turbulent flows. Figure 4.9 shows the total velocity and its gradient in the symmetry plane of the burst, for a linear bursts with $y_0^+ = 400$ and an initial maximum wall-normal velocity of $v^+ = 2$. The time shown in figure 4.9 is $\tau = 1$, close to the maximum amplification. It is clear that the effect of the linear streak on the mean velocity profile is weak, and the averaged structures coming out of the linear model are barely able to satisfy the instability criteria presented in the previous paragraphs. Note that, because of the self-similarity of the bursts and streaks within the logarithmic layer, this observation also applies to bursts of all sizes with the same initial intensity.

We also have to consider the possible effects of the outer region on the logarithmic layer. Del Álamo & Jiménez (2006) showed that the maximum transient growth for the modes reaching into the outer region is stronger than for those mostly contained within the logarithmic layer. In fact, previous analysis of the stability properties of wall-bounded flows had only been able to obtain outer unstable modes (Butler & Farrel, 1992; Reddy & Henningson, 1993). The initial conditions leading to maximally growing modes usually consist of pairs of counter-rotating streamwise vortices that generate u-structures when they interact with the mean shear. We have tested the effect of the outer region by running the linear model for a burst with $y_0^+ = 400$ and $\beta = 0.6$, but using the U and ν_T profiles of turbulent channels with finite Reynolds numbers ($Re_\tau = 2000, 4000$ and 8000). When compared with

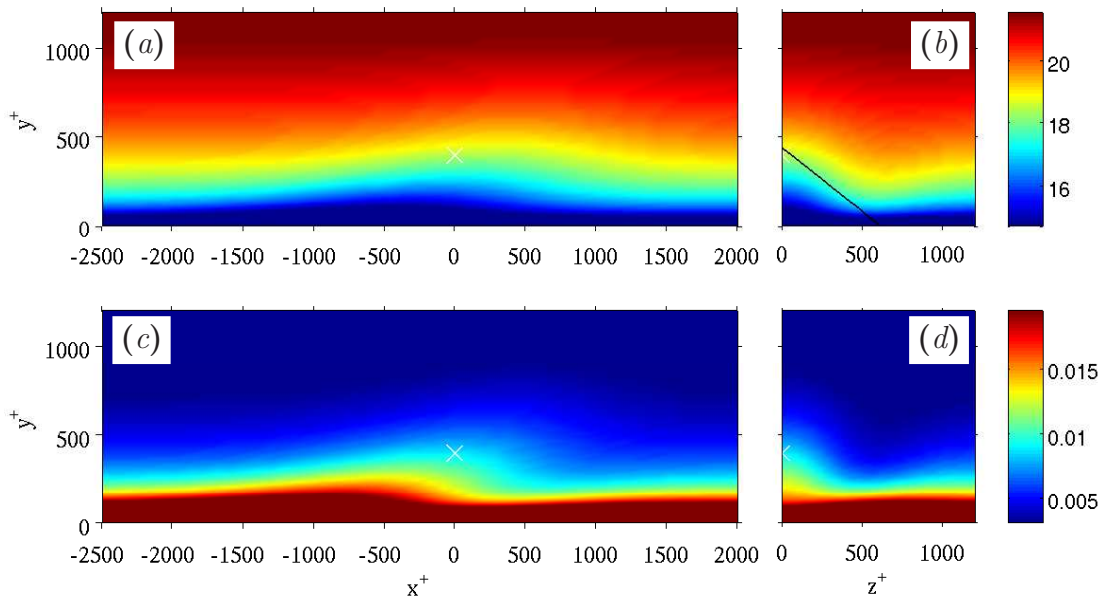

Figure 4.9: Realizations of the total velocity $(U+u)$ (a and b) and of the total velocity gradient $\partial_y(U+u)$ (c and d) at $\tau = 1$. (a) and (c), at $r_z = 0$. The data comes from our linear model for the infinite long logarithmic layer, with $y_0^+ = 400$, $\beta = 0.6$. The maximum wall-normal velocity of the initial burst is $v^+ = 2$. The dotted line in (b) is $\theta = 50°$.

the previously discussed case of an infinitely long logarithmic layer, the cases with a finite Re_τ are qualitatively similar, but their peak energy amplification increases as Re_τ decreases. This is a consequence of the increase of the lifetimes of the bursts as they emerge into the outer region, where the turbulent eddy viscosity levels off, and eventually decreases. Figure 4.10 shows the instantaneous velocity field of the channel with $Re_\tau = 2000$ at maximum amplification, and we can observe that its effect on the mean velocity profile is larger than for the case of an infinite long logarithmic region.

Note that this scenario reverses the direction of causality in wall-bounded turbulence. Instead of having bursts generated at the wall and rising towards the outer layer, the suggestion is that only large streaks reaching above the logarithmic layer become unstable, and create what is necessarily a very large burst. The sweep created by that ejection then generates, or perhaps triggers, the structures that are observed near the wall. The origin of large streaks and bursts would then have to be sought in a cycle similar to that in the buffer layer, but involving turbulent structures spanning the whole flow. This would be consistent with the shape of the streaks created by the linear model, which are only created below the center of the burst (see figures 4.4 and 4.8). The logarithmic layer would then only have a passive

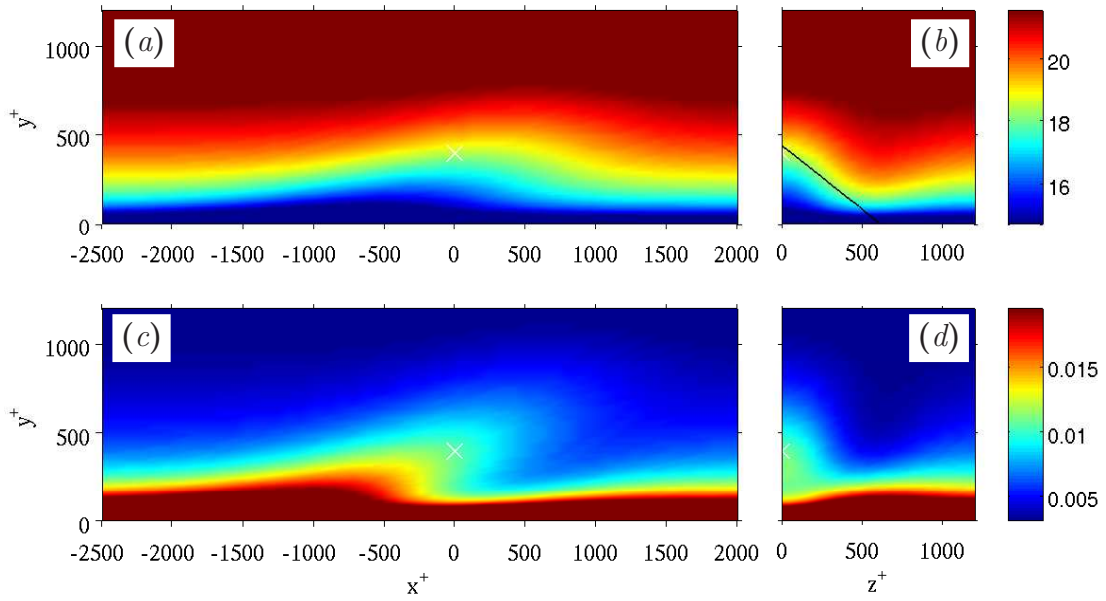

Figure 4.10: Realizations of the total velocity $(U+u)$ (a and b) and of the total velocity gradient $\partial_y(U+u)$ (c and d) at $\tau = 1$. (a) and (c), at $r_z = 0$. The data comes from our linear model for a finite channel with $Re_\tau = 2000$, with $y_0^+ = 400$, $\beta = 0.6$. The maximum wall-normal velocity of the initial burst is $v^+ = 2$. The dotted line in (b) is $\theta = 50°$.

role, similar to the forward energy cascade across the inertial range in isotropic turbulence. Exploring that possibility in detail must be attempted in future work, but it should be mentioned that similar top-down scenarios have been proposed from the meteorological community (e.g. Hunt & Morrison, 2000).

From the results presented in figures 4.9 and 4.10 is not possible to decide which of the shear layers (top or lateral) are more likely to become unstable in the u-streaks of the logarithmic region. This is an important question, since it determines the shape of the streaks. The dominant instability in the buffer layer is sinuous, associated with the lateral shear layers (Schoppa & Hussain, 2002), and the typical structures leading to bursting in that region are also known to be sinuous (Stretch, 1990; Jiménez & Moin, 1991). On the other hand, a Kelvin–Helmholtz instability of the upper shear layer (Skote *et al.*, 2002) generates varicose oscillations of the streak, consistent with many observations in the logarithmic and outer regions, such as those by Robinson (1991*b*), Blackburn *et al.* (1996), Chong *et al.* (1998), Adrian *et al.* (2000), Ganapathisubramani *et al.* (2003) and del Álamo *et al.* (2006). It turns out that the averaged velocity fields conditioned to a burst do switch character above the buffer layer. Consider figure 4.11, which was obtained from the channel by del Álamo *et al.* (2006) at $Re_\tau = 950$. When the conditioning clusters are restricted to the

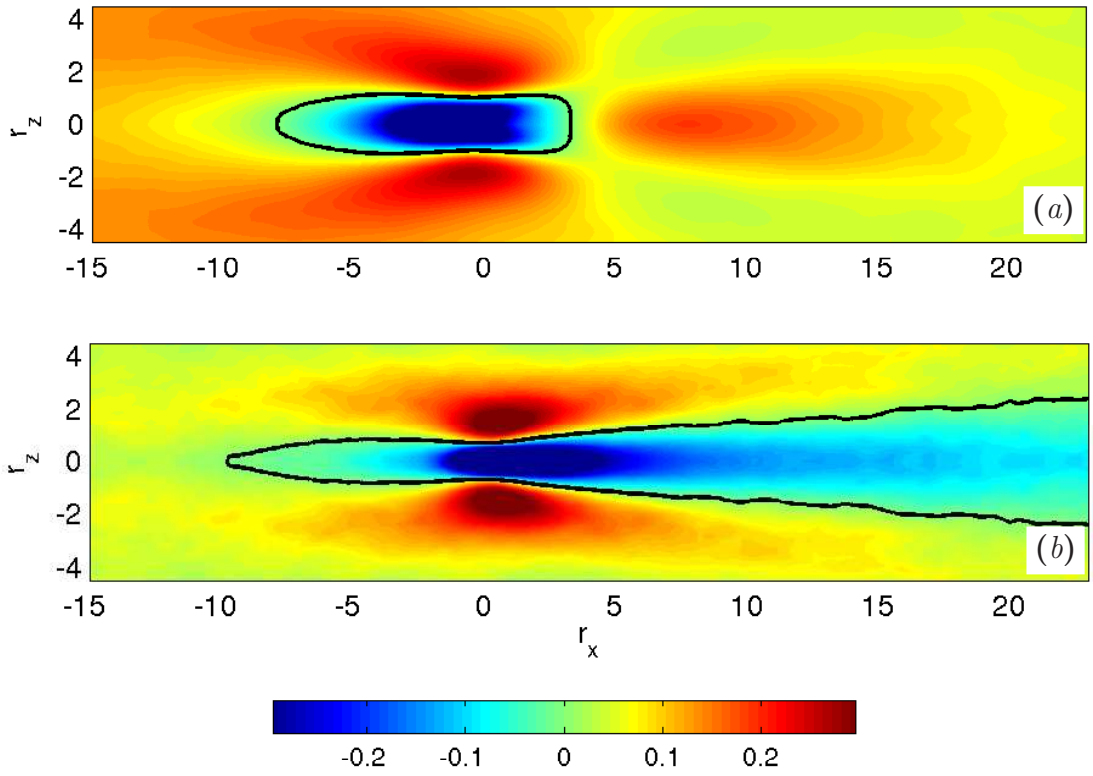

Figure 4.11: Streamwise velocity conditioned to clusters extracted from a turbulent channel with $Re_\tau = 950$ (del Álamo *et al.*, 2006). (a) Sinuous mode, conditioning clusters having minimum and maximum wall-distances of $y^+_{\min} < 20$ and $y^+_{\max} \in (10, 50)$. (a) Varicose mode, $y^+_{\min} < 20$ and $y^+_{\max} \in (100, 200)$. The black contours correspond to $\langle u \rangle = 0$.

buffer region (figure 4.11a), the averaged velocity $\langle u \rangle$ at $r_y = 0$ exhibits positive and negative patches alternating along the streamwise direction. This is the footprint of a sinuous deformation, with the two possible orientations superimposed by the statistics. When the clusters are restricted to the logarithmic region (figure 4.11b), the positive patches are aligned along the streamwise direction, consistent with a varicose deformation. Note that other interpretations of these figures are possible, such as a change in the distance among consecutive clusters along the streak, which would appear as a series of low-velocity spots in the wake of one cluster, but each of which would actually be due to a different cluster. An even simpler interpretation could be that the higher perturbation background in the logarithmic layer smears the sinuous signature, which is simply not seen.

Even so, a change in the dominant instability mode for the streaks would be consistent with the analysis of Kawahara *et al.* (2003), who computed the first two terms of the asymptotic expansion of the most unstable eigenmodes of a corrugated vorticity sheet near a wall, in terms of the wavenumber. The varicose and sinuous

eigenvalues were equal to lowest order, but the first order correction was more unstable for the sinuous mode near the wall, and for the varicose one away from it. The effect was small, but its possible relation with the above observations deserves further investigation.

4.6. Conclusions

We have described a mechanism that generates streamwise velocity streaks in the logarithmic region of wall-bounded turbulent flows, starting with a initial wall-normal velocity ejection or burst with cross-stream dimensions of the order of its wall-distance. The analysis of the orders of magnitude of the terms in the Navier–Stokes equations shows that the dynamics of both the burst and the streak are linear, except for the initial creation of the burst which is outside this simplified model. The main role of the non-linear interaction with the background turbulence is to limit the growth of the structures, and that effect has been introduced in the linearized equations with a turbulent eddy viscosity. Therefore, the present linear model describes the ensemble-averaged behavior of the eddies, rather than the evolution of any particular realization.

Although the basic magnitude of the subgrid eddy viscosity has been taken from that required to create the mean velocity profile, we have paid special attention to the effect of the fraction of the mean tangential stress that is carried by it. For that purpose, we have varied the fraction of the subgrid stress from a purely laminar case, in which only the molecular viscosity is active, to a fully turbulent one in which all the tangential stress is carried by the eddy viscosity. From comparisons with experimental results, the optimum subgrid percentage has been found to be about 60%, which is in reasonable agreement with experimental spectral information. Note that, in the laminar limit, our model would be essentially a linearized version of the non-linear laminar simulations by Zhou *et al.* (1999).

We have performed numerical simulations of the linearized equations in logarithmic layers at virtually infinite Re_τ, so that the effect of the outer flow is neglected. We have shown that when the initial condition extends above the buffer region the evolution of the system quickly becomes self-similar, until the turbulent eddy viscosity dissipates the burst in times comparable to its turn-over time. In that process, the v-bursts are barely able to double their initial sizes, independently of the fraction of the Reynolds stresses modelled by the eddy viscosity. This is in agreement with the simulations of Zhou *et al.* (1999), where the hairpins only increase their initial heights by about a factor of two.

The interaction of the burst with the mean velocity gradient generates an elongated low-velocity streak that lives longer and decays slower. This u-structure is located mostly upstream and *below* the burst, where the mean velocity gradient is largest. The overall structure agrees well with the upstream part of the wakes reported by del Álamo *et al.* (2006), but the downstream part of the latter is absent in the linear model. This, and the lack of any obvious mechanism that would allow

bursts created in the buffer layer to grow to the potentially infinitely-larger scales of the logarithmic region, leads us to conclude that the bursts have to be created within the streaks to which they are statistically associated, and that they have to be created with roughly the same size at which they are observed. The same conclusion was reached from order-of-magnitude considerations by del Álamo *et al.* (2006). On the other hand, the agreement between the lifetimes computed from the model with those in turbulent channels, and the correspondence between the upstream parts of the velocity structures in both cases, suggest that the present linear model is a fair representation of the evolution of the logarithmic-layer bursts.

These conclusions contradict those in Zhou *et al.* (1999). In the first place, the large difference between the lifetimes implied by the present model and those of the hairpins in their laminar simulations casts some doubts on the applicability of the latter to a turbulent case. Our results suggest that the perturbations due to the background turbulence would smear out any ejection before the nonlinearity has time to regenerate the burst. Our conclusion is that the hairpin trains observed in simulations and in experiments have to be a consequence, rather than the cause of the streaks (del Álamo *et al.*, 2006), and that they would therefore be essentially passive.

In fact, preliminary stability considerations have suggested that the streaks created within the logarithmic layer by the burst are too weak to create new bursts, even when the intensity of the initial conditions is chosen to be strong enough as to be likely unrealistic. In that sense, the present model does not provide a viable explanation for the whole regeneration cycle of wall turbulence outside the buffer layer, or for the origin of the bursts. We have shown evidence suggesting that there may be a change in the dominant deformation mode of the streaks away from the wall, with sinuous modes being more important in the buffer region, and varicose ones in the logarithmic layer.

Finally, we have shown that the peak amplification increases when the outer region is included in the model, by considering a finite Re_τ. This is caused by the lower eddy viscosity encountered by the streak as it reaches the upper edge of the logarithmic layer. We have suggested that this might provide an answer to the conundrum about the regeneration cycle away from the wall, which would reside predominantly in the outer region, while the logarithmic layer would be subordinated to it. There is, as far as we know, very little direct evidence for such an scenario, which would reverse the flow of causality commonly assumed for wall-bounded flows, but we have noted that similar proposals have been made from the meteorological community.

Chapter 5

Conclusions and future work

The present thesis tries to shed some light on the inner-outer interactions in wall-bounded turbulence, and their role in the dynamics of the flow. The main tool used to investigate these interactions is the set of DNSes presented in chapter 2. In the simulations performed for this thesis, the standard non-slip and impermeability boundary conditions that are natural to smooth walls have been replaced by a single-harmonic velocity disturbance with non-zero tangential Reynolds stresses at the walls. We have shown that the effect of these disturbances is to perturb, and eventually destroy, the near-wall energy cycle characteristic of smooth-walled flows. The wall is populated by a pattern of locally-separated regions that interact with the flow above them. As a consequence, the near-wall streaks and the quasi-streamwise vortices are shortened, while the wall-normal and spanwise velocity fluctuations are enhanced in the buffer region. The Reynolds stresses are enhanced near the wall, where the mean velocity gradient is reduced, resulting in a lower mean velocity at the upper limit of the wall-region.

We have argued that these modifications are typically encountered in turbulent flows over rough walls, and the present boundary conditions have been interpreted as a means of simulating the effect of wall roughness without having to deal with the details of the flow around the roughness elements. The characterization of the present results in terms of their equivalent sand roughness have indicated that one of the cases is transitionally rough, while the rest are in the fully rough regime. We have also discussed that the present DNSes can be understood as simulations of a core flow without a wall region, in the same sense that the autonomous channel in Jiménez *et al.* (2004) is a wall region without a core region.

Two complementary approaches have been used to analyze the data obtained from the wall-disturbed simulations. The first one is a spectral analysis, focused on the energy distribution among the different scales (chapter 2) and the second one is a statistical comparison of the coherent structures of vorticity in the outer region of wall-disturbed and smooth-walled cases (chapter 3). Both analyses are complementary and provide a complete description of the flow.

The most important result obtained from the spectral analysis is that the changes produced by the wall-roughness are limited to the roughness sublayer, defined in terms of the additional Reynolds stresses introduced by the wall forcing. We have seen that the flow within this roughness sublayer is dominated by the wavenumbers of the forcing and its harmonics. However, the spectral distribution of energy above it is essentially the same found above the near-wall region of smooth-walled turbulent flows. This result supports Townsend's hypothesis and the classical theory, which had been recently challenged by several experiments and simulations, like those by Krogstad *et al.* (1992); Djenidi *et al.* (1994); Krogstad & Antonia (1994, 1999); Bhaganagar & Kim (2003); Leonardi *et al.* (2003); Orlandi *et al.* (2003); Poggi *et al.* (2003). Our results are also in agreement with other experiments and simulations, like Perry & Abell (1977); Perry *et al.* (1986); Ligrani & Moffat (1986); Perry *et al.* (1987); Raupach *et al.* (1991); Keirsbulck *et al.* (2002); Ashafarian *et al.* (2004); Bakken *et al.* (2005); Flack *et al.* (2005).

However, some care has to be taken when claiming the independence of the outer region on the details of the wall. We have shown in §2.5.1 that the wall forcing is indeed able to modify the intensity of the global modes, which are the largest structures of the outer region, correlated across the whole flow thickness. The results obtained in the wall-disturbed simulations show that the changes in the intensity are not accompanied by changes in the shape of these modes, nor in changes in the correlation of their wall-normal and streamwise components, nor in their advection velocities. Due to the limited Reynolds numbers of our DNEes, we have used data from experimental turbulent flows over smooth and rough surfaces to show that the velocity scale of those global modes is proportional to $u_\tau \log(Re_\tau)$. This velocity scale collapses the intensity of the streamwise velocity fluctuations at a fixed wall-normal distance for a wide range of Reynolds numbers, several values of the roughness functions, and for two canonical geometries, channels and pipes. It has been discussed that such a dependence on the viscosity in the outer region of fully rough turbulent flows is surprising, and that maybe the fully rough cases with the higher Re_τ are leveling off. Unfortunately, the data are not conclusive on this matter. All that can be said is that in the hydraulically smooth and transitionally rough regimes, the velocity scale of the global modes seems to be proportional to $u_\tau \log(Re_\tau)$. Higher Reynolds numbers are needed to elucidate the reasons for that dependence, and also to describe the behavior of the global modes in fully rough flows.

The second approach used in this thesis is the study of the statistical properties of clusters of vortices, in comparison to the smooth-walled data of del Álamo *et al.* (2006). We have seen that, similar to the smooth-walled case, the clusters extracted from the rough-walled simulations naturally separate in two distinguished families: wall-detached and wall-attached. The former are dissipative eddies, with sizes proportional to the Kolmogorov scale. We have seen that they resemble the worms found in isotropic turbulence by Jiménez & Wray (1998), and that they are not modified in the outer region by the wall forcing. In the roughness sublayer, the

density of detached clusters varies slightly with respect of that observed in the buffer region of smooth-walled flows.

We have shown that, similar to what is observed over smooth walls (del Álamo *et al.*, 2004), the attached clusters in the rough-walled cases are statistically associated to wall-normal velocity bursts, which are understood here as the transient ejection of fluid in a region that evolves coherently until it decays (Kim *et al.*, 1971). Even when the attached nature of these objects might suggest that they should feel the changes in the wall, we have concluded in §3.4 that this is not the case. The distribution of sizes of the attached clusters over rough walls exhibit the same self-similar behavior previously observed for smooth-walled flows at higher Reynolds numbers, and the probability density function of their shapes is only marginally dependent on the wall details. We have also seen that the density of attached clusters collapses for the smooth- and rough-walled cases, independent of the threshold used to identify them. We have presented the average velocity fields conditioned to the attached clusters that reach outside the roughness sublayer, and we have seen that they agree quite well with those obtained for smooth-walled flows: a Λ-vortex with a wall-normal velocity ejection between its legs, and a long cone-shaped, low-momentum structure that extends downstream of the conditioning object.

However, besides the independence of the attached clusters on the details of the wall, we have seen that the low-momentum structures associated with them are modified upstream and below the burst, in the roughness sublayer. We have argued these modifications are connected to the changes in the mean velocity gradient, rather than to the direct effect of the wall-disturbances. We have also seen that the wakes are quite similar in their downstream end, independent of the nature of the wall. We have shown that they can not be much wider that the flow thickness, and we have been able to connect them with the global modes discussed in chapter 2.

In the final part of this thesis we have put together all these observations into a simple linear model, that is able to explain the generation of the low-speed streaks of the logarithmic region. By analyzing the orders of magnitude of the terms in the Navier-Stokes equations, we have shown in §4.2 that the dynamics of the attached bursts are essentially linear. The characteristic time associated to the mean shear is shorter than their eddy turnover time, so the Rapid Distortion Theory can be applied. The only role of the non-linear interactions of the eddy with the background turbulence and with itself is to set a bound on the growth of the structure. This effect is introduced into the linear model by the coarse approximation of the eddy viscosity, which has been proved to work for elongated structures in Jiménez *et al.* (2001*a*), Jiménez *et al.* (2004), and del Álamo & Jiménez (2006).

Therefore, we have performed several simulations of a logarithmic region governed by the linearized Navier-Stokes equations with a eddy viscosity model. The Reynolds number in these simulations is virtually infinite, and the outer region is absent. The initial condition for those simulations has been provided by an idealized version of the bursts obtained in the conditional average of the attached clusters in §3.5. We have allowed the variation of the percentage of the total Reynolds stresses

accounted by the eddy viscosity model, in order to evaluate its effect on the linear model. It is important to bear in mind that the use of the eddy viscosity implies that the linearized equations describe the evolution of an ensemble-averaged eddy, rather than the evolution of any particular one. As a consequence, the linear model presented in chapter 4 gives us information about average lifetimes, mean propagation in the wall-normal direction and average sizes and shapes of the resulting velocity structure.

The results of the linear simulations have shown that a localized burst can generate linearly an elongated upstream u-streak. This streak reaches its maximum intensity soon after the initial burst is dissipated by the background turbulence. By that time, the evolution of the system is roughly self-similar, and the burst has only been able to double its initial size in the process. We have shown that the lifetimes and the time-averaged structure of the eddies of the linear model agree reasonably well with those extracted from turbulent channels, suggesting that this mechanism is statistically significant in real turbulent flows. We have also applied the linear model to the mean velocity profile obtained for rough-walled flows, showing that it is robust and that it operates similarly over smooth and rough walls.

We have also discussed the absence of the downstream part of the low-momentum wakes in the streaks generated by the linear model. This may be one of the most interesting outcomes from the linear simulations, since it suggests that the cones are the cause rather than the effect of the bursts. However, we have estimated that the linearly generated streaks of the logarithmic regions are too weak to change the stability properties of the local mean velocity profile, and the limited wall-normal growth of the bursts cast doubts on their capability of populating the logarithmic region of a high-Reynolds number flow by growing from the buffer region, where the amplification is higher.

It is interesting to note that, when the effect of the outer region is introduced in the linear model, the reduction of the turbulent eddy viscosity above the logarithmic region allows for larger growths and consequently larger deformations of the local mean velocity. This observation may provide an answer to the conundrum about the generation of wall-normal bursts within the logarithmic region. Our suggestion is that the causality assumed in most models of wall-bounded turbulence may be reversed, and that the outer region may be critical for the dynamics of the logarithmic layer. The latter would be essentially a passive layer, subordinated to the outer region.

It has also been discussed in this thesis how the instantaneous association of clusters/packets and log-layer streaks is not as simple as suggested by the hairpin packet model of Adrian *et al.* (2000). The instantaneous visualizations of a turbulent channel with $Re_\tau = 947$ have shown that the organization of small to large packets within a low-velocity streak is not conclusive, and that indeed there are many clusters that appear outside of the streaks. Also, the results of the linear model indicate that the non-linear process proposed by Zhou *et al.* (1999) can be hardly extrapolated from the laminar simulations to the real turbulent flows, since the eddies are

dissipated by the background turbulence in shorter times than required by the autogeneration mechanism to produce new hairpins. Finally, the hairpin packet model suggests that these structures growth from the wall. However, the comparison of the attached clusters over smooth- and rough-walls suggests that the cluster/bursts do not come from the wall, or alternatively that they forget quickly about their origins. We have noted that these two options do not exclude each other. Indeed, while the lifetimes reported in del Álamo *et al.* (2006) support the first, the results of the linear analysis presented in chapter 4 support the second.

The conclusion of the present thesis is that the dynamics of the logarithmic and outer regions of wall-bounded turbulence are driven by wall-normal velocity bursts generated at all heights. In average, these bursts pump low-velocity fluid from the wall into the outer region, generating the very large low-velocity structures commonly observed in numerical simulations and in experiments. The higher energy production and dissipation within the bursts results in the percolation of the clusters, which are essentially markers of the bursts. The low-momentum structures generated by these bursts are located upstream and below them, since the velocity difference between the center of the burst and the wall is always larger than that available above the burst. The lifetimes of the bursts are short, and several burst of different sizes appear associated, in an statistical sense, with a single low-momentum region. The hypothesis, which needs further confirmation, is that the largest bursts are born in the outer region and generate the low-momentum structures of the logarithmic region, which trigger an unspecified instability that produce new (smaller) bursts.

The future research that may follow the present thesis is the analysis of the cascade of the logarithmic layer. Our results suggest that this cascade is fairly independent of the wall, and that it might be tightly coupled with the dynamics of the outer region. These issues require further research. Also, the lineal model presented here is only able to explain the average generation of streaks by wall-normal bursts. The generation of the wall-normal bursts is not understood, and it might need a model based on instantaneous eddies, rather than in averaged ones.

Finally, it is interesting to note that the relative independence of the outer region on the details of the wall should allow the use of the present wall forcing to emulate real k-type roughness in complex geometries. For this purpose, the parameters of the forcing (wavelengths and intensities) will have to be tuned to provide the appropriate wall friction and a decrease in the activity of the buffer region equivalent to that of the real roughness. Other details of the direct effect of the wall-roughness on the flow should not be important. Also, the possibility of reproducing the behavior expected for d-roughness triggering an instability of the outer region with the boundary conditions deserves further investigation. The instability analysis of Jiménez *et al.* (2001*b*) showed that the formation of spanwise rollers over porous walls was related to an instability of the outer region, involving both Kelvin–Helmholtz instability and a neutral inviscid shear waves of the mean velocity profile. A similar mechanism could be present in d-type rough-walled flows, a possibility that should be explored

in the future.

References

Acarlar, M. S. & Smith, C. R. 1987*a* A study of hairpin vortices in a laminar boundary layer. part 1. hairpin vortices generated by a hemisphere protuberance. *J. Fluid Mech.* **175**, 1–41.

Acarlar, M. S. & Smith, C. R. 1987*b* A study of hairpin vortices in a laminar boundary layer. part 2. hairpin vortices generated by fluid injection. *J. Fluid Mech.* **175**, 43–83.

Adrian, R. J. 2007 Hairpin vortex organization in wall turbulence. *Phys. Fluids* **19**, 041301.

Adrian, R. J. & Liu, Z. C. 2002 Observation of vortex packets in direct numerical simulations of fully turbulent channel flow. *J. Vision* **5**, 9.

Adrian, R. J., Meinhart, C. D. & Tomkins, C. D. 2000 Vortex organization in the outer region of the turbulent boundary layer. *J. Fluid Mech.* **422**, 1–53.

Adrian, R. J. & Moin, P. 1988 Stochastic estimation of organized turbulent strcuture - Homogeneous shear-flow. *J. Fluid Mech.* **190**, 531–559.

del Álamo, J. C. & Jiménez, J. 2001 Direct numerical simulation of the very large anisotropic scales in a turbulent channel. In *Ann. Res. Briefs*, pp. 329–341. Center for Turbulence Research, Stanford University.

del Álamo, J. C. & Jiménez, J. 2003 Spectra of the very large anisotropic scales in turbulent channels. *Phys. Fluids* **15**, L41–L44.

del Álamo, J. C. & Jiménez, J. 2006 Linear energy amplification in turbulent channels. *J. Fluid Mech.* **559**, 205 – 213.

del Álamo, J. C. & Jiménez, J. 2008 Convection velocities in wall-bounded turbulence In preparation.

del Álamo, J. C., Jiménez, J., Zandonade, P. & Moser, R. D. 2004 Scaling of the energy spectra of turbulent channels. *J. Fluid Mech.* **500**, 135–144.

del Álamo, J. C., Jiménez, J., Zandonade, P. & Moser, R. D. 2006 Self-similar vortex clusters in the logarithmic region. *J. Fluid Mech.* **561**, 329–358.

Ashafarian, A., Andersson, H. I. & Manhart, M. 2004 DNS of turbulent flow in a rod-roughened channel. *Int. J. Fluid Flow* **25**, 373 – 383.

Bakewell, H. P. & Lumley, J. L. 1967 Viscous sublayer and adjacent wall region in turbulent pipe flow. *Phys. Fluids* **10**, 1880–1889.

Bakken, O. M., Krogstad, P. A., Ashfarian, A. & Andersson, H. I. 2005 Reynolds number effects in the outer layer of the turbulent flow in a channel with rough walls. *Phys. Fluids* **17**, 065101.

Balakumar, B. J. & Adrian, R. J. 2007 Large- and very-large-scale motions in channel and boundary-layer flows. *Phil. Trans. R. Soc. A* **365**, 665–681.

Batchelor, G. K. 1953 *The theory of homogeneous turbulence*. Cambridge U. Press.

Batchelor, G. K. & Townsend, A. A. 1949 The nature of turbulent motion at large wave numbers. *Proc. R. Soc. London A* **199**, 513–520.

Bechert, S. W., Bruse, M. & Hage, W. 2000 Experiments with three-dimensional ribblets as an idealized model of shark skin. *Exp. Fluids* **28**, 403–12.

Bhaganagar, K. & Kim, J. 2003 Effects of surface roughness on turbulent boundary layers. In *Bull. Am. Phys. Soc., Vol 48, No 10*, p. 87.

Blackburn, H. M., Mansour, N. N. & Cantwell, B. J. 1996 Topology of fine-scale motions in turbulent channel flow. *J. Fluid Mech.* **310**, 269–292.

Blackwelder, R. F. & Eckelmann, H. 1979 Streamwise vortices associated with the bursting phenomenon. *J. Fluid Mech.* **94**, 577–594.

Boussinesq, J. 1877 Essair sur la théorie des eaux courrantes. *Mém. Acad. Sci. Paris* **22**, 1–680.

Bradshaw, P. 1967 Inactive motion and pressure fluctuations in turbulent boundary layers. *J. Fluid Mech.* **30**, 241–258.

Brown, G. L. & Thomas, A. S. W. 1977 Large structure in a turbulent boundary layer. *Phys. Fluids* **20**, S243.

Bullock, K. J., Cooper, R. E. & Abernathy, F. H. 1978 Structural similarity in radial correlations and spectra of longitudinal velocity fluctuations in pipe flow. *J. Fluid Mech.* **88**, 585–608.

Butler, K. M. & Farrel, B. F. 1992 Three-dimensional optimal perturbations in viscous shear flow. *Phys. Fluids A* **4**, 1637–1650.

Butler, K. M. & Farrel, B. F. 1993 Optimal perturbations and streak spacing in wall-bounded turbulent shear flow. *Phys. Fluids A* **5**, 774–777.

Cess, R. D. 1958 A survey of the literature on heat transfer in turbulent tube flow. Report 8-0529-R24. Westinghouse Research.

Chong, M. S., Soria, J., Perry, A. E., Chacin, J., Cantwell, B. J. & Na, Y. 1998 Turbulence structures of wall-bounded flows using DNS data. *J. Fluid Mech.* **357**, 225–247.

Christensen, K. T. & Adrian, R. J. 2001 Statistical evidence of hairpin vortex packets in wall turbulence. *J. Fluid Mech.* **431**, 433–443.

Coceal, O., Dobre, A., Thomas, T. G. & Belcher, S. E. 2007 Structure of turbulent flows over regular arrays of cubical roughness. *J. Fluid Mech.* **589**, 375–409.

Comte-Bellot, G. 1965 Écoulement turbulent entre deux parois parellèles. Publications Scientifiques et Techniques 419. Ministère de L'Air.

Darcy, H. 1857 *Recherches Expérimentales Relatives au Mouvement de l'Eau dans les Tuyaux*. Mallet-Bachelier, Paris.

Djenidi, L., Anselmet, F. & Antonia, R. A. 1994 Lda measurements in a turbulent boundary layer over a *d*-type rough wall. *Experiments in Fluids* **16**, 323–329.

Flack, K. A., Shultz, M. P., & Shapiro, T. A. 2005 Experimental support for townsend's Reynolds number similarity hypothesis on rough walls. *Phys. Fluids* **17**, 035102.

Frisch, U. 1995 *Turbulence*. Cambridge U. Press, 103.

Ganapathisubramani, B., Longmire, E. K. & Marusic, I. 2003 Characteristics of vortex packets in turbulent boundary layers. *J. Fluid Mech.* **478**, 35–46.

George, W. K. & Castillo, L. 1997 Zero-pressure-gradient turbulent boundary layer. *Appl. Mech. Rev.* **50**, 689–730.

de Graaff, D. B. & Eaton, J. K. 2000 Reynolds-number scaling of the flat-plate turbulent boundary layer. *J. Fluid Mech.* **422**, 319–346.

Grant, H. L. 1958 The large eddies of turbulent motion. *J. Fluid Mech.* **4**, 149.

Guala, M., Hommema, S. E. & Adrian, R. J. 2006 Large-scale and very-large-scale motions in turbulent pipe flow. *J. Fluid Mech.* **554**, 521–542.

Hägen, G. 1854 Über den Einfluss der Temperatur auf die Bewegung des Wassers in Röhren. *Math. Abh. Akad. Wis. Berlin* **17**, 17–98.

Haidari, A. H. & Smith, C. R. 1994 The generation and regeneration of single hairpin vortices. *J. Fluid Mech.* **277**, 135–162.

Hanjalić, H. & Launder, B. E. 1972 Fully developed asymmetric flow in a plane channel. *J. Fluid Mech.* **51**, 301–335.

Head, M. R. & Bandyopadhyay, P. 1981 New aspects of turbulent boundary-layer structure. *J. Fluid Mech.* **107**, 297–338.

Hinze, J. O. 1975 *Turbulence*, 2nd edn. Mac Graw-Hill New York.

Hites, M. 1997 Scaling of high-Reynolds number turbulent boundary layers in the national diagnostic facility. Ph. D. thesis, Illinois Inst. of Technology.

Hoyas, S. & Jiménez, J. 2006 Turbulent channel simulation at $Re_\tau = 2000$. *Phys. Fluids* **18**, 011702.

Hunt, J. C. R. & Morrison, J. F. 2000 Eddy structure in turbulent boundary layers. *Eur. J. Mech. B Fluids* **19**, 673–694.

Hunt, J. C. R., Wray, A. A. & Moin, P. 1988 Eddies, streams, and convergence zones in turbulent flows. In *Proc. Summer Program*, pp. 9–14. Center for Turbulence Research, Stanford University.

Hutchins, N., Ganapathisubramani, B. & Marusic, I. 2007 Large-scale influences in near-wall turbulence. *Phil. Trans. R. Soc. A* **365**, 647–664.

Jackson, P. S. 1981 On the displacement height in the logarithmic velocity profile. *J. Fluid Mech.* **111**, 15–25.

Jiménez, J. 1994 On the structure and control of near wall turbulence. *Phys. Fluids* **6**, 944–953.

Jiménez, J. 1998 The largest structures in turbulent wall flows. In *Ann. Res. Briefs*, pp. 943–945. Center for Turbulence Research, Stanford University.

Jiménez, J. 2000 Turbulence. In *Perspectives in Fluid Dynamics* (ed. G. K. Batchelor, H. K. Moffat & M. G. Worster), pp. 231 – 288. Cambridge U. Press.

Jiménez, J. 2004 Turbulent flows over rough walls. *Ann. Rev. Fluid Mech.* **36**, 173–196.

Jiménez, J., del Álamo, J. C. & Flores, O. 2004 The large-scale dynamics of near-wall turbulence. *J. Fluid Mech.* **505**, 179 – 199.

Jiménez, J., Flores, O. & García-Villalba, M. 2001*a* The large-scale organization of autonomous turbulent wall regions. In *Ann. Res. Briefs*, pp. 317–327. Center for Turbulence Research, Stanford University.

Jiménez, J., Kawahara, G., Simens, M. P., Nagata, M. & Shiba, M. 2005 Characterization of near-wall turbulence in terms of equilibrium and bursting solutions. *Phys. Fluids* **15** (015105).

Jiménez, J. & Moin, P. 1991 The minimal flow unit in near-wall turbulence. *J. Fluid Mech.* **225**, 221–240.

Jiménez, J. & Pinelli, A. 1999 The autonomous cycle of near-wall turbulence. *J. Fluid Mech.* **389**, 335–359.

Jiménez, J. & Simens, M. P. 2000 The largest scales in turbulent flow: the structure of the wall layer. In *Coherent Structures in Complex Systems* (ed. D. Reguera, L. L. Bonilla & J. M. Rubí), pp. 39–57. Springer.

Jiménez, J. & Simens, M. P. 2001 Low-dimensional dynamics in a turbulent wall flow. *J. Fluid Mech.* **435**, 81.

Jiménez, J., Uhlmann, M., Pinelli, A. & Kawahara, G. 2001*b* Turbulent shear flow over active and passive porous surfaces. *J. Fluid Mech.* **442**, 89 – 117.

Jiménez, J. & Wray, A. A. 1998 On the characteristics of vortex filaments in isotropic turbulence. *J. Fluid Mech.* **373**, 255–285.

Kaneda, Y. & Ishihara, T. 2006 High-resolution direct numerical simulation of turbulence. *Journal of Turbulence* **7**, 1–17.

von Kármán, T. 1930 Mechanische Ahnlichkeit und Turbulenz. In *Proceedings Third Int. Congr. Applied Mechanics, Stockholm*, pp. 85–105.

von Kármán, T. & Howarth, L. 1938 On the statistical theory of isotropic turbulence. *Proc. Royal Soc. London* **A 164**, 192–215.

Kawahara, G., Jiménez, J., Uhlmann, M. & Pinelli, A. 2003 Linear instability of a corrugated vortex sheet – a model for streak instability. *J. Fluid Mech.* **483**, 315 – 342.

Keirsbulck, L., Labraga, L., Mazouz, A. & Tournier, C. 2002 Surface roughness effects on turbulent boundary layer structures. *J. Fluid Eng - Trans ASME* **124**, 127–135.

Kim, H. T., Kline, S. J. & Reynolds, W. C. 1971 The production of turbulence near a smooth wall in a turbulent boundary layer. *J. Fluid Mech.* **50**, 133–166.

Kim, J., Moin, P. & Moser, R. D. 1987 Turbulence statistics in fully developed channel flow at low Reynolds number. *J. Fluid Mech.* **177**, 133–166.

Kim, K. 1999 On the structure of pressure fluctuations in simulated turbulent channel flow. *J. Fluid Mech.* **205**, 421–451.

Kim, K. & Adrian, R. J. 1999 Very large-scale motion in the outer layer. *Phys. Fluids* **11**, 417–422.

Kolmogorov, A. N. 1941 Dissipation of energy in isotropic turbulence. *Dokl. Akad. Nauk. SSSR* **32**, 19 – 21.

Kolmogorov, A. N. 1962 A refinement of previous hypothesis concerning the local structure of turbulence in viscous incompressible fluid at high Reynolds number. *J. Fluid Mech.* **13**, 82 – 85.

Kovasznay, L. S. G., Kibbens, V. & Blackwelder, R. F. 1970 Large-scale motion in the intermittent region of a turbulent boundary layer. *J. Fluid Mech.* **41**, 283.

Krogstad, P.-A. & Antonia, R. A. 1994 Structure of turbulent boundary layers on smooth and rough walls. *J. Fluid Mech.* **277**, 1–21.

Krogstad, P. A. & Antonia, R. A. 1999 Surface roughness effects in turbulent boundary layers. *Experiments in fluids* **27**, 450–460.

Krogstad, P. A., Antonia, R. A. & Browne, L. W. B. 1992 Comparison between rough- and smooth-wall turbulent boundary layers. *J. Fluid Mech.* **245**, 599–617.

Kwok, W. Y., Moser, R. D. & Jiménez, J. 2001 A critical evaluation of the resolution properties of b-splines and compact finite difference methods. *J. Comput. Phys.* **174**, 510–551.

Launder, B. E. & Spalding, D. B. 1992 *Mathematical Models of Turbulence*. Academic.

Lele, S. K. 1992 Compact finite difference schemes with spectral-like resolution. *J. Comput. Phys.* **103**, 16–42.

Leonardi, S., Orlandi, P., Smalley, R. J., Djenidi, L. & Antonia, R. A. 2003 Direct numerical simulation of turbulent channel flow with transverse square bars on one wall. *J. Fluid Mech.* **491**, 229–238.

Lesieur, M. 1997 *Turbulence in fluids*, 3rd edn. Kluwer.

Ligrani, P. M. & Moffat, R. J. 1986 Structure of transitionally rough and fully rough turbulent boundary layers. *J. Fluid Mech.* **162**, 69–98.

Marusic, I. 2001 On the role of large-scale structures in wall turbulence. *Phys. Fluids* **13**, 735–743.

Meinhart, C. D. & Adrian, R. J. 1995 On the existence of uniform momentum zones in a turbulent boundary layer. *Phys. Fluids* **7**, 694–696.

Millikan, C. B. 1939 A critical discussion of turbulent flows in channels and circular tubes. In *Proceedings 5th Int. Cong. Appl. Math.* (ed. J. P. D. Hartog & H. Peters). Wiley.

Moin, P., Adrian, R. J. & Kim, J. 1987 Stochastic estimation of organized structures in turbulent channel flow. In *Proc. 6th Turbulent Shear Flows Symp*, pp. 16.9.1–16.9.8. Toulouse, France.

Moin, P. & Mahesh, K. 1998 Direct Numerical Simulation: A tool in turbulence research. *Annu. Rev. Fluid Mech.* **30**, 539–578.

Moin, P. & Moser, R. D. 1989 Characteristic-eddy decomposition of turbulence in a channel. *J. Fluid Mech.* **200**, 471–509.

Monty, J. P., Stewart, J. A., Williams, R. C. & Chong, M. S. 2007 Large-scale features in turbulent pipe and channel flows. *J. Fluid Mech.* **589**, 147–156.

Morrison, J. F., McKeon, B. J., Jiang, W. & Smits, A. J. 2004 Scaling of the streamwise velocity component in turbulent pipe flow. *J. Fluid Mech.* **508**, 99–131.

Nagata, M. 1990 Three-dimensional finite-amplitude solutions in plane Couette flow: Bifurcation from infinity. *J. Fluid Mech.* **217**, 519.

Niederschulte, M. A., Adrian, R. J. & Hanratty, T. J. 1990 Measurements of turbulent flow in a channel at low reynolds numbers. *Exps. Fluids* **9**, 222–230.

Nikuradse, J. 1932 Turbulente strömung in Nichtkreisförmigen Rohren. *Forshg. Arb. Ing.-Wes.* **356**.

Nikuradse, J. 1933 Strömungsgesetze in Rauhen Rohren. *VDI-Forsch* **361**, engl. transl. 1950. Laws of flow in rough pipes. *NACA TM* 1292.

Oberlack, M. 1997 Similarity in rotating and non-rotating turbulent pipe flows. *J. Fluid Mech.* **379**, 1–22.

Oboukhov, A. M. 1962 Some specific features of atmospheric turbulence. *J. Fluid Mech.* **13**, 77–81.

Onsager, L. 1945 The distribution of energy in turbulence. *Phys. Rev.* **68**, 286.

Orlandi, P., Leonardi, S., Tuzi, R. & Antonia, R. A. 2003 Direct numerical simulations of turbulent channel flow with wall velocity disturbances. *Phys. Fluids.* **15**, 3587–3601.

Perry, A. E. & Abell, C. J. 1975 Scaling laws for pipe-flow turbulence. *J. Fluid Mech.* **67**, 257.

Perry, A. E. & Abell, C. J. 1977 Asymptotic similarity of turbulence structures in smooth- and rough-walled pipes. *J. Fluid Mech.* **79**, 785 – 799.

Perry, A. E. & Chong, M. S. 1982 On the mechanism of wall turbulence. *J. Fluid Mech.* **119**, 173–217.

Perry, A. E., Henbest, S. & Chong, M. S. 1986 A theoretical and experimental study of wall turbulence. *J. Fluid Mech.* **119**, 163–199.

Perry, A. E., Lim, K. L. & Henbest, S. 1987 An experimental study of turbulence structure in smooth- and rough-wall turbulent boundary layer. *J. Fluid Mech.* **177**, 437–466.

Perry, A. E. & Marusic, I. 1995 A wall-wake model for the turbulence structure of boundary layers. 1. Extension of the attached eddy hypothesis. *J. Fluid Mech.* **298**, 361–388.

Perry, A. E., Schofield, W. H. & Joubert, P. N. 1969 Rough-wall turbulent boundary layers. *J. Fluid Mech.* **37**, 383–413.

Poggi, D., Porporato, A. & Ridolfi, L. 2003 Analysis of the small-scale structure of turbulence on smooth and rough walls. *Phys. Fluids* **15**, 35–46.

Pope, S. B. 2000 *Turbulent flows*. Cambridge U. Press.

Prandtl, L. 1904 Über Flüssigkeitsbewegung bei sehr kleiner Reibung. In *Verhandlungen IIIrd Intern. Math. Kongress Heidelberg*, pp. 484–491. English translation: NACA Memo No. 453 (1928).

Prandtl, L. 1914 Der Luftwiderstand von Kugeln. *Math. Phys. Klasse* pp. 177–190.

Prandtl, L. 1925 Beritch über die Entstenhung der Turbulenz. *Z. Angew. Math. Mech.* **5**, 136–139.

Prandtl, L. 1935 The mechanics of viscous fluids. In *Aerodynamics Theory, Vol III* (ed. W. F. Durand), pp. 34–208. Springer Verlag.

Raupach, M. R., Antonia, R. A. & Rajagopalan, S. 1991 Rough-wall turbulent boundary layers. *Appl. Mech. Rev.* **44**, 1–25.

Reddy, S. C. & Henningson, D. S. 1993 Energy growth in viscous channel flows. *J. Fluid Mech.* **525**, 209 – 238.

Reichardt, H. 1951 Vollständige Darstellung der Turbulenten Geschwindigkeitsverteilung in glatten Leitungen. *ZAMM* **31**, 208–219.

Reynolds, O. 1883 An experimental investigation of the circumstances which determine whether the motion of water shall be direct or sinuose, and of the law of resistance in parallel channels. *Phil. Trans. R. Soc. London* **174**, 935–982.

Reynolds, O. 1894 On the dynamical theory of incompressible viscous fluids and the determination of the criterion. *Phil. Trans. R. Soc. London* **186**, 123–164.

Reynolds, W. C. & Hussain, A. K. M. F. 1972 The mechanics of an organized wave in turbulent shear flow. part 3. theoretical models and comparisons with experiments. *J. Fluid Mech.* **54**, 263–288.

Richardson, L. F. 1920 The supply of energy from and to atmospheric eddies. *Proc. R. Soc. A* **97**, 354–373.

Robinson, S. K. 1991*a* Coherent motions in the turbulent boundary layer. *Ann. Rev. Fluid Mech.* **23**, 601–639.

Robinson, S. K. 1991*b* The kinematics of turbulent boundary layer structure. Ph.D. thesis, NASA Ames Research Center.

Sabot, J., Saleh, I. & Comte-Bellot, G. 1977 Effects of roughness on the intermittent maintenance of reynolds shear stress in pipe flow. *Phys. Fluids* **20**, 150–155.

Sagaut, P. 2005 *Large Eddy Simulation for incompressible flows: an introduction*, 3rd edn. Springer.

Schlichting, H. 1979 *Boundary-Layer Theory*. Mc Graw-Hill.

Schoppa, W. & Hussain, F. 2002 Coherent structure generation in near-wall turbulence. *J. Fluid Mech.* **453**, 57–108.

Singer, B. A. & Joslin, R. D. 1994 Metamorphosis of a hairpin vortex into a young turbulent spot. *Phys. Fluids* **6**, 3724–3736.

Sirovich, L. & Karlsson, S. 1997 Trubulent drag reduction by passive mechanisms. *Nature* **388**, 753–55.

Skote, M., Haritonidis, J. H. & Henningson, D. S. 2002 Varicose instabilities in turbulent boundary layers. *Phys. Fluids* **14** (7), 2309–2323.

Smagorinski, J. 1963 General circulation experiments with the primitive equations. *Mon. Weather Rev.* **91**, 99–164.

Spalart, P. R. 1988 Direct simulation of a turbulent boundary layer up to $Re_\theta = 1410$. *J. Fluid Mech.* **187**, 61–98.

Spalart, P. R., Moser, R. D. & Rogers, M. M. 1991 Spectral methods for the navier-stokes equations with one infinite and two periodic directions. *J. Comp. Phys.* **96**, 297 – 324.

Stretch, D. D. 1990 Automated pattern eduction from turbulent flow diagnostics. In *CTR Ann. Res. Briefs*, pp. 145–157. Stanford Univ.

Suponitsky, V., Cohen, J. & Bar-Yoseph, P. Z. 2005 The generation of streaks and hairpin vortices from a localized vortex disturbance embedded in a unbounded uniform shear flow. *J. Fluid Mech.* **553**, 65–100.

Tanahashi, M., Kang, S.-J., Miyamoto, T., Shiokawa, S. & Miyauchi, T. 2004 Scaling of fine scale eddies in turbulent channel flows up to $Re_\tau = 800$. *Int. Journal of Heat and Fluid Flow* **25**, 331 – 340.

Tani, I. 1988 Drag reduction by riblet viewed as a roughness problem. *Proc. Jpn. Acad. B* **64**, 21–24.

Taylor, G. I. 1921 Difussion by continuous movements. *Proc. London Math. Soc.* **20**, 196–212.

Taylor, G. I. 1935 Statistical theory of turbulence. Parts I to IV. *Proc. Royal Soc. London* **A 151**, 421–478.

Tennekes, H. & Lumley, J. L. 1972 *First course in turbulence*. MIT. Press.

Theodorsen, T. 1952 Mechanism of turbulence. In *Proc. Second Midwestern Conf. on Fluid Mechanics, Ohio, Ohio State University*, pp. 1 – 18.

Thom, A. S. 1971 Momentum absorption by vegetation. *Quart. J. Royal Meteorol. Soc.* **97**, 414–428.

Toh, S. & Itano, T. 2001 On the regeneration mechanism of turbulence in the channel flow. In *Proceedings of IUTAM Symposium on Geometry and Statistics of Turbulence* (ed. T. Kambe, T. Nakano & T. Miyauchi), p. 305. Kluwer, Dordrecht.

Toh, S. & Itano, T. 2005 Interaction between a large-scale structure and near-wall strcutures in channel flow. *J. Fluid Mech.* **524**, 249–262.

Tomkins, C. D. & Adrian, R. J. 2003 Spanwise structure and scale growth in turbulent boundary layers. *J. Fluid Mech.* **490**, 37–74.

Townsend, A. A. 1958 The turbulent boundary layer. In *Boundary Layer Research* (ed. H. Gortler), , vol. 1. Springer-Verlag Berlin.

Townsend, A. A. 1961 Equilibrium layers and wall-turbulence. *J. Fluid Mech.* **11**, 97–120.

Townsend, A. A. 1976 *The structure of turbulent shear flows*, 2nd edn. Cambridge U. Press.

Waleffe, F. 2001 Exact coherent structures in channel flows. *J. Fluid Mech.* **435**, 81.

Waleffe, F. 2003 Homotopy of exact coherent structures in plane shear flows. *Phys. Fluids* **15**, 1517.

Wallace, J. M., Eckelmann, H. & Brodkey, R. S. 1972 The wall region in turbulent shear flow. *J. Fluid Mech.* **54**, 39–48.

Wei, T. & Willmarth, W. W. 1989 Reynolds-number effects on the structure of a turbulent channel flow. *J. Fluid Mech.* **204**, 57–95.

Wilcox, C. D. 1993 *Turbulence modelling for CFD*. DCW Industries.

Willmarth, W. W. & Lu, S. S. 1972 Structure of the Reynolds near the wall. *J. Fluid Mech.* **55**, 65–92.

Willmarth, W. W. & Woolridge, C. E. 1962 Measurements of the fluctuating pressure at the wall beneath a thick turbulent boundary layer. *J. Fluid Mech.* **14**, 187–210.

Wills, J. A. B. 1964 On convection velocities in turbulent shear flows. *J. Fluid Mech.* **20**, 417–432.

Zhou, J. & Adrian, R. J. 1995 Autogeneration of near-wall vortical structures in channel flow. *Phys. Fluids* **8**, 288–290.

Zhou, J., Adrian, R. J., S., B. & Kendall, T. M. 1999 Mechanisms for generating coherent packets of hairpin vortices in channel flow. *J. Fluid Mech.* **387**, 353–396.